

# UC San Diego

## UC San Diego Electronic Theses and Dissertations

### Title

Photoluminescence spectral study of single CdSe/ZnS Colloidal Nanocrystals in Poly(methyl methacrylate) and Quantum Dots molecules

### Permalink

<https://escholarship.org/uc/item/8w79q35z>

### Author

Shen, Yaoming

### Publication Date

2008

Peer reviewed|Thesis/dissertation

UNIVERSITY OF CALIFORNIA, SAN DIEGO

Photoluminescence Spectral Study of Single CdSe/ZnS Colloidal Nanocrystals in  
Poly(methyl methacrylate) and  
Quantum Dots Molecules

A dissertation submitted in partial satisfaction of the  
requirements for the degree Doctor of Philosophy  
in  
Electrical Engineering(Applied physics)

by

Yaoming Shen

Committee in charge:

Professor Yeshaiahu Fainman, Chair  
Professor Lu J. Sham, Co-Chair  
Professor Leonid Butov  
Professor Charles Tu  
Professor Deli Wang

2008

Copyright  
Yaoming Shen, 2008  
All rights reserved.

The dissertation of Yaoming Shen is approved, and it is acceptable in quality and form for publication on micro-film:

---

---

---

---

Co-Chair

---

Chair

University of California, San Diego

2008

# TABLE OF CONTENTS

Signature Page . . . . .	iii
Table of Contents . . . . .	iv
List of Figures . . . . .	vi
Acknowledgements . . . . .	ix
Vita and Publications . . . . .	xi
Abstract . . . . .	xii
I Introduction . . . . .	1
A. Brief history of semiconductor nanocrystals and quantum dots study . . . . .	1
B. Motivations . . . . .	2
C. Thesis outline . . . . .	6
II Quantum dot energy levels calculation . . . . .	8
A. Density of states in quantum semiconductor structures . . . . .	9
B. Particle-in-a-spherical potential model . . . . .	11
C. Optical transition probabilities and dipole moment . . . . .	18
D. Tunneling transport and diffusion in weakly coupled quantum dot ensembles . . . . .	19
III Characterization of the CdSe/ZnS nanocrystals . . . . .	23
A. Photoluminescence measurement . . . . .	23
B. Single nano-object spectroscopy . . . . .	28
IV PMMA nanocrystals composites fabricated via use of pre-polymerization . . . . .	31
A. Introduction . . . . .	31
B. Incorporation of NCs into thick bulk polymer matrix using pre-polymerization . . . . .	33
C. Low temperature measurement . . . . .	40
D. CdSe/ZnS NCs in negative photon resist SU-8 . . . . .	41
1. Introduction . . . . .	41
2. SU-8-NC composite waveguides . . . . .	43
E. Infrared NCs in PMMA . . . . .	45
F. Discussions and conclusions . . . . .	48
V Photoluminescence spectral study of single CdSe nanocrystals in PMMA . . . . .	50
A. Introduction to the history of single NC study . . . . .	50
1. Definition of blinking (fluorescence intermittency) of NCs . . . . .	50
2. Telegraph noise . . . . .	52

3. Auger process . . . . .	52
4. Power law . . . . .	52
B. Experiment purpose and set up . . . . .	53
C. Experiment results . . . . .	55
1. Spectral diffusion . . . . .	55
2. Influence of spectral diffusion on the line shapes of single CdSe NCs . . . . .	57
3. Spectral jumps between two states . . . . .	57
4. Tunneling Model . . . . .	60
5. Fluorescence quenching . . . . .	61
6. Photo-enhanced luminescence . . . . .	66
7. Blinking . . . . .	68
8. Phonon replicas . . . . .	69
9. Other types . . . . .	71
D. Conclusions . . . . .	71
VI Optical characterization of InAs/GaAs Quantum Dots Molecules (Double Quantum Dots) . . . . .	73
A. Compare between as-grown quantum dots and self-assembled InAs/GaAs lateral double quantum dots . . . . .	73
1. Experimental procedure . . . . .	74
2. Results and discussion . . . . .	75
B. The Effects of Rapid Thermal Annealing on Doubled Quantum Dots Grown by Molecular Beam Epitaxy . . . . .	82
1. Introduction . . . . .	82
2. Experimental Procedure . . . . .	82
3. Results and Discussions . . . . .	83
C. Summary . . . . .	90
Bibliography . . . . .	91

## LIST OF FIGURES

Figure II.1: Schematic representation of density of states $N(E)$ for an ideal a) Bulk-semiconductor B)Thin film c) Quantum wire d) Quantum dot [1] . . . . .	11
Figure IV.1: Originally NCs were suspended in liquid. After processing, they were incorporated in PMMA solid matrix. The pre-polymerized polymer could be cast into various molds to form solid-state polymer with various shape. . . . .	34
Figure IV.2: a) For the prepolymerization, the color is uniform, as shown in the right figure. The directly polymerized counterpart, however, exhibits severe non-uniformity, as shown in the left figure. From the close-up , large bunches of clusters can be observed. . . . .	35
Figure IV.3: Absorption and PL spectra of NCs in (a) toluene solution and (b) PMMA-NC composite, where the dash line shows the absorption spectrum of a 1 mm thick pure PMMA slide. . . . .	37
Figure IV.4: NCs in PMMA gratings . . . . .	38
Figure IV.5: (a)SEM photograph of a PMMA-NC composite waveguide array on a $SiO_2$ /Si substrate. (b) Closeup of PMMA-NC composite waveguide (c) Image of optical beam trace traveling along the waveguide. (d) Mode profile from the waveguide output. . . . .	39
Figure IV.6: Integrated PL spectra for NCs in PMMA-NC composite vs temperature. . . . .	40
Figure IV.7: Full width half maximum of PL spectra for NCs in PMMA-NC composite vs temperature. . . . .	41
Figure IV.8: The PL for SU-8-NCs compared with the PL for NCs in liquid	42
Figure IV.9: SU-8 composite structures by using e-beam lithography. . . .	44
Figure IV.10: SU-8 composite structures by using KalSUSS mask aligner: (a) SEM photographs of a straight waveguide and (b) microscopic images of a spiral waveguide excited with a UV laser (364 nm). . . .	46
Figure IV.11: The PL of Infrared PbSe NCs in PMMA. The peak wavelength shifts 134 nm from 1200 nm in liquid to 1334 nm in PMMA. The FWHM wavelength in both cases are about the same. . . . .	47
Figure IV.12: Infrared NCs PbSe in PMMA absorption . . . . .	47
Figure V.1: The micro PL experiment setup for single CdSe nanocrystals in PMMA measurement. . . . .	53
Figure V.2: This is a typical image detected by the liquid Nitrogen cooled CCD camera. Horizontal and vertical axes are the horizontal and the vertical pixels of the CCD correspondingly. Z axis is the intensity value read by the CCD, which is shown in color as well. . . . .	54

Figure V.3: Spectra from another NC were recorded continuously with an integration time of 0.5 s. The emission peak randomly shifts with small energy changes between 2.099 eV and 2.108 eV. . . . .	58
Figure V.4: Spectra from a typical switching NC, recorded at six different excitation powers (2.0, 3.2, 5.0, 7.2, 11, $20 \times 10^3 \text{W/cm}^2$ ) are shown in order in (a)-(f). The integration time 2 s is used for this measurement. . . . .	59
Figure V.5: NC has been quenched after a few minutes. But there is almost no sign before quenching happens except the PL peak jumps between two states. The right figure is a magnified part of the left figure. . . . .	62
Figure V.6: Before quenching happens, the PL peak jumps to a lower energy state. . . . .	63
Figure V.7: Before quenching happens, the PL peak jumps to a higher energy state . . . . .	64
Figure V.8: The NC is pumped continuously by the CW laser. PL is observed increasing with time. The sharp peak close to 603 nm is noise. . . . .	66
Figure V.9: Although in our measurement blinking phenomenon is not dominant, we do see some of the dots will recover after stayed dark for a few minutes. It is different with quenching since quenching bleached the NCs and they won't emit light any more. . . . .	68
Figure V.10: Spectra from a NC were recorded continuously with an integration time of 2 s each. (a-c) shows in some NCs, higher laser intensity not only increases the switching frequency, but also makes the states moving randomly. . . . .	69
Figure V.11: Spectra from a NC were recorded continuously with an integration time of 30 s each and constant temperature and excitation power. We used a 30 s integration time for each frame to see the lower energy peaks which are weaker than the exciton peak. . . . .	70
Figure VI.1: (a) shows a $2 \times 2 \mu\text{m}^2$ AFM image of the as grown QDs sample surface. The distribution of the QDs' heights are shown on (b). We estimate their height to be $h_1 = 11 \pm 1 \text{nm}$ . . . . .	75
Figure VI.2: (a) shows a $2 \times 2 \mu\text{m}^2$ AFM image of the Bi-QDs sample surface. The distribution of the Bi-QDs' heights are shown on (b). We estimate their height to be $3.8 \pm 1 \text{nm}$ . A Gaussian fit has been included. It indicates that there are two Gaussian distributions. . . . .	76
Figure VI.3: Center-to-center width histogram of DQDs with Gaussian fit. . . . .	78
Figure VI.4: PL spectra of as-grown QDs and DQDs at 9 K. The dotted curves for DQDS are the Gaussian components. . . . .	79
Figure VI.5: The temperature-dependent peak emission energy of as-grown QDs and DQDs. The solid lines are calculations from the Varshni equation. . . . .	80



Figure VI.6: The temperature dependence of PL intensity of as-grown QDs and DQDs. . . . .	81
Figure VI.7: AFM image of as-grown DQDs fabricated by MBE under $As_2$ overpressure. . . . .	84
Figure VI.8: Cross-sectional TEM. The lower wetting layer is formed when the first as-grown QDs are made. The 1.7 nm thickness of thin GaAs layer is fabricated during partial-capping process. . . . .	85
Figure VI.9: Shows the low temperature PL spectra of as-grown DQDs which were annealed at $650^\circ C$ , $750^\circ C$ and $850^\circ C$ . . . . .	86
Figure VI.10: Temperature-dependent PL data are measured from 9 K to 290 K with 50 mW incident excitation intensity from a diode-pumped solid-state laser at 532 nm. The PL peak energy as a function of sample temperature is shown in the inset. . . . .	87
Figure VI.11: Shows the PL intensity of as-grown DQDs and their annealed DQDs as a function of inverse temperature. . . . .	88

## ACKNOWLEDGEMENTS

First and foremost I offer my sincerest gratitude to both of my supervisors, Professor Lu J. Sham and Professor Yeshaiahu Fainman, who have supported me throughout my thesis with their patience and knowledge while allowing me the room to work in my own way. I attribute the level of my doctor degree to their encouragement and effort. Without them this thesis, too, would not have been completed or written. One simply could not wish for two better or nicer supervisors.

I appreciate the help from Drs. Dmitriy Panasenko, Kevin Tetz and Lin Pang when I first joined the group. I also want to thank all my colleagues in Prof. Sham's and Prof. Fainman's groups: Chia-Ho, Sandra, Slava, Nikola, Robbie, Maziar, Maxim, Liang, Kazu, Alex, Wang and Renbao. You guys are great. Thanks for the good opinions and discussions.

I must pay my respect and thankfulness to Professor Leonid Butov, who, back in 2005, gave me a chance to use his lab and offered me all the valuable advices in the micro-PL measurement. I'm also grateful to his students: Sen and Aaron. The discussion with them is really helpful.

Dr. Suwaree Suraprapapich have provided me with all of QD molecules samples covered in this thesis as well as many others, with consistent quality. Professor Charles Tu has offered much advice and insight throughout my work on QD molecules study.

I am most grateful to my family, who were always there to encourage me whenever I felt depressed.

The text of chapter IV, in part, is a reprint of the material as it appears in Yaoming Shen, Lin Pang, Kevin Tetz, Yeshaiahu Fainman "Characterization

of PMMA quantum dot composite fabricated by pre-polymerizing method” SPIE (2004), where the dissertation author was the first author. Also in part, is a reprint of the material as it appears in L. Pang, Y. Shen, K. Tetz, and Y. Fainman, “PMMA quantum dots composites fabricated via use of pre-polymerization,” Opt. Expr., 13, 44-49 (2005), where the dissertation author was the second author. The co-authors in this publication directed, supervised, and co-worked on the research which forms the basis of this chapter.

The text of chapter V, in part, is a reprint of the material as it appears in Yaoming Shen, Lin Pang, Y. Fainman, Martin Griswold, Sen Yang, L. V. Butov, and L. J. Sham “Photoluminescence spectral switching of single CdSe/ZnS colloidal nanocrystals in poly(methyl methacrylate)” Phys. Rev. B 76, 085312 (2007), where the dissertation author was the first author. The co-authors in this publication directed, supervised, and co-worked on the research which forms the basis of this chapter.

The text of chapter VI, in part, is a reprint of the material as it appears in S. Suraprapapich, Y. Shen, V. A. Odnoblyudov, S. Panyakeow, C. W. Tu, “Self-Assembled Lateral Bi-Quantum Dot Molecule Formation by Gas Source Molecular Beam Epitaxy”, 9 January 2007, Journal of Crystal Growth, where the dissertation author was the second author. The co-authors in this publication directed, supervised, and co-worked on the research which forms the basis of this chapter.

## VITA

2001	B.S. Department of Physics, Peking University, Beijing, China
2001–2004	Research Assistant, Department of Electrical and Computer Engineering, University of California, San Diego
2004	M.S., University of California, San Diego
2004–2007	Research Assistant, Department of Electrical and Computer Engineering, University of California, San Diego
2008	Doctor of Philosophy, University of California, San Diego

## PUBLICATIONS

Yaoming Shen, Lin Pang, Y. Fainman, Martin Griswold, Sen Yang, L. V. Butov, and L. J. Sham “Photoluminescence spectral switching of single CdSe/ZnS colloidal nanocrystals in poly(methyl methacrylate)” Phys. Rev. B 76, 085312 (2007)

Yaoming Shen, Lin Pang, Kevin Tetz, Yeshaiah Fainman “Characterization of PMMA quantum dot composite fabricated by pre-polymerizing method” SPIE (2004)

L. Pang, Y. Shen, K. Tetz, and Y. Fainman, “PMMA quantum dots composites fabricated via use of pre-polymerization,” Opt. Expr., 13, 44-49 (2005).

L. Pang, K. Tetz, Y. Shen, C. Chen and Y. Fainman, “Photosensitive quantum dot composites and their applications in optical structures”, J. Vac. Sci. Technol. B 23, 2413-2418 (2005)

Lin Pang, Yaoming Shen, Kevin Tetz, Chyong Hua Chen, Yeshaiah Fainman, “PMMA quantum dots composites and their applications” SPIE (2005)

S. Suraprapich, Y. Shen, V. A. Odnoblyudov, S. Panyakeow, C. W. Tu, “Self-Assembled Lateral Bi-Quantum Dot Molecule Formation by Gas Source Molecular Beam Epitaxy”, 9 January 2007, Journal of Crystal Growth.

K. Ikeda, Y. Shen and Y. Fainman “Study on Nonlinear Optical Property of Amorphous Silicon with Z-scan Technique” submitted to CLEO

## ABSTRACT OF THE DISSERTATION

Photoluminescence Spectral Study of Single CdSe/ZnS Colloidal Nanocrystals in  
Poly(methyl methacrylate) and Quantum Dot Molecules

by

Yaoming Shen

Doctor of Philosophy in Electrical and Computer Engineering (Applied Physics)

University of California, San Diego, 2008

Professor Yeshaiah Fainman, Chair

Professor Lu J. Sham, Co-chair

Quantum dots (QDs) and Nano-crystals (NCs) have been studied for decades. Because of the nanoscale quantum confinement, discrete energy density states and narrowband emitters properties, they hold great promise for numerous optoelectronics and photonics applications. They could be used for tunable lasers, white LED, Nano-OLED, non-volatile memory and solar cells. They are also the most promising candidates for the quantum computing.

The benefits for NCs over QDs is that NCs can be incorporated into a variety of polymers as well as thin films of bulk semiconductors. These exceptional flexibility and structural control distinguish NCs from the more traditional QD structures fabricated using epitaxial growth techniques.

In my research of work, I studied the photoluminescence (PL) and absorption character of ensemble NCs incorporated in Polymethyl methacrylate (PMMA). To understand the behavior of the NCs in PMMA, it is important to measure a single NC to avoid the inhomogeneous broadening of many NCs.

So I particularly studied the behavior of a single NC in PMMA matrix. A microphotoluminescence setup to optically isolate a single nanocrystal is used. Random spectral shift and blinking behavior (on and off) are found. Addition

to that, two color spectral shifting, is a major phenomena found in the system. Other interesting results such as PL intensity changes (decreasing or increasing with time) and quenching effect are observed and explained too.

From the correlation function, we can distinguish the phonon replicas. The energy of these phonons can be calculated very accurately from the experiment result. The Huang-Rhys factors can be estimated too.

Self-assembled semiconductor quantum dots (QDs), from highly strained-layer heteroepitaxy in the Stranski–Krastanow (S–K) growth mode, have been intensively studied because of the  $\delta$ -function-like density of states, which is significant for optoelectronic applications. Spontaneous formation of semiconductor quantum-dot molecules (QDMs), which are clusters of a few QDs, has attracted attention as a possible implementation of future quantum devices such as quantum cellular automata. With the advances in crystal growth techniques, the fabrication methods for nanostructures have been improved continuously. Lateral QDMs have been achieved. As a side topic, lateral QDMs have been studied and the result is presented in the last chapter.

# I

## Introduction

### I.A Brief history of semiconductor nanocrystals and quantum dots study

Semiconductor nanocrystals (NCs) are very small crystalline material which contain tens or a few hundred atoms with sizes of a few nanometers. Quantum dots (QDs) are semiconductor nanostructure that confine the motion of conduction band electrons, valence band holes, or excitons (bound pairs of conduction band electrons and valence band holes) in all three spatial directions. It is well known that below a certain size, the properties of the crystalline material start to deviate significantly from bulk properties and strongly dependent on size. These properties, so called nanoscale quantum confinement properties, make NCs and QDs attract much interest in the last few decades. They hold great promise for numerous optoelectronics and photonics applications such as in lasers, transistors, sensors, photodetectors and as biological labels [2]. Also quantum dot technology is one of the most promising candidates for use in solid-state quantum computation.

An important parameter of a semiconductor material is the width of the energy gap that separates the conduction from the valence energy bands. In bulk semiconductors, the width of this gap is a fixed parameter, which is determined

by the material’s identity. However, the situation changes in the case of nanoscale semiconductor particles with sizes smaller than 10 nm. This size range corresponds to the regime of quantum confinement for which electronic excitations “feel” the presence of the particle boundaries and respond to changes in the particle size by adjusting their energy spectra. The phenomenon is known as the quantum size effect.

Optical and electronic properties are dominated by the structure of valence and conduction bandedges. As the QD size decreases, the energy gap increases, leading, in particular, to a blue shift of the emission wavelength. In the first approximation, this effect can be described using a simple “quantum box” model. For a spherical QD with radius  $R$ , this model predicts that the size-dependent contribution to the energy gap is simply proportional to  $1/R^2$ . For QDs, discretization of energy levels at the conduction and valence bandedges (even though the allowed energy levels broaden to bands at the center), modifies the absorption spectrum into different peaks. Moreover, due to the relatively small number of electrons in a QD and dramatic changes in its properties by adding just one electron, QDs are sometimes considered as ‘artificial atoms’. The highest occupied molecular orbital (HOMO), as shown in the case of cluster, becomes the top of the valence band and the lowest unoccupied molecular orbital (LUMO) as bottom of the conduction band [3].

## I.B Motivations

Semiconductor QDs and NCs have wide applications due to their properties of narrowband emitters, tunable throughout the visible portion of the spectrum and broadband absorbers that can be used with multiple types of underlying short wavelength (UV, violet, blue) light sources.

**Tunable lasers** Quantum dot materials can provide superior performance in lasing applications compared to bulk semiconductors. In the zero dimen-



sional (0 D) quantum dots the separation between energy states is greater than the thermal energy of the charge carriers; this inhibits the thermal depopulation of the lowest, “emitting” transition, phenomenon that confers high-temperature stability and a narrow spectral emission width. Lasing was initially observed for CdSe quantum dots, imbedded in a glass matrix, in an optically pumped device. Lasing effect by electrical pumping (carrier injection) can also be achieved. In quantum dots more than one electron can be excited; every discrete electron and hole energy state can be populated either by one or by two particles with different spin orientations. The creation of the first electron-hole pair results in absorption saturation; the creation of two pairs with respectively oriented spin is called population inversion or optical gain. The two electron-hole pair states are classified as biexciton. Lasing effect results from the stimulated decay of a biexciton into a photon and exciton.

**White LED using quantum dots** Researchers at the Department of Energy’s (DOE) Sandia National Laboratories have developed the first solid-state white light-emitting device using quantum dots. They took an LED that produces intense, blue light. Coat it with a thin layer of NCs and produce white light in this way. In the future, the use of quantum dots as light-emitting phosphors may represent a major application of nanotechnology.

**Nano-OLED** In 2002, researchers in MIT have succeeded in combining plastic electronics with high-performance inorganic semiconductor nanocrystals to create a high-efficiency hybrid light-emitting structure; They claims that nanocrystal-organic light emitting diode that will one day replace liquid crystal displays (LCDs) as the flat-panel display of choice for consumer electronics. This is called Nano-OLED-nanocrystal-organic light emitting diode.

**Bioimaging** By far the most important application today is in biological imaging. Fluorescence labeling of specific compartments in cells is a widely used method in biology to visualize structural units that, due to lack of contrast or resolution, cannot be distinguished by just recording an image. The idea is to chemi-

cally link a fluorescent dye to a biomolecule that binds specifically and selectively to a certain compartment in the bio specimen. Current biosensors use fluorescent-based dyes; these dyes emit light over a broad spectral width - which limit their effectiveness to a small number of colors - and they also degrade over time under the microscope (phenomenon called “bleaching”). Core/shell CdSe/ZnS semiconductor nanocrystals are more robust fluorescent probes with size tunable emission properties. A shell of higher band gap semiconductor material can increase dramatically the brightness of quantum dots and protect them from photo bleaching. The surface of the quantum dots can also be chemically modified in such a way that the quantum dot can be chemically linked with a biomolecule that binds specifically to the target.

**Non-volatile memory** Future miniaturized devices, beyond the Moore’s law era of silicon, are expected to rely on new, ingenious methods to implement spatially controlled and highly functional nanoscale components synthesized by inexpensive chemistry. Chip technology based on self-assembly would enhance performance and packing density by orders of magnitude, deliver rich on-chip functionality, and operate at molecular level. Low-dimensional semiconductor nanostructures and organic molecules, which offer unique possibilities such as extremely low power dissipation, quantum effects, surface sensitivity and low synthesis cost, could be the building blocks for next-generation electronics. Optical memory is a technology that could potentially replace electrical data buffers in optical communication systems and allow for the elimination of the accompanying optical-to-electrical conversion hardware. Previously, optical memory devices have been implemented in III-V quantum dot systems, albeit at cryogenic temperatures. Room temperature operation is not possible in these devices because carriers are confined in relatively shallow potential wells. While similar devices have been fabricated in II-VI materials that can operate at room temperature, silicon based optical nanocrystal memory offers the possibility for implementation in industry compatible fabrication processes. Dielectric layers with embedded semiconductor nanocrystals are

widely studied recently, in order to overcome difficulties of non-volatile memory devices connected with technology scale-down, and to develop Si-based light emitting diodes (LEDs). So, although realtered metal-insulator-semiconductor (MIS) structures can be prepared on any semiconductor substrate, silicon-based structures are the most important ones for the technological development.

**Fuel cells** Potentially for developing high performance fuel cells for use in portable consumer electronics such as laptop computers, cell phones and digital cameras. A fuel cell is an energy conversion device and alternative to batteries that converts energy from chemical reaction into electricity and heat. Fuel cells combine fuels such as hydrogen or methanol along with air and water to produce electrical power. Fuel cells are environmentally friendly because their by-products are heat and water, and are viewed by many as a potential successor to less efficient and less environment all friendly portable power such as lithium-ion and other batteries used in portable electronics devices. The tremendous growth in unit sales of portable electronic devices, coupled with an increasing burden on battery life as applications become ever more complex, has created a serious concern amongst device manufactures about power requirements. The inherent higher energy density of small fuel cells in comparison to batteries has the potential to lead to both longer operational time and serve the power demands of next generation portable electronics.

**Nanocrystal solar cells** The other potential product is a new type of solar cell that performs like a traditional solar cell, but can be configured like a light weight, flexible plastic. In particular, this technology has the potential to provide low cost solar power through currently available, high volume and inexpensive manufacturing techniques based on conventional film based processes such as roll to roll manufacturing. Imagine a future in which the rooftops of residential homes and commercial buildings can be laminated with inexpensive, ultra-thin films of nano-sized semiconductors that will efficiently convert sunlight into electrical power and provide virtually all of our electricity needs. This future is a step closer to being

realized. Detecting low abundance antigens with even the best conventional dye conjugates can be a challenge, as photobleaching can make it difficult to effectively observe and record staining. The exceptional photostability of NC conjugates can provide substantial benefits in the detection of low abundance targets. Due to their narrow and symmetric emission spectra, NCs are also ideal for multicolored, multiplexed fluorescence detection using a single excitation source such as the 405 nm laser.

**Quantum computing** It has been imagined that an arrangement of quantum dots could be an ideal structure for building quantum computing cell. For example if in an arrangement of four quantum dots placed in the corners of square cell two more electrons are introduced then the electrons will tend to occupy the opposite corners to minimize their reciprocal interaction; quantum dots are placed very close to each other so that the electron can tunnel from one quantum dot to another. In this way a logic state can be represented. Further if the electrons are forced to switch into opposite quantum dot corners then another logic state can be represented. The idea that a real possibility for aligning two or more quantum dots in a pattern that could enable the representation of a logic state seemed impossible only few years ago. Researchers from Fujitsu laboratories were the first to achieve such performance [4], by electron beam lithography and local induced oxidation by conductive AFM techniques. They proposed arrangement of four quantum dots that represent a logic state '1' and '0' arrangement of GaAs quantum dots on a solid substrate achieved by e-beam lithography and conductive AFM. Adapted from Ref. [4], the electron can travel from one corner to the next corner of the square by tunneling.

## I.C Thesis outline

This thesis focuses on studies of spectra of Nanocrystals (NCs) in Poly (methyl methacrylate) – PMMA. A side topic is QD molecules study. In the first

chapter of this dissertation, the history and applications for the NCs and QDs are introduced.

The second chapter gives a detail theoretical and systematic description for the energy structure of the QDs and a quantum mechanical tunneling model for coupled quantum dots (QDs) ensembles.

The third chapter introduces two characterization techniques we used for CdSe/ZnS nanocrystals in this thesis.

Incorporation of NCs into thick bulk polymer matrix is a challenging but promising technique. The forth chapter is one method we adopted to achieve such task. Characteristics of ensemble NCs in PMMA is specially studied. In addition, we also incorporate them in negative photon resist SU-8. Photoluminescence has been measured and compared.

In the fifth chapter we have investigated spectral switching between two states in the PL and random spectral shifts from single CdSe/ZnS colloidal nanocrystals in PMMA. Fluorescence quenching and Photo-enhanced luminescence are studied. In higher pump intensity, lower energy lines are found and identified as phonon replicas.

As a side topic, self-assembled InAs lateral Double Quantum Dots(DQDs) achieved using GSMBE under As<sub>2</sub> overpressure are studied in chapter six. The temperature dependence and power dependence of PL are investigated. Rapid thermal annealing effect on DQDs is studied too.

## II

# Quantum dot energy levels calculation

Quantum size effect occurs when size of the nanocrystal becomes comparable to or smaller than the natural length scale of the electron and hole. To be more precise, one can utilize the Bohr radius as a convenient length scale. In general, the Bohr radius of a particle is defined as

$$a_B = \varepsilon \frac{m}{m^*} a_0 \quad (\text{II.1})$$

where  $\varepsilon$  is the dielectric constant of the material,  $m^*$  is the mass of the particle,  $m$  is the rest mass of the electron, and  $a_0$  is the Bohr radius of the hydrogen atom.

**Weak confinement regime** ( $a_e, a_h < R < a_{exc}$ ):

When  $R$  is larger than both  $a_e$  and  $a_h$ , but is smaller than  $a_{exc}$  (i.e., when  $a_e, a_h < R < a_{exc}$ ), only the center-of-mass motion of the exciton can be described as a single, uncharged particle.

**Intermediate confinement regime** ( $a_e > R > a_h$ )

Intermediate confinement regime in a QD corresponds to the situation where the Bohr radius is between  $a_e$  and  $a_h$  (e.g., when  $a_e > R > a_h$ ), one particle

is strongly confined and the other is not. This is due to the difference in the effective masses of electron and hole. In this case, the hole moves in the average potential of the much faster electron and is localized at the center of the NC.

### **Strong confinement regime ( $R \ll a_e, a_h, a_{exc}$ )**

When the nanocrystal radius,  $R$ , is much smaller than  $a_e$ ,  $a_h$  and  $a_{exc}$ , the electron and hole are each strongly confined by the nanocrystal boundary. This is referred to as the strong confinement regime.

## **II.A Density of states in quantum semiconductor structures**

In order to characterize the physical properties like optical transitions, charge transport etc., the information about the number of states  $N(E)$  and density of states  $D(E)$  is very crucial. Density of states is the derivative of the number of states:

$$D(E) = \frac{dN(E)}{dE} \quad (\text{II.2})$$

In real devices,  $N(E)$  and  $D(E)$  will directly affect current levels and signal-to-noise ratios.

There are four configurations of elementary quantum devices: 1) bulk materials in which electrons experience strong quantum confinement in zero dimensions and weak confinement in three dimensions. 2) quantum slabs (or quantum wells) in which electrons experience strong quantum confinement in one dimension and weak confinement (or approximately ‘free’ ) in two dimensions; 3) quantum wires in which electrons experience strong quantum confinement in two dimensions and weak confinement in one dimension; 4) quantum dots in which electrons experience strong quantum confinement in three dimensions and weak confinement

in zero dimensions; and Traditionally weak quantum confinement has been treated using the continuum approximation. This has the advantage of providing a simple analytic result.

### **Bulk material**

For a three-dimensional bulk material, the DOS is defined as the number of available electronic states per unit volume per unit energy at energy  $E$  and is given by

$$N(E) = \frac{\sqrt{2}m_e^{3/2}}{\pi^2\hbar^3}E^{1/2} \quad (\text{II.3})$$

### **Quantum wells**

Passing from three-dimensional bulk to two-dimensional structures, (so called ‘quantum well’) the carrier movement is restricted to a plane. Such two-dimensional systems include thin films, layer structures and superlattices. Now the DOS is modified to the number of available electronic states per unit area per unit energy and is given by

$$N(E) = \frac{m_e}{\pi\hbar^2} \quad (\text{II.4})$$

### **Quantum wires**

Further reduction in the dimensionality of the system ends up in a ‘quantum wire’. Examples of such one-dimensional structures include nanotubes, semiconductor nanowires, and nanorods. For a quantum wire the DOS is defined as the availability of electronic states per unit length per unit energy and is given by

$$N(E) = \frac{\sqrt{2}m_e^{1/2}}{\pi\hbar}E^{-1/2} \quad (\text{II.5})$$

### **Quantum dots**

For a zero dimensional system (QD), the confinement is along all three dimensions and the DOS becomes a delta function. Fig. II.1 schematically shows



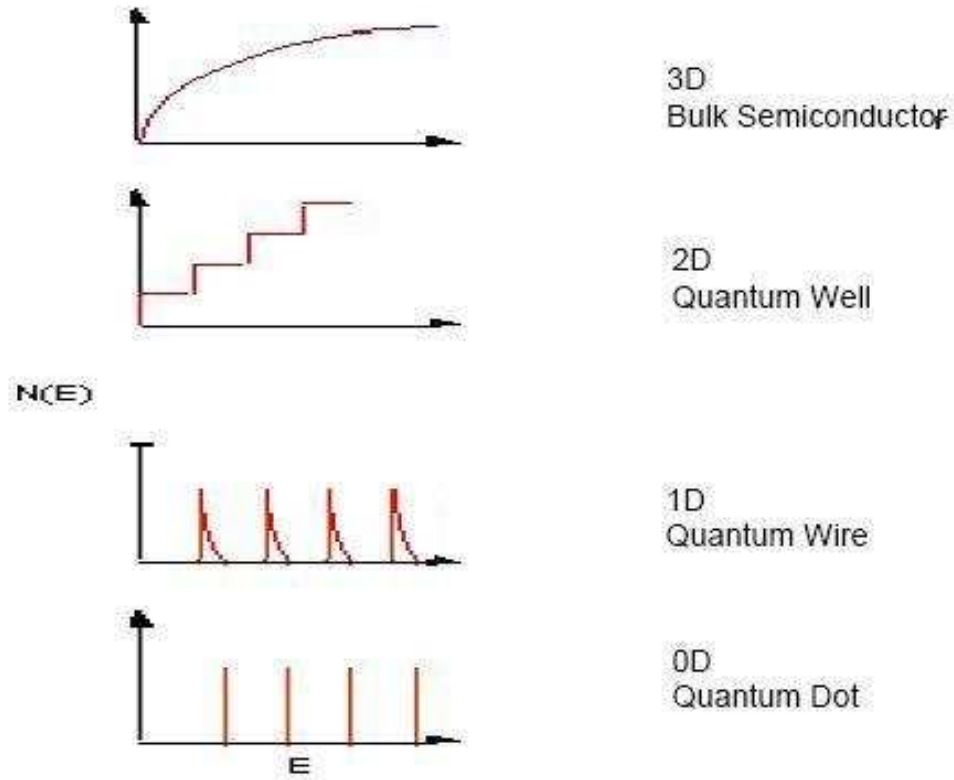


Figure II.1: Schematic representation of density of states  $N(E)$  for an ideal a) Bulk-semiconductor B)Thin film c) Quantum wire d) Quantum dot [1]

the modifications in the DOS as a function of dimension.

## II.B Particle-in-a-spherical potential model

Three-dimensional quantum confinement in CdSe nanocrystal can be treated as a quantum mechanical problem of particle-in-a-spherical potential. This simple model has been improved during last two decades by the addition of appropriate terms to the Hamiltonian. These additional terms contributing to the Hamiltonian originating from realistic situations like electron-hole Coulomb interaction, mixing of hole states, splitting of the states due to exchange-interaction, etc. To calculate the energy level of NC's, one can begin with a very simple model: the particle-in-a-sphere model. In general, this model considers an arbitrary par-

particle of mass  $m_0$  in a spherical potential well  $V(r)$

$$\left[-\frac{\hbar^2}{2m}\nabla^2 + V(\vec{r})\right]\Psi(\vec{r}) = E\Psi(\vec{r}) \quad (\text{II.6})$$

We choose  $V(\vec{r})=V(r)$  centro symmetric and given by

$$V(r) = \begin{cases} 0 & r < a \\ V_0 & r > a \end{cases} \quad (\text{II.7})$$

for NC's of radius  $a$ .

The radial Schrödinger equations in spherical coordinates for the  $l = 0$  ground state are

$$\frac{d^2 R_d(r)}{dr^2} + \frac{2}{r} \frac{dR_d(r)}{dr} + k_{in}^2 R_d(r) = 0, r < a \quad (\text{II.8})$$

,

$$\frac{d^2 R_d(r)}{dr^2} + \frac{2}{r} \frac{dR_d(r)}{dr} - k_{out}^2 R_d(r) = 0, r > a \quad (\text{II.9})$$

,

$$\text{with } k_{in}^2 = \frac{2m^*E}{\hbar^2} \text{ and } k_{out}^2 = \frac{2m_0|E-V_0|}{\hbar^2},$$

where  $m^*$  stands for the electron or hole effective mass. The ground state wave function may be expressed as spherical Bessel functions of first and third kind of zeroth order

$$R_d(r) \propto \begin{cases} j_0(k_{in}r) = \frac{\sin(k_{in}r)}{k_{in}r}, r < a, \\ h_0^{(1)}(k_{out}r) = -\frac{\exp(-k_{out}r)}{k_{out}r}, r > a. \end{cases} \quad (\text{II.10})$$

The proper matching conditions for the two branches of  $R_d(r)$  are obtained by imposing the continuity of the logarithmic derivative at the well edge weighted for the particle masses

$$\frac{1}{m^* R_d(r)} \frac{dR_d(r)}{dr} \Big|_{r \rightarrow a^-} = \frac{1}{m_0 R_d(r)} \frac{dR_d(r)}{dr} \Big|_{r \rightarrow a^+} \quad (\text{II.11})$$

This is done in order to preserve the current probability density at the semiconductor-matrix interface. By substituting

$$m_0 k_{in}^2 a^2 + m^* k_{out}^2 a^2 = \frac{m_0 V_0}{\Delta} \text{ and } \frac{1}{\Delta} = \frac{2m^* a^2}{\hbar^2}$$

in the equation above and after some rearrangements the energy eigenvalues  $E_e$  and  $E_h$  are obtained solving for  $x$  from the equation

$$x \cot(x) = 1 - \left(\frac{m^*}{m_0}\right) - \sqrt{\left(\frac{m^*}{m_0}\right) \left(\frac{V_0}{\Delta} - x^2\right)} \quad (\text{II.12})$$

where  $x = k_{in}a$ .

The Schrödinger equation is solved yielding wave functions

$$\Phi_{n,l,m}(r, \theta, \varphi) = C \frac{j_l(k_{n,l}r) Y_l^m(\theta, \varphi)}{r} \quad (\text{II.13})$$

Where  $C$  is a normalization constant,  $Y_l^m(\theta, \varphi)$  is a spherical harmonic,  $j_l(k_{n,l}r)$  is the  $l$ th-order spherical Bessel function, and

$$k_{n,l} = \frac{\alpha_{n,l}}{a} \quad (\text{II.14})$$

$$E_{n,l} = \frac{\hbar^2 k_{n,l}^2}{2m_0} = \frac{\hbar^2 \alpha_{n,l}^2}{2m_0 a^2} \quad (\text{II.15})$$

Due to the symmetry of the problem, the eigenfunctions are simple atomic-like orbitals which can be labeled by the quantum numbers  $n$  (1, 2, 3...),  $l$  (s, p, d,...), and  $m$ . The energies are identical to the kinetic energy of the free particle, except that the energy is proportional to  $1/a^2$  and, therefore, is strongly dependent on the size of the sphere.

At first glance, this model may not seem useful for the nanocrystal problem. The above particle is confined to an empty sphere, whereas the nanocrystal is filled with semiconductor atoms. However, by a series of approximations, the nanocrystal problem can be reduced to the particle-in-a-sphere form. The photoexcited carriers (electrons and holes) may then be treated as particles inside a sphere of constant potential.

First, the bulk conduction and valence bands are approximated by simple isotropic bands within the effective mass approximation. According to Bloch's theorem, the electronic wave functions in a bulk crystal can be written as

$$\Psi_{nk}(\vec{r}) = u_{nk}(\vec{r}) \exp(i \vec{k} \cdot \vec{r}) \quad (\text{II.16})$$

where  $u_{nk}$  is a function with the periodicity of the crystal lattice and the wave functions are labeled by the band index  $n$  and wave vector  $k$ . The energy of these wave functions is typically described in a band diagram, a plot of  $E$  versus  $k$ . Although band diagrams are in general quite complex and difficult to calculate, in the effective mass approximation the bands are assumed to have simple parabolic forms near extrema in the band diagram. For example, because CdSe is a direct-gap semiconductor, both the valence-band maximum and conduction-band minimum occur at  $k = 0$ . In the effective mass approximation, the energy of the conduction ( $n=c$ ) and valence ( $n=v$ ) bands are approximated as

$$\begin{aligned} E_k^c &= \frac{\hbar^2 k^2}{2m_{eff}^c} + E_g \\ E_k^v &= \frac{\hbar^2 k^2}{2m_{eff}^v} \end{aligned} \quad (\text{II.17})$$

Respectively, where  $E_g$  is the semiconductor bandgap and the energies are relative to the top of the valence band. In this approximation, the carriers behave as free particles with an effective mass,  $m_{eff}^c$ . Graphically, the effective mass accounts for the curvature of the conduction and valence bands at  $k = 0$ . Physically, the effective mass attempts to incorporate the complicated periodic potential felt by the carrier in the lattice. This approximation allows the semiconductor atoms in the lattice to be completely ignored and the electron and hole to be treated as if they were free particles, but with a different mass.

However, to utilize the effective mass approximation in the nanocrystal problem, the crystallites must be treated as a bulk sample. In other words, we assume that the single-particle (electron or hole) wave function can be written in terms of Bloch functions and that the concept of an effective mass still has meaning

in a small quantum dot. If this is reasonable, we can utilize the parabolic bands to determine the electron levels in the nanocrystal. This approximation, sometimes called the envelope function approximation, is valid when the nanocrystal diameter is much larger than the lattice constant of the material. In this case, the single-particle (sp) wave function can be written as a linear combination of Bloch functions:

$$\Psi_{sp}(\vec{r}) = \sum_k C_{nk} u_{nk}(\vec{r}) \exp(i \vec{k} \cdot \vec{r}) \quad (\text{II.18})$$

Where  $C_{nk}$  are expansion coefficients which ensure that the sum satisfies the spherical boundary condition of the nanocrystal. If we further assume that the functions  $u_{nk}$  have a weak  $k$  dependence, then equation can be rewritten as

$$\Psi_{sp}(\vec{r}) = u_{n0}(\vec{r}) \sum_k C_{nk} \exp(i \vec{k} \cdot \vec{r}) = u_{n0}(\vec{r}) f_{sp}(\vec{r}) \quad (\text{II.19})$$

where  $f_{sp}(\vec{r})$  is the single-particle envelope function. Because the periodic function  $u_{n0}$  can be determined within the tight-binding approximation [or linear combination of atomic orbitals approximation] as a sum of atomic wave functions,

$$u_{n0}(\vec{r}) = \sum_i C_n \varphi_n(\vec{r} - \vec{r}_i) \quad (\text{II.20})$$

where the sum is over lattice sites and  $n$  represents the conduction band or valence band for the electron or hole, respectively, the nanocrystal problem is reduced to determining the envelope functions for the single-particle wave functions,  $f_{sp}(\vec{r})$ . Fortunately, this is exactly the problem that is addressed by the particle-in-a-sphere model. For spherically shaped nanocrystals with potential barrier that can be approximated as infinitely high, the envelope functions of the carriers are given by the particle-in-a-sphere solutions. Therefore, each of the electron and hole levels depicted can be described by an atomic-like orbital that is confined within the nanocrystal (1S, 1P, 1D, 2S, etc.). The energy of these levels is described by

Eq. (II.17), with the free particle mass  $m_0$  replaced by  $m_{eff}^{c,v}$ .

The Coulomb interaction between electron and hole is treated in the frame of first-order perturbation theory, thus obtaining

$$\begin{aligned} E_{e-h} &= \left\langle 1s_e, 1s_h \left| \frac{e^2}{4\pi\epsilon_0\epsilon(\bar{r}_0)|\vec{r}_e - \vec{r}_h|} \right| 1s_e, 1s_h \right\rangle \\ &= -\frac{2e^2}{4\pi\epsilon_0\epsilon(\bar{r}_0)} \int_0^a R_d^2(r_h) r_h^2 dr_h \int_0^a R_d^2(r_e) r_e^2 dr_e \end{aligned} \quad (\text{II.21})$$

The integral is calculated only inside the cluster volume since the contribution of the outer volume has been shown to be two or three orders of magnitude smaller than the inner one. A size dependent dielectric constant, developed originally by Hanken and then readapted to treat Coulomb perturbation in NC's, is used

$$\frac{1}{\epsilon(\bar{r}_0)} = \frac{1}{\epsilon_\infty} - \left[ \frac{1}{\epsilon_\infty} - \frac{1}{\epsilon_0} \right] \left[ 1 - \frac{\exp(-\bar{r}_0/\rho_e) + \exp(-\bar{r}_0/\rho_h)}{2} \right] \quad (\text{II.22})$$

Here  $\bar{r}_0$  is the mean electron-hole distance,  $\epsilon_0$  and  $\epsilon_\infty$  are the static and optical dielectric constants and  $\rho_{e,h}$  are given as

$$\rho_{e,h} = \left( \frac{\hbar}{2m_{e,h}^* \omega_{LO}} \right)^{1/2} \quad (\text{II.23})$$

where  $\omega_{LO}$  is the LO phonon frequency. Finally the band gap  $E_g(a)$  for a cluster with radius  $a$  and its variation  $\Delta E_g(a)$  with respect to the bulk value are calculated as

$$E_g(a) = E_e(a) + E_h(a) + E_{e-h}(a) + E_g(bulk) \quad (\text{II.24})$$

$$\Delta E_g(a) = E_e(a) + E_h(a) + E_{e-h}(a) \quad (\text{II.25})$$

So far, this treatment has completely ignored the Coulombic attraction between the electron and the hole, which leads to excitons in the bulk material. Of course, the Coulombic attraction still exists in the nanocrystal. However, how it is included depends on the confinement regime. In the strong confinement regime, another approximation, the strong confinement approximation, is used to treat this term. According to Eq. (II.15), the confinement energy of each carrier scales as  $1/a^2$ . The Coulomb interaction scales as  $1/a$ . In sufficiently small crystallites, the quadratic confinement term dominates. Thus, in the strong confinement regime, the electron and hole can be treated independently and each is described as a particle in a sphere. The Coulomb term may then be added as a first-order energy correction,  $E_c$ . Therefore, using Eqs(II.15), (II.17), and (II.21), the electron-hole pair (ehp) states in nanocrystals are written as

$$\begin{aligned}\Psi_{esp}(\vec{r}_e, \vec{r}_h) &= \Psi_e(\vec{r})\Psi_h(\vec{r}) = u_c f_e(\vec{r}_e) u_v f_h(\vec{r}_h) \\ &= C \left( u_c \frac{j_{L_e}(k_{n_e, L_e} r_e) Y_{L_e}^{m_e}(\theta, \varphi)}{r_e} \right) \left( u_v \frac{j_{L_h}(k_{n_h, L_h} r_h) Y_{L_h}^{m_h}(\theta, \varphi)}{r_h} \right)\end{aligned}\quad (\text{II.26})$$

with energies

$$E_{ehp}(n_h L_h n_e L_e) = E_g + \frac{\hbar^2 \alpha_{n,l}^2}{2a^2} \left\{ \frac{\varphi_{n_h, L_h}^2}{m_{eff}^v} + \frac{\varphi_{n_e, L_e}^2}{m_{eff}^c} \right\} - E_c \quad (\text{II.27})$$

The states are labeled by the quantum numbers  $n_h L_h n_e L_e$ . For example, the lowest-pair state is written as  $1S_h 1S_e$ . For pair states with the electron in the  $1S_e$  level, the first-order Coulomb correction,  $E_c$ , is  $1.8e^2 \varepsilon a$ , where  $\varepsilon$  is the dielectric constant of the semiconductor. Equation II.26 and II.27 are usually referred to as the particle-in-a-sphere solutions to the nanocrystal spectrum.

CdSe is a II-VI semiconductor. Even in the nano regime, the physical size of a CdSe QD is much larger than the lattice constants ( $a = 0.4299$  nm,  $c = 0.701$  nm) [9]. Therefore, it is possible to assume the same crystalline structure as for the bulk material. At the same time nanocrystals open the opportunity to study ‘size induced quantization effects’. Because of the close correlation with

the bulk crystal structure, the description of nanocrystals can be developed from bulk solid state physics and quantum mechanics. The quantum size effect can be explained qualitatively by considering a particle-in-a-box like situation where the energy separation between the levels increases as the dimensions of the box are reduced. Thus one can observe an increase in the band gap of the semiconductor while decreasing the particle size. Quantitative theoretical approaches have been employed during the last two decades. For example, effective mass approximations (EMA) [10, 11] and empirical tight-binding methods (ETBM) [12].

## II.C Optical transition probabilities and dipole moment

The probability to make an optical transition from the ground state,  $|0\rangle$ , to a particular electron-hole pair state is given by the dipole matrix element

$$P = \left| \langle \Psi_{ehp} | \vec{e} \cdot \hat{p} | 0 \rangle \right|^2 \quad (\text{II.28})$$

Where  $\vec{e}$  is the polarization vector of the light and  $\hat{p}$  is the momentum operator. In the strong confinement regime, where the carriers are treated independently, the equation above is commonly rewritten in terms of the single-particle states:

$$P = \left| \langle \Psi_e | \vec{e} \cdot \hat{p} | \Psi_h \rangle \right|^2 \quad (\text{II.29})$$

Because the envelope functions are slowly varying in terms of  $\vec{r}$ , the operator  $\hat{p}$  acts only on the unit cell portion ( $u_{nk}$ ) of the wave function. The equation is further simplified to

$$P = |\langle u_c | \vec{e} \cdot \vec{p} | u_v \rangle|^2 |\langle f_e | f_h \rangle|^2 \quad (\text{II.30})$$

In the particle-in-a-sphere model, this yields



$$P = |\langle u_c | \vec{e} \bullet \vec{p} | u_v \rangle|^2 \delta_{n_e, n_h} \delta_{L_e, L_h} \quad (\text{II.31})$$

Due to the orthonormality of the envelope functions. Therefore, simple selection rules ( $\Delta n = 0$  and  $\Delta L = 0$ ) are obtained.

$$\varepsilon' = \varepsilon_\infty + \frac{\varepsilon_d}{1 + (\varpi\tau)^2},$$

and

$$\varepsilon = \frac{\varepsilon_d}{1 + (\varpi\tau)^2} \varpi\tau$$

Where  $\varepsilon_\infty$  is the high frequency limit of the dielectric constant of the spheres plus the static dielectric constant of the solvent and  $\varpi$  is the angular frequency. The dipole contribution,  $\varepsilon_d$ , and the rotation relaxation time,  $\tau$ , are given by

$$\varepsilon_d = \frac{4\pi n\mu^2}{3kT} \quad (\text{II.32})$$

and

$$\tau = \frac{4\pi\eta a^3}{kT} \quad (\text{II.33})$$

where  $n$  is the concentration of the dipole spheres,  $\mu$  is the screened dipole moment,  $\eta$  is the viscosity of the solvent, and  $a$  is the hydrodynamic radius.

Colloidal NC's of CdSe exhibit large dipole moments (41-98 D) and linearly dependent on the radius of the semiconductor core [13].

## II.D Tunneling transport and diffusion in weakly coupled quantum dot ensembles

The asymmetric broadening together with the shift of the PL peak towards higher energies are first indications for the formation of extended states in the QDMs due to tunnel coupling. Tunnel coupling of the QD ground states cre-

ates extended states with a distinct energy separation determined by the coupling strength.

Especially for heavy holes, the quantum-mechanical coupling between adjacent QDs may be weak, while charge capture is from a wetting layer that acts as a thermal reservoir. We consider only the case when charge being initially captured by a QD with subsequent jumps to adjacent QDs. A continuity equation can then be written to describe the hole density, given by

$$\frac{\delta n_h(\vec{r}, t)}{\delta x} = \frac{\vec{J}(\vec{r}, t)}{q} + \nabla \bullet D_h(\vec{r}) \nabla n_h(\vec{r}, t) - P[n_e(\vec{r}, t)] \frac{n_h(\vec{r}, t)}{\tau_{sp}} - \frac{n_h(\vec{r}, t)}{\tau_{nr}} \quad (\text{II.34})$$

where  $n_{h,e}(\vec{r}, t)$  is the hole (electron) density in a QD at  $\vec{r}$ ,  $\frac{\vec{J}(\vec{r}, t)}{q}$  is an external source,  $D_h$  is the hole diffusion rate,  $\tau_{sp}$  is the spontaneous lifetime of an electron-hole pair confined in the same QD,  $P[n_e(\vec{r}, t)]$  is the probability that a QD that contains a hole also contains an electron, and  $\tau_{nr}$  is a nonradiative lifetime. The position  $\vec{r}$ , takes discrete values at each QD with differentials taken as spatial separations between QDs. Charge neutrality is not assumed in each QD, but is assumed for the average carrier densities. At low excitation the QDs are nearly empty. In the absence of selective electron and hole capture by the same QD, the recombination rate becomes limited by  $\tau_{nr}$ , which may exceed tens of nanoseconds. Therefore, even small tunneling rates, such as expected for heavy holes, may lead to modification of the ensemble spectra at low bias.

A charge's wave function is localized to a QD through superposition of energy eigenmodes that constructively interfere to give an amplitude only within that QD. For weak coupling we ignore the influence of nearest neighbors in calculating the jump probability between two adjacent QDs. The assumption of weak coupling requires including only the first two energy eigenstates of the two QD systems. We label the QDs as QD1 and QD2, and use the orthogonal wave-functions  $\psi_1(\vec{r})$  and  $\psi_2(\vec{r})$  to represent the charge localized to the respective QD.

The two lowest-energy eigenstates used to construct  $\psi_1(\vec{r})$  and  $\psi_2(\vec{r})$  are

taken as  $\psi_e(\vec{r})$  and  $\psi_o(\vec{r})$ , which have eigenfrequencies of  $\omega_e$  and  $\omega_o$ , respectively, with  $\Delta\varpi = \omega_o - \omega_e$ . For symmetrical QDs,  $\psi_e(\vec{r})$  and  $\psi_o(\vec{r})$  are the even and odd wave functions.

Taking  $\psi_1(\vec{r})$  for the larger of asymmetric QDs, its overlap is higher for  $\psi_e(\vec{r})$  with a thermal probability of existence given by

$$P_{\psi_1} = \frac{(1/2)e^{(\hbar\Delta\omega)/(4KT)} + |\langle\psi_e | \psi_1\rangle|^2 \sinh[\hbar\Delta\varpi/(4KT)]}{\cosh[\hbar\Delta\varpi/(4KT)]} \quad (\text{II.35})$$

where  $\hbar$  is the Planck constant and  $KT$  is the thermal energy. For  $\psi_2(\vec{r})$ , the thermal probability is

$$P_{\psi_2} = \frac{(1/2)e^{-(\hbar\Delta\omega)/(4KT)} + |\langle\psi_o | \psi_2\rangle|^2 \sinh[\hbar\Delta\varpi/(4KT)]}{\cosh[\hbar\Delta\varpi/(4KT)]} \quad (\text{II.36})$$

For  $\hbar\Delta\varpi \gg KT$  only the even state  $\psi_e(\vec{r})$  has a significant probability of being occupied, but for large asymmetry in QD sizes we also have  $|\langle\psi_e | \psi_1\rangle| \rightarrow 1$ . Therefore, low temperature favors trapping in the largest QDs despite the presence of quantum-mechanical coupling.

Assuming that the charge is initially localized to QD1, the probability of finding the charge later in QD2 is due to the free evolution of the time-dependent wave function, but with evolution interrupted by phase breaking. The wave function is given by

$$\psi(\vec{r}, t) = e^{-i(\omega_e + \omega_o)t/2} \{ [\cos(\Delta\omega t/2) + K_1 \sin(\Delta\omega t/2)] \psi_1(\vec{r}) + K_2 \sin(\Delta\omega t/2) \psi_2(\vec{r}) \} \quad (\text{II.37})$$

where the coefficients are given by  $|K_2| = \sqrt{1 + |K_1|^2}$  and

$$K_1 = i \frac{\langle\psi_e | \psi_1\rangle \langle\psi_o | \psi_2\rangle + \langle\psi_e | \psi_2\rangle \langle\psi_o | \psi_1\rangle}{\langle\psi_e | \psi_1\rangle \langle\psi_o | \psi_2\rangle - \langle\psi_e | \psi_2\rangle \langle\psi_o | \psi_1\rangle} \quad (\text{II.38})$$

Equation (II.37) describes the coherent oscillation of the wave function from QD1 to QD2 and back again, with the oscillation frequency of  $\Delta\varpi$ . However,

only for the case of symmetrical QDs will the wave function attain an equal amplitude for occupation of either QD1 or QD2 during an oscillation cycle. Increasing asymmetry increases the oscillation frequency while the maximum amplitude for occupation in the adjacent well decreases. With the charge in QD1 at  $t=0$  and in the absence of scattering, the probability of finding the charge  $\Delta t$  later in QD2 is  $|K_2|^2 \sin^2(\Delta\omega\Delta t/2)$ .

For weakly coupled QDs the oscillation frequency for the coherent charge transfer can be much slower than other relevant time scales. Dephasing of the wave function due to reservoir coupling is known to reduce the tunneling rate at resonance and lead to sequential tunneling and charge localization. Measurements for one-dimensional AlGaAs/GaAs mesoscopic wires place the dephasing time as  $\tau_\phi \sim 10$  ps at low temperature, and there is some evidence to suggest that it is longer for QDs. For weak coupling we assume  $\Delta\varpi < \tau_\phi^{-1}$ . Averaging  $\Delta t$  over an exponential distribution with a characteristic time constant of  $\tau_\phi$  as  $|K_2|^2 \Delta\omega^2 / [2(\Delta\varpi^2 + \tau_\phi^{-2})]$ . From this jump probability, a diffusion coefficient due to tunneling is given by

$$D \approx \frac{\xi}{4n_{QD}} \frac{|K_2|^2 \Delta\varpi^2}{\tau_\phi(\Delta\omega^2 + \tau_\phi^{-2})} \quad (\text{II.39})$$

where  $n_{QD}$  is the local QD density, and  $\xi$  is on the order of unity and set by the positions of nearest neighbors.

# III

## Characterization of the CdSe/ZnS nanocrystals

### III.A Photoluminescence measurement

In a quasi zero-dimensional structure like NCs and QDs, the physical size is small enough such that its electronic states begin to resemble those of an atom or molecule. Photoluminescence (PL) measurements are the basic tool that allow for the investigation of discrete energy levels of such nano particles. A photon of appropriate wavelength excites an electron from the valence band (VB) to the conduction band (CB) and creates an exciton. Bandedge excitation promotes the electron and hole directly into the discrete levels while high frequency photons excite the carriers to the continuum (solid upward arrow). At low excitation intensities the excited charge carriers relax nonradiatively through many discrete excited states to the bandedge states. Such intraband relaxation of electrons and holes are monitored with femtosecond time-resolved pump-probe measurements [14]. For electrons, this relaxation process is on a time scale of a few hundred femtoseconds and that for holes is a few picoseconds. However, for bulk II-VI semiconductors, intraband relaxation rates are very fast due to efficient coupling of the dynamics of the charge carriers to the lattice as well as due to diffusion to

defect states. High nonradiative relaxation rates are observed in the case of bulk materials because of a high density of electron and phonon states [15]. Interband carrier relaxation from the bandedge states of a QD depends on the rates of three competing processes: Radiative recombination (i), Nonradiative recombination (ii) and Trap processes (iii).

(i) Radiative recombination

Radiative recombination of an electron-hole pair emits photon. PL measurements are the basic tool to elucidate information carried by the emitted photons. In PL spectroscopy, radiation intensity versus wavelength of the emitted photons is registered. PL spectrum provides information on the energy levels of the QDs.

(ii) Nonradiative recombination

The most significant nonradiative relaxation processes of excitons in semiconductor QDs are the interaction with phonons and the Auger process [16]. Exciton-phonon interaction in NCs is of great importance. This controls the energy relaxation and intrinsic dephasing processes [17]. As a result, the absorption and emission linewidths and the luminescence Stokes shifts depend on the strength of the exciton-phonon interaction. For a CdSe QD with a diameter of 2 nm, the energy separation between first and second excited state is nearly 200 meV. The longitudinal optical phonon energy,  $E_{LO}$ , is 26 meV [18]. Since the dispersion curve of optical phonons is nearly independent of the wave vector and the absence of intermediate states between the adjacent excited states, the relaxation between excited states in NCs by the emission of multiple LO-phonons is inhibited by the 'phonon bottleneck'. However, multiple emissions of acoustic phonons appear to be the main relaxation mechanism. Homogeneous spectral line-shapes are determined at high temperatures by dynamic processes which destroy the phase coherence of the excited state. Details of the exciton-phonon interaction can be obtained from resonant Raman scattering experiments [19].

Auger processes are very efficient in QDs than in bulk materials. This is

because, in QDs, with a radius smaller than exciton Bohr radius  $a_B$ , multiple excitons can be occupied by a volume which is smaller than excitonic volume  $V \sim a_B^3$ . This is possible because of strong carrier confinement which increases the overlap between carrier wavefunctions and enhances Coulombic interactions. Not only that, because of the restrictions imposed by energy and momentum conservation, such multiparticle Auger transitions are relatively inefficient in bulk semiconductors. However, this is considerably enhanced in QDs, because of the breakdown in translation symmetry which leads to a relaxation in momentum conservation [20]. A QD may carry two electron-hole pairs within the lifetime of the excited state. Energy of one of the pairs is transferred to the remaining electron (hole). Thus in the case of Auger relaxation of a biexciton in a neutral QD, the excited carrier is still confined in the QD. Auger relaxation can also cause charging of a QD, generally known as Autoionization. Due to the high density of states far from the bandedge, creation of a second electron-hole pair become possible even in an ionized QD. The electron-hole pair couples to the remaining charge carrier resulting in very fast non-radiative decays which is much faster than the radiative lifetime [21]. Due to these processes a charged QD appears as a dark QD.

### (iii) Trap processes

A trap can be considered as a localized electronic state which captures charge carriers. Unlike the band levels that extend throughout the whole crystal, the trap levels exist only in relatively small regions of space around the trap potential. If the state is highly localized so that an electron bound to the trap potential has a wavefunction that extends only as far as the nearest neighbors, the uncertainty in location is small. Such a trap potential is known as deep trap. The energy level for a deep trap in an E vs k diagram, therefore, extends over a wide range of k values. For shallow traps, the uncertainty in location is large, and therefore the corresponding uncertainty in momentum is small. There are several reasons for the origin of such localized trap potentials.

(a) Imperfections: There are in general, three types of imperfections.

Point imperfections due to missing or misplaced atoms that belong to the crystal (usually called defects), point imperfections due to foreign atoms that do not belong to the crystal (usually called impurities), and large structural imperfections such as imperfection complexes, dislocation or grain boundaries [22].

(b) Surface-related states: The high surface-to-volume ratio of NCs suggests that the surface properties should have significant role on their optical properties. Surface-related states are energetically positioned within the band gap of QDs [23]. These surface traps are associated with surface reconstruction in the atomic positions, stoichiometric defects ( $\text{Cd}^{2+}$ ,  $\text{Zn}^{2+}$ ,  $\text{Se}^{2-}$  and  $\text{S}^{2-}$  vacancies in the case of  $\text{CdSe/ZnS}$  QDs), dangling bonds, external atoms (like oxygen) associated with contamination or chemical/physical changes in the exposed surface and interfacial defects due to lattice mismatch [24].

(c) Self-trapped states:

The carriers are most likely trapped in the states localized at the QD-matrix interface [25, 26] or outside the QD in the surrounding matrix [27]. The self-trapped states are significant when trapping of carriers in the surrounding matrix, for example polymers, occur. Charges injected into polymers induce localized acceptor states. These acceptor states are characterized by atomic and electronic relaxations of the molecular moiety on which the charge is localized and of the polymer matrix surrounding the charge. These kinds of energetically relaxed states are not the intrinsic states of a neutral polymer. A charge inside a dielectric matrix produces a polarization in the dielectric as a consequence of its Coulomb field. In turn, the polarized surroundings will produce a reaction field at the location of the charge. The interaction of the charge with this reaction field stabilizes the charge in the dielectric matrix. This is known as self-trapping. The crucial parameters describing the process of localization and trapping is the relation between the spatial overlap of the electron/hole wavefunction with that of trap potential as well as the depth of local potential fluctuations. The trapping process decreases overlap of electron-hole wavefunction and therefore increases the recombination



time. In QDs the most likely trap process is the capture of an electron or hole by a local potential in the interface region or in the surrounding matrix. However, in QDs the interface related trap processes modifies the electronic properties much more than an impurity in the bulk semiconductor usually does. Trapping not only changes the recombination process, but can also cause lattice distortion, alternate the potential barrier, or active chemical reaction. After the trap process of optically excited electron or hole, the QD can be considered a completely changed new object. Radiative relaxation from the trap states to the ground state of a QD is registered as red-shifted trap luminescence with respect to bandedge emission. During the course of photoluminescence cycles (repeated laser excitation, exciton formation and radiative recombination), the QD turns “dark” when an electron or hole (most probably electron due to extended wavefunction of the electron into the matrix where the QDs are embedded [28]) from the exciton localizes (or traps) near the surface of the QD leaving a delocalized charge carrier inside the QD. The energy transfer from the exciton to the delocalized charge carrier and subsequent nonradiative relaxation of the charge carrier (250 fs - 3 ps) [29] is much faster than the radiative lifetime of the exciton ( $\sim 20$  ns). Therefore, a QD with a delocalized charge carrier is a “dark” QD. The “dark” QD can turn to a “bright” QD [30] when: (i) The delocalized charge within the QD is also get localized at the interface between core and shell. Localization causes discretization of the energy levels and reduces the spatial overlap between exciton wavefunction and the lone charge carrier and therefore the energy transfer as well. However, decoration of the charges at the QD surface or at the close vicinity creates a surface dipole which modifies the local electric field. This causes Stark shift in the emission frequency. Diffusion of the charges between the trap sites create time dependent dipole followed by a time dependent emission frequency. (ii) The charge localized in the trap relaxes back into the QD core and recombining with the delocalized charge within the QD. The emission frequency will be same as that of a neutral particle after the dark period provided the localization and recapture of the charges

does not induce any dipole in the close vicinity of the particle. As the size of the QD decreases, the competition between radiative recombination and trapping process increases. Portion of the atoms which are influenced by surface defects, is drastically increasing with decreasing size. At the same time increased overlap of electron-hole wave function in small QDs enhances radiative recombination.

### III.B Single nano-object spectroscopy

In less than 20 years, single nano-object spectroscopy has evolved from a specialized variety of optical spectroscopy at low temperatures into a versatile tool used to address a broad range of questions in physics, chemistry, biology, and material science. It started in 1989 with the experiments of Kador and Moerner [31], who detected the absorption signal of an individual dye molecule embedded in a solid matrix at liquid helium temperatures. Soon after that, Orrit et al.[32] introduced single-molecule spectroscopy by means of fluorescence excitation, a more straightforward technique that yielded better signal-to-noise ratios than the absorption method did. A few years later, Wild and coworkers demonstrated the feasibility of near-field single-molecule microscopy at low temperatures [33], which can isolate the chromophores spatially in a suitably diluted sample. This optical method provides access to the absorption, emission, or excitation spectra of single nano-objects and can determine either the positions of these objects with less than  $\lambda/2$  accuracy or the full three-dimensional orientation of their transition dipole moments. Recent work aims at using single molecules as nanoparts or nanoelements in a variety of molecular-scale devices, from triggered sources of single photons to single-molecular switches. The combination of microscopy with time- and frequency-resolved spectroscopy is opening a wide field of new and exciting applications to individual nano-objects.

Room-temperature investigations of individual chromophores were first conducted by Betzig and coworkers [34], who used near-field optics to achieve

subdiffraction-limit excitation volumes, thus reducing the background noise. Prior investigations of fluorophores diffusing in solution [35] already suggested that detecting immobilized single fluorophores by far-field confocal microscopy should be possible. This was first realized by Trautman et al.[36] and Xie and coworkers. [37] Since then, far-field microscopy of individual fluorophores has become an important technique in many fields of science. The evolution of nanotechnology started with the invention of scanning tunneling microscopy (STM) and atomic force microscopy (AFM) in the 1980's. These scanning probe microscopic (SPM) techniques could not only provide insight into the structure and dynamics at nanometer scale but also image and manipulate single atoms and molecules. Besides SPM, single chromophore sensitivity can also be reached by far-field optical method known as single chromophore detection (SCD). Here, microscopic approach is combined with spectroscopic techniques [38]. The study of single nano-objects (molecules, NCs, metal colloids etc.) is a modern tool for optical diagnosis. The major limitation in single chromophore detection at RT results from limited number of photons emitted by the single nano-object. However, the invention of highly sensitive detectors like avalanche photodiode (APD) and intensified charge coupled device (I-CCD) promoted the detection limit down to a single chromophore level with advanced optical detection techniques like confocal and wide field optical video microscopy. This can be achieved by diluting the chromophore in the order of nano molar concentration in a non-absorbing medium and selecting a single molecule or single QD in an optical near field or a diffraction-limited spot. The disadvantage of conventional spectroscopy is the loss of spectral details due to ensemble averaging effects. However, single chromophore spectroscopy has been successful in revealing many new phenomena which are obscured in ensemble measurements. In addition to spatial resolution, single chromophore spectroscopy also provides temporal information on a single chromophore level such as fluorescence lifetime, non-radiative relaxation, intersystem crossing rates, evolution of excited- and trapped-state population. Direct observation of single enzyme reactions [39] is promoted by detection

and spectroscopy on a single molecule level. Even optical access to molecules [40] is possible with SCD.

Commonly adopted optical far field techniques for the detection of single NCs are wide-field video microscopy and confocal microscopy. The advantage of wide-field video microscopy over confocal microscopy is the parallel detection of many QDs. This reduces the temporal fluctuations of the experimental parameters (e.g., intensity of the excitation laser, ambient conditions etc.)

# IV

## PMMA nanocrystals composites fabricated via use of pre-polymerization

### IV.A Introduction

Utilizing nanoscale quantum confinement of semiconductor materials in 1-D (quantum wells), 2-D (quantum wires), and 3-D (quantum dots) spaces is one of the most promising approaches to enhance and engineer linear and nonlinear properties of optical and optoelectronic materials. Since the first quantum dots were made by use of the etched quantum well by Reed [41], various methods of fabricating semiconductor QDs have been investigated. Self-organized growth of QDs has been widely used to make electronic and optoelectronic devices from the epitaxial structure to the random arrangement of islets by means of the Stranski-Krastanow transition [42]. These types of structures rely on complicated processing and high cost with metal-organic chemical vapor deposition (MOCVD) and molecular beam epitaxy (MBE) facilities.

Recently, semiconductor NCs fabricated in colloidal solution via synthetic routes have been shown to be promising alternative fabrication method of QDs

[43, 44, 45]. The benefits for NCs over self-assembled QDs is that NCs can be incorporated into a variety of polymers as well as thin films of bulk semiconductors. They can also be manipulated into close packed glassy thin films, ordered three-dimensional superlattices (colloidal crystals), or linked to form NC molecules. Exceptional flexibility and structural control distinguish nanocrystallite QDs from the more traditional QD structures fabricated using epitaxial growth techniques. In addition, they facilitate the study of some potentially novel QD physics, which may be difficult or inaccessible with epitaxially grown dots.

One of the approaches uses incorporation of NCs into polymer thin films and has shown a great promise [46, 47]. However, the incorporation of NCs into thick bulk polymer matrix has remained challenging. A large number of complicated synthesis techniques have been investigated to prevent aggregation of NCs during the polymerization process when NCs are dissolved in vinyl monomers and processed to radical polymerization. These methods include: Gao et. al. [48] used Pb methacrylate to make PbS NCs, then polymerized the vinyl to form solid polymer composite. Frog et. al. [49] incorporated NCs within a polymer containing phosphine donors attached to the polymer backbone to form polymerized NCs composite film. Lee et. al. [50] used the same phosphine ligand covering NCs to prevent the NCs from phase separating during polymerization to form solid composite polymer. Zhang et. al [51] utilized the polymerizable surfactant to transfer NCs to styrene solution and polymerized to solid polymer composite.

In this chapter, we describe a simple method of pre-polymerizing monomer NC solution to prevent the NCs from separating away from the polymer matrix. The pre-polymerized polymer could be cast into various molds to form solid-state polymer-NC composites via a complete polymerization step. This approach could be used for fabrication of various microstructures [52]. Moreover, its dilute solution can also be used to form films by spin coating, which can be further lithographically processed to construct nanostructures for realization of photonic devices [53].

## IV.B Incorporation of NCs into thick bulk polymer matrix using pre-polymerization

Our process is based on radical polymerization of methyl methacrylate (MMA). Under vigorous stirring, a quantity of nanoparticle colloidal solution of 620 nm CdSe/ZnS core shell tri-n-octylphosphine oxide (TOPO) capped quantum dots in toluene (Evident Technologies) is slowly added into the distilled MMA with a concentration of radical initiator azobisisobutyronitrile (AIBN) of 0.1% in weight. The MMA QD solution was heated in a thermostatic water bath at about  $90^{\circ}\text{C}$  for 20 min. To get the suitable viscosity, or prepolymerization, and then poured into molds, which were put into an oven at  $60^{\circ}\text{C}$  for postpolymerization. Generally, the whole process in the oven is conducted for more than 20 hours.

It is commonly known that uniform dispersion of nanoparticles in the final solid phase polymer-QD composites is hampered by separation and cluster aggregation within the matrix. To minimize these effects, ligand and other surfactant were used to envelope the nanoparticles to prevent aggregation during the polymerization of the monomers [48, 49, 50, 51]. In contrast, our method does not use such surfactants, indicating that the NCs are only suspended in the MMA monomers during polymerization step. The polymerization procedure of MMA to its polymer form, or poly methyl methacrylate (PMMA), could influence the NC distribution in the polymerized PMMA.

We conducted a comparison experiment on complete polymerization into PMMA of the pre-polymerized and non-pre-polymerized MMA mixed with NCs. In this experiment we prepared 4 ml of 0.6 mg/ml NC-MMA solution of 0.1% AIBN which was spilt equally into two identical glass vials. One of the vials was placed into thermostatic water bath at  $90^{\circ}\text{C}$  for about 20 min. for pre-polymerization. Later it was transferred into oven at  $60^{\circ}\text{C}$  together with another vial containing non-pre-polymerized NC MMA solution. The two samples were kept in the oven for 20 hours.

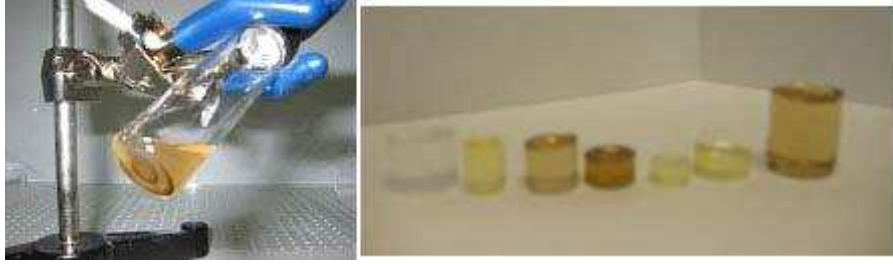


Figure IV.1: Originally NCs were suspended in liquid. After processing, they were incorporated in PMMA solid matrix. The pre-polymerized polymer could be cast into various molds to form solid-state polymer with various shape.

The appearance of the two solidified composite polymers was completely different as shown in Fig. IV.2. For the prepolymerization, the color is uniform, and there were no observable defects, as shown in Fig. IV.2(a) (right). The directly polymerized counterpart, however, exhibits severe non-uniformity, as shown in Fig. IV.2(a) (left). From the close-up in Fig. IV.2(a), large bunches of clusters can be observed, indicating the agglomeration of the NCs after direct polymerization. That is why attempts to obtain such composites from radical polymerization with the vinyl monomers showed limited success [50]. The sideview (the left part of Fig. IV.2(b)) also shows non-uniformity of NCs distribution in the vertical direction. In fact, the NCs have clustered (i.e., split) into two parts with almost no NCs in the middle region of the sample.

The non-uniformity can be explained as follows: in general, the NCs dissolve in MMA easier than in polymerized PMMA due to the difference in the viscosity. Therefore, for direct polymerization process during 20 hours, when MMA is polymerized to PMMA, the large molecular mass PMMA with enveloped NCs sinks to the bottom of the container, whereas the non-polymerized MMA moves towards the top. Furthermore, due to the higher solubility of NCs in non-polymerized MMA, the non-wrapped NCs diffuse to the top MMA layer, leaving a gap in the middle region. After the polymerization process is complete, the composite has a non-uniform distribution of NCs in vertical direction as confirmed by our experi-



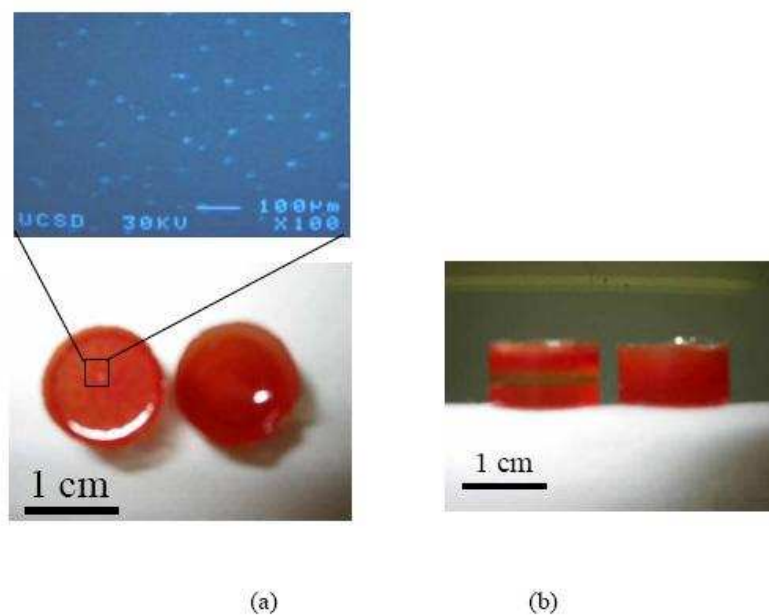


Figure IV.2: a) For the prepolymerization, the color is uniform, as shown in the right figure. The directly polymerized counterpart, however, exhibits severe non-uniformity, as shown in the left figure. From the close-up, large bunches of clusters can be observed.

ments.

It is obvious that the aggregation of NCs needs adequate control for most of the potential applications. In contrast, pre-polymerization of MMA-NC solution, processed for a short time at a higher temperature, assures the rapid polymerization of couples of MMA monomers to form oligomers, which envelopes the NCs and prevents them from aggregation. Moreover, the great compatibility of the oligomer in both MMA and polymerized PMMA assures that the capped NCs will disperse uniformly during the post polymerization process. This also explains the formation of the bottom section of the PMMA-NC composite in the direct polymerization (Fig. IV.2(b) (left)), in which the partially formed oligomers capping the NCs polymerize to PMMA-NC composite, coalesce and descend. It should be mentioned that the capping ligand on the NCs, TOPO, plays an important role in solubilizing the NCs in the MMA. Clear PMMA-NC composites have also been produced with different sizes of CdSe/ZnS and PbSe colloidal NCs using above procedure.

For characterization of NC properties in the PMMA-NC composites fabricated using the pre-polymerization approach, we conducted experiments on absorption and photoluminescence (PL). An argon laser with wavelength of 488 nm was used to pump for PL measurements, whereas LS-1 broadband (Ocean Optics) halogen lamp was used to measure the absorption spectrum. We used CVI DK480 monochromator and Hamamatsu H7421-50 (GaAs) photocounter to measure the absorption as well as PL from the samples. First, for comparison purposes, the spectra of NCs in toluene solution of concentration 2.5 mg/ml were measured as shown in the Fig. IV.3(a). The first absorption peak of the CdSe/ZnS NCs is 612 nm, and its PL peak is at 625 nm with full width half maximum (FWHM) of about 16 nm. Fig. IV.3(b) shows the absorption and PL spectra of PMMA-NC composite in a slide-like shape with thickness of 1 mm produced by casting the pre-polymerized MMA polymer (0.6 mg/ml) into a flat chamber made from glass slides. Absorption spectrum of a 1 mm thick pure PMMA slide is also shown

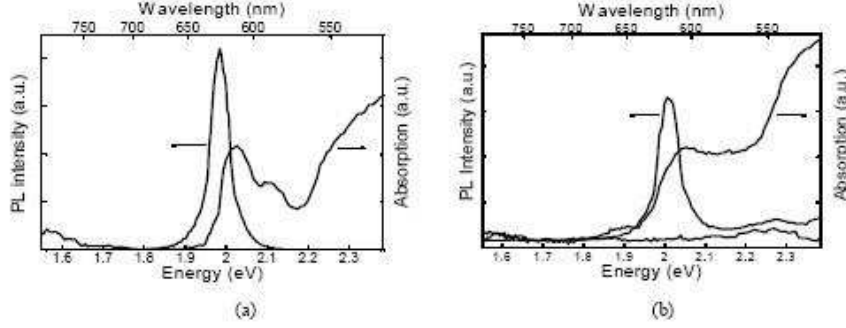


Figure IV.3: Absorption and PL spectra of NCs in (a) toluene solution and (b) PMMA-NC composite, where the dash line shows the absorption spectrum of a 1 mm thick pure PMMA slide.

for comparison, demonstrating that pure PMMA material absorbs little light at visible and near infrared regions. The PL peak of the solid PMMA-NC composite matrix occurs at about 617 nm with FWHM of about 19 nm. The blue shift of the PL peak seems to be in contradiction with Ref. [50], where a PL peak of 625 nm in toluene shifted approximately 17 nm to longer wavelength when incorporated into the composite matrix. The red shift of Ref. [50] was interpreted as due to light reabsorption by the larger NCs in the distribution as the emitted light from the smaller NCs travels along the composite rod. Because of different synthesis of colloidal NCs, a direct comparison between these two procedures cannot be conducted.

From Fig. IV.3(b), we observe that the first absorption peak of PMMA-NC composite sample occurs at about 602 nm, showing a shift to shorter wavelength (blue shift) by about 10 nm as compared to the absorption maximum of 612 nm measured for NCs in toluene. Blue shift in the PL and absorption spectra had been reported for different kinds of quantum dots when exposed in air (oxygen) [54, 55, 56], even was utilized for patterning [57]. For our case, the blue shift could not be attributed to the oxidation of the NCs surface. Detail analysis will be provided in the next chapter. Our method of preparing PMMA-NC composites could

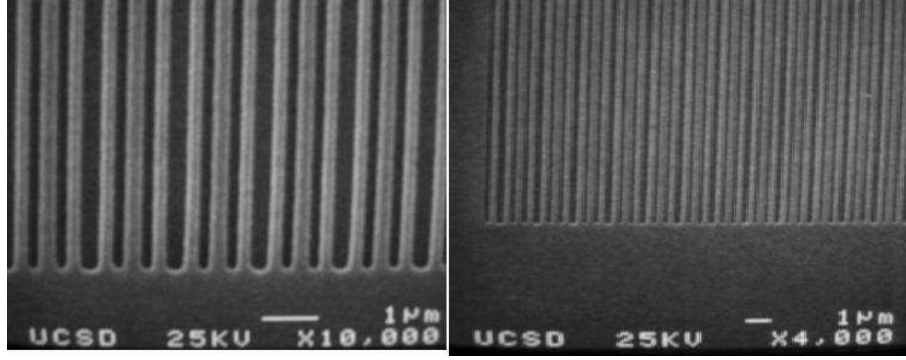


Figure IV.4: NCs in PMMA gratings

be used not only to achieve NC polymer displays [46] and precisely duplicated microstructures [52], but also be used for direct writing electron beam lithography to make nanostructures and other nanoscale patterned polymer-NC structures by exploiting the nature of sensitivity of PMMA to an electron beam. This fabrication approach may be very attractive for numerous applications of NCs composites for photonics and optoelectronics.

For the proof-of-concept experiment the prepolymerized PMMA-NC composite was dissolved in MMA and then spin coated on a  $SiO_2$  substrate. After the soft baking step, the PMMA-NC layer was patterned by E-beam lithography in a modified SEM (JEOL JSM-6400), followed by development in solution of methyl isobutyl ketone (MIBK) and isopropyl alcohol (IPA) of MIBK:IPA=1:2.

Fig. IV.4 shows an SEM photograph of a structure with  $1.5 \mu m$  period and feature sizes of 200 and 300 nm. Different from the photoactivation of NCs for large structure patterning [57], and selfassembly for small structure [56], the grating structure shown in Fig. IV.4 demonstrates that our PMMA-NC composite is a good E-beam sensitive material for patterning nanostructures. Although its organic matrix is not as environmentally stable as semiconductor QDs structure fabricated via MBE and MOCVD techniques, its flexibility and compatibility with organic optoelectronics make it a very attractive candidate for many applications. Use of PMMA-NC composite as a new electron beam writing material is being

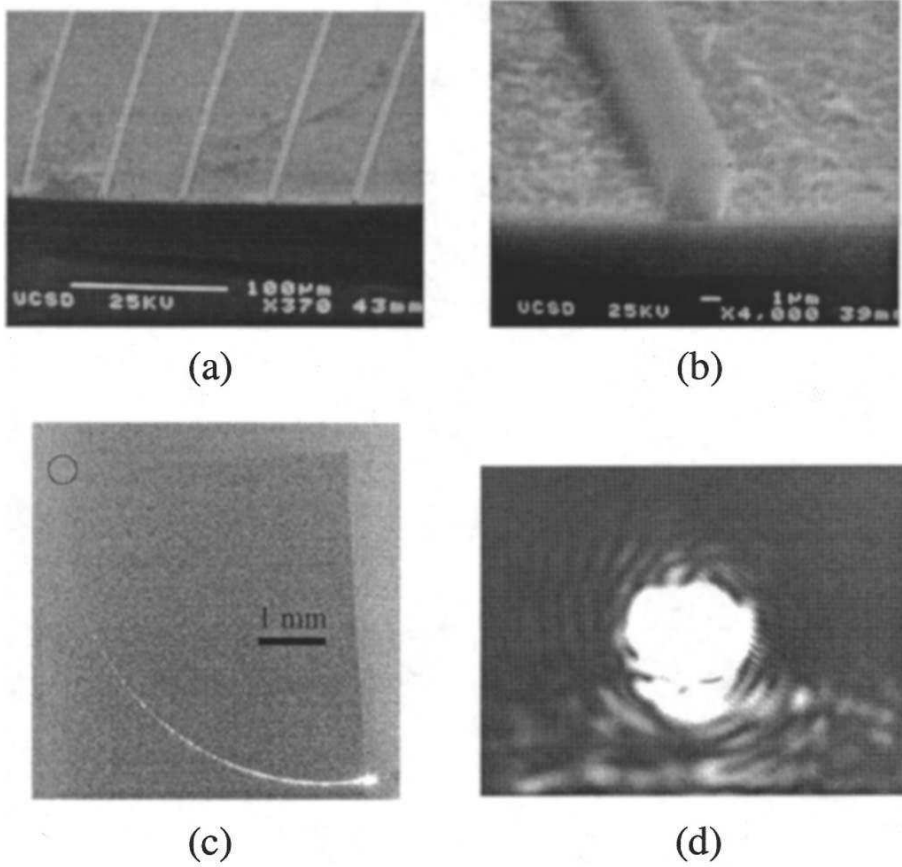


Figure IV.5: (a) SEM photograph of a PMMA-NC composite waveguide array on a  $\text{SiO}_2/\text{Si}$  substrate. (b) Closeup of PMMA-NC composite waveguide (c) Image of optical beam trace traveling along the waveguide. (d) Mode profile from the waveguide output.

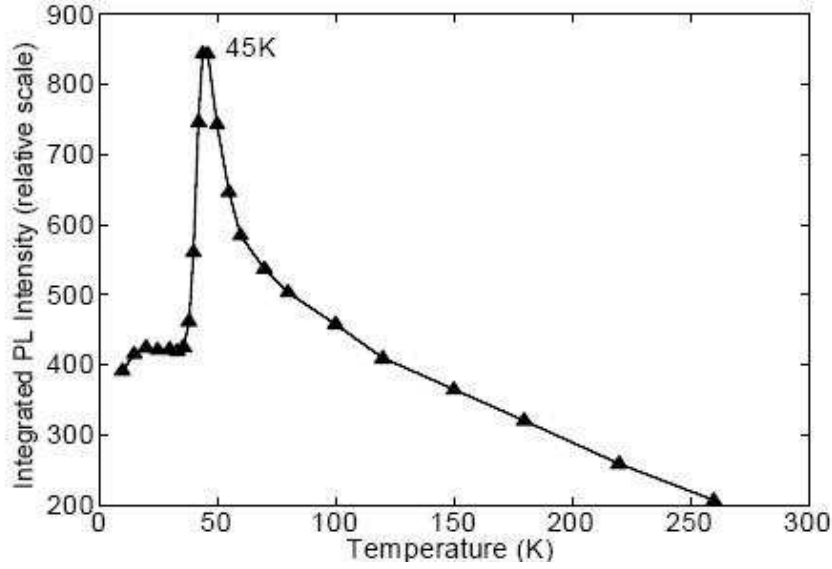


Figure IV.6: Integrated PL spectra for NCs in PMMA-NC composite vs temperature.

further investigated as a new ebeam resist as well as a new patterned optoelectronic material (see Fig IV.5).

## IV.C Low temperature measurement

Low temperature PL measurement was conducted in the Janis CCS-150 closed cycle refrigerator (CCR) systems, in which the sample was put on a small stage in the cryochamber. It can be cooled down to 10 K. We use LakeShore 331 temperature controller to adjust the temperature from 10 K to room temperature.

We measured the PL by changing the temperature slowly and steadily. We found that the total PL signal increased slowly when temperature changed from 10 K to 36 K (Fig. IV.6). But it changed with a factor of two when the temperature increased from 36 K to 45 K. At 45 K, it reached the maximum. After that it decreased and reduced as one forth at room temperature. The full

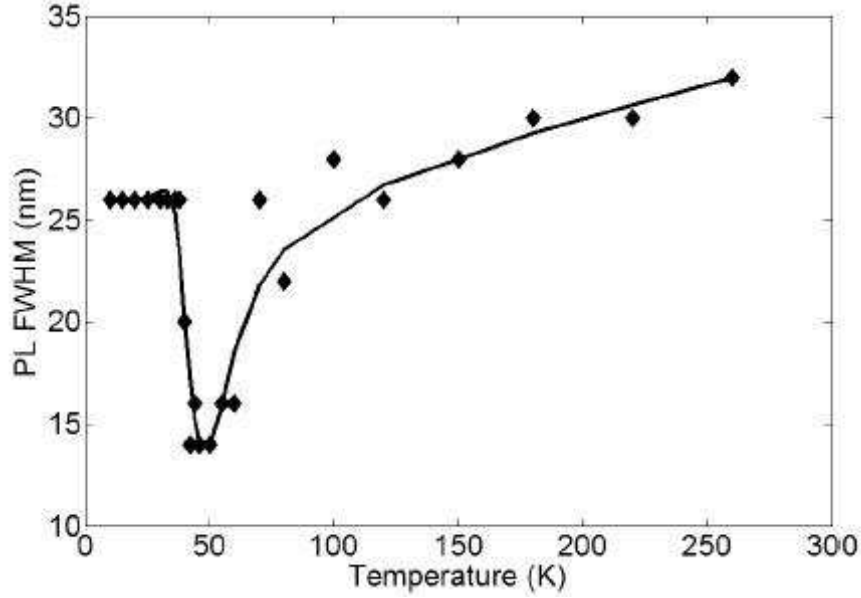


Figure IV.7: Full width half maximum of PL spectra for NCs in PMMA-NC composite vs temperature.

width half maximum of the PL (Fig. IV.7) has an inverted shape with the Fig. IV.6. It has a minimum value around 45 K which is 14 nm. At 10 K the FWHM is 26 nm and at room temperature the FWHM is 32 nm. The physical explanation for this phenomena is still unknown.

## IV.D CdSe/ZnS NCs in negative photon resist SU-8

### IV.D.1 Introduction

The resist SU-8 has been used as an UV sensitive material in microelectromechanical systems and in holographic lithography [58, 59]. It also has been demonstrated to be an appropriate material for fabrication of polymer waveguides and microring structures by using *e*-beam lithography [60], although its resolution

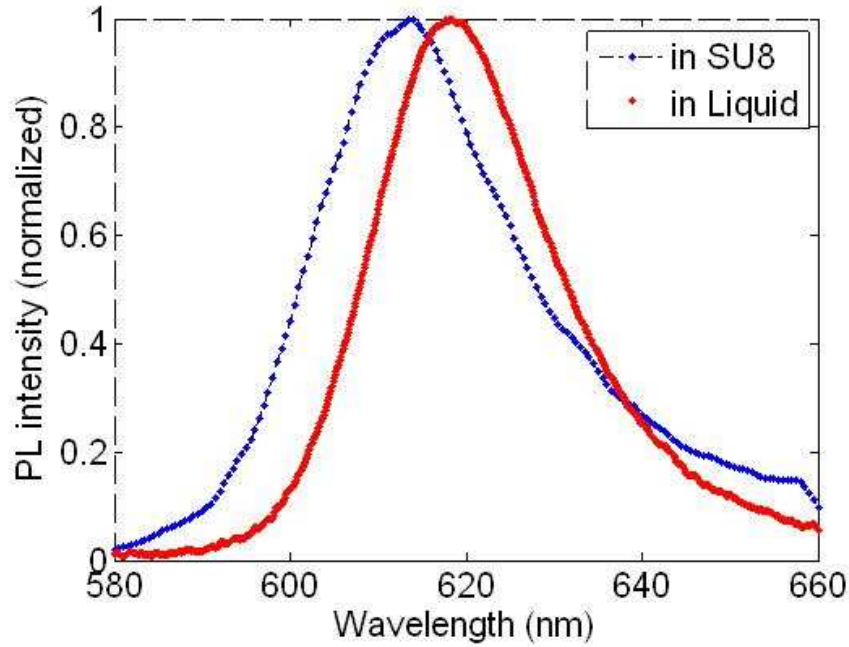


Figure IV.8: The PL for SU-8-NCs compared with the PL for NCs in liquid

is inferior to PMMA. If a SU-8 NC composite can be achieved, the sensitivity of the SU-8 material to electron beam and UV light will make it very easy to produce high-quality (less rough) NC composite single-mode-waveguide structures to investigate the NC properties in waveguide structures.

Because of the incompatibility of SU-8 with toluene, which is the solvent of the NC colloid, the NCs first must be transferred into a SU-8 compatible solvent, such as hexane or propylene ether acetate, etc., then added into the SU-8 solution very slowly with strong stirring. Precautions must be taken to prevent clustering of the NCs. Compared with the aforementioned PMMA-NC composite, the NC concentration in the SU-8-NC composite cannot be increased arbitrarily high due to the lesser dispensability of NCs in the viscous SU-8-polymer solution.

SU-8-NC composite was prepared by spin coating the solution onto a substrate followed by a soft bake in a  $90^{\circ}\text{C}$  oven for 5 min. The PL in the SU-8-NC composites was measured as shown in Fig. IV.8 with the same setup as PMMA-NCs. The NCs used to make the SU-8 composite are from a different batch bought



from the same company. Their central emission wavelength was slightly different from the one used in making the PMMA-NC composite. However, the trend of the PL after the solidification is the same. The PL blueshifts from 618 nm in liquid SU-8 solution to 613.5 nm in SU-8 solid film. Similarly, the FWHM increases from 24 nm in solution to 27 nm after being dried.

#### IV.D.2 SU-8-NC composite waveguides

SU-8 is a chemically amplified negative UV and electron beam resist. The acid generated during the exposure catalyzes the crosslinking at postexposure bake (PEB) [58], which means that less exposure dosages are needed compared to other resists. Fig. IV.9(a) shows a SEM image of an *e*-beam exposed SU-8 composite waveguide with a height of  $3.5\ \mu\text{m}$  and a width of  $2.5\ \mu\text{m}$  in the upper portion. Although a smooth sidewall was achieved, the waveguide does not have a rectangular profile. The bottom portion of the waveguide extended to  $6\ \mu\text{m}$  due to the scattering of the electrons from the surface of the  $\text{SiO}_2$  underlayer. The conductivity could be improved by employing a conductive layer on the top and even on the bottom of the SU-8 layer. In order to show the whole waveguide structure, we used a microscope to take photographs as shown in Fig. IV.9(b) and Fig. IV.9(c). Fig. IV.9(b) shows a microscopic photograph of a waveguiding coupler with the ring diameter of about  $200\ \mu\text{m}$ . Fig. IV.9(c) is a waveguidedisk coupler with the disk diameter of about  $100\ \mu\text{m}$ . Fig. IV.9(d) is a guided mode profile by imaging the waveguide output onto a near-infrared CCD camera (Merlin, Indigo) through a 20X microscopic objective lens and a imaging lens while coupling a  $1.55\ \mu\text{m}$  laser beam from a fiber to a L-shape SU-8 waveguide. The single mode profile, as shown in Fig. IV.9(d), matches the design of the waveguide structure.

As we know, SU-8 resist is very sensitive to electron beams, usually  $0.8\ \mu\text{C}/\text{cm}^2$  is typical for a SU-8 waveguide writing followed by PEB on a hotplate at  $95^\circ\text{C}$  for 1 min. However, for the SU-8-NC composite, the exposure needs to be increased to over  $2\ \mu\text{C}/\text{cm}^2$  for the same PEB processing as a result of the

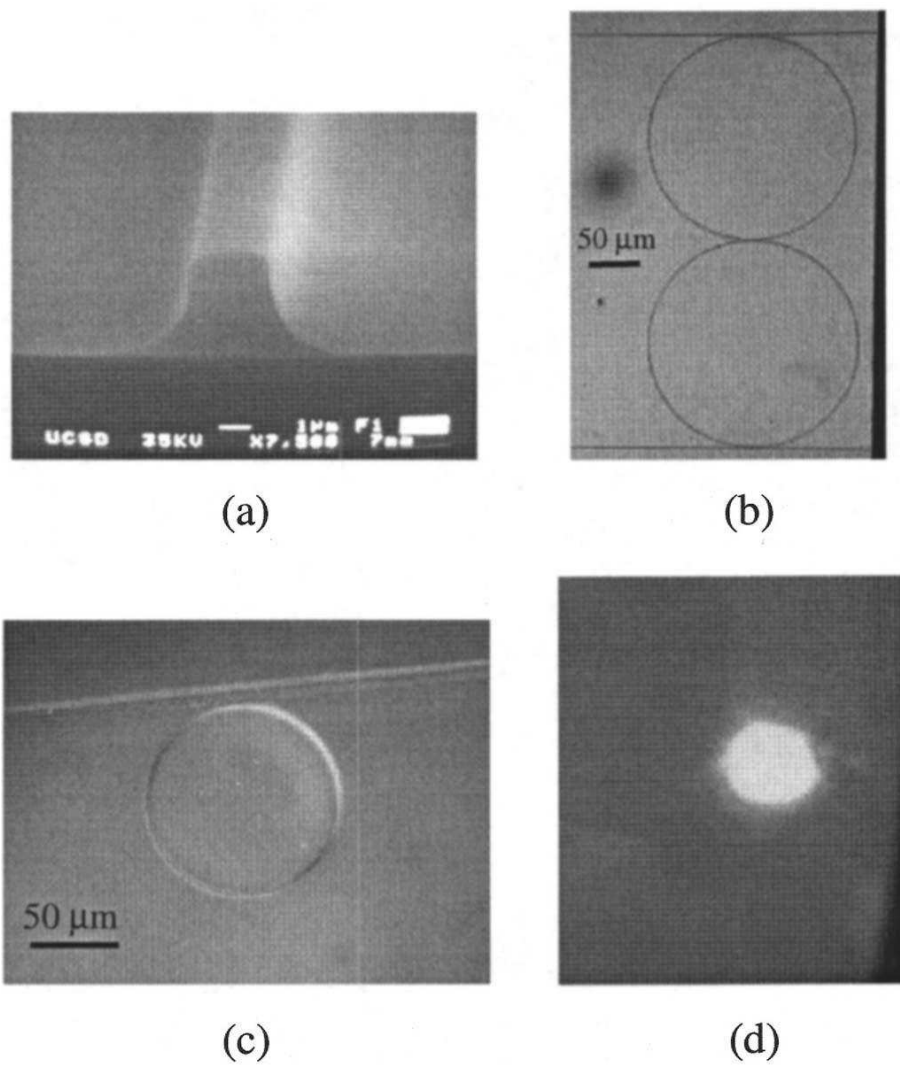


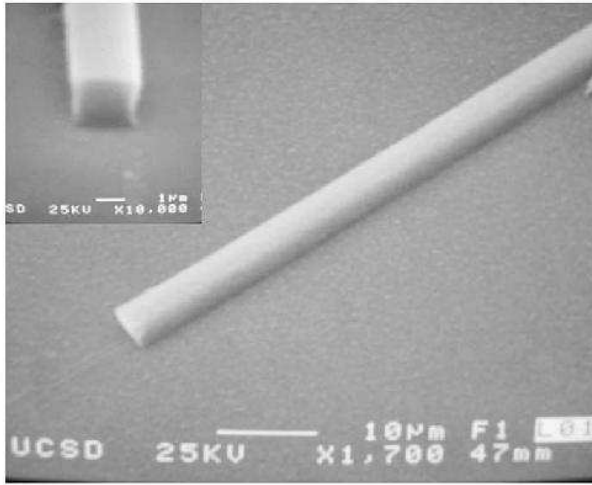
Figure IV.9: SU-8 composite structures by using e-beam lithography.

influence of the NCs component in the SU-8 matrix.

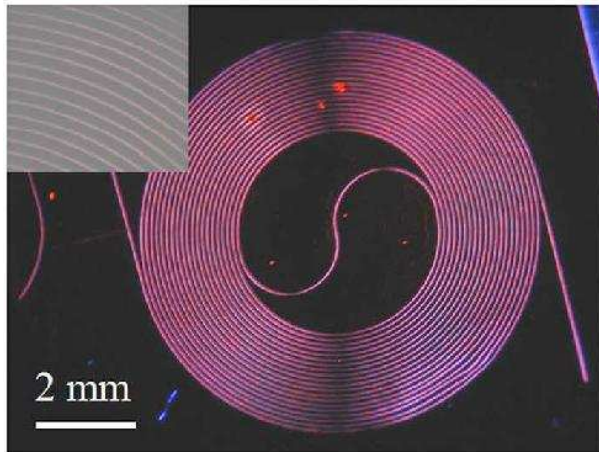
Due to the limitation of the positioning stage in our SEM writing system, the maximal writing area is about  $3 \times 3 \text{ mm}^2$ . For the larger area waveguide structures, optical lithography is a good alternative, and dry etching is unnecessary. After exposure through a mask, the SU-8-NC composite layer on the  $\text{SiO}_2/\text{Si}$  substrate was baked on a hotplate for the PEB step, developed in propylene glycol methyl ether acetate. Fig. IV.10(a) shows the SEM photograph of the fabricated waveguide with smooth sidewalls with width of  $2.1 \mu\text{m}$  and height of  $1.7 \mu\text{m}$  shown in the inset. Fig. IV.10(b) shows a spiral waveguide with a total length of 1 m and 4 mm internal diameter, and 8 mm external diameter, respectively. The interval between the waveguides is  $50 \mu\text{m}$ . We observed the whole spiral waveguide structure using a 0.7 X microscope, in which we had enough space to introduce a UV light (364 nm from Ar+ laser) to illuminate the sample area to stimulate the quantum dots. We can clearly see the photoluminescence from the emission of the CdSe/ZnS quantum dots in the SU-8 composite waveguide. The two dark areas on the spiral waveguide were due to the shade of the UV illumination. The large bright spots in the spiral areas are the NC clusters in the composite, which can be removed by filtering the SU-8-NC solution before spin coating. The inset in Fig. IV.10(b) shows the uniform photoluminescence of the waveguides.

## IV.E Infrared NCs in PMMA

Infrared PbSe NCs was incorporated in PMMA too. PL and absorption were measured as shown in Fig. IV.11 and Fig. IV.12. The peak wavelength of the PL shifts 134 nm from 1200 nm for the NCs in liquid to 1334 nm for those in PMMA. The FWHM wavelength in both cases are about the same. In Fig. IV.12, absorption curves for PbSe PMMA-NCs in different post-processing temperature are shown. The absorption of pure PMMA is plotted as a reference.



(a)



(b)

Figure IV.10: SU-8 composite structures by using KalSUSS mask aligner: (a) SEM photographs of a straight waveguide and (b) microscopic images of a spiral waveguide excited with a UV laser (364 nm).

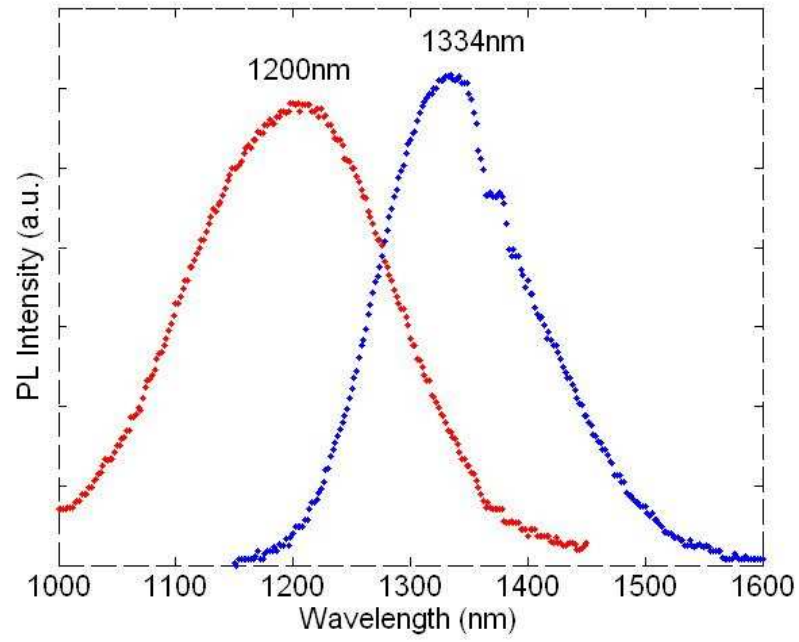


Figure IV.11: The PL of Infrared PbSe NCs in PMMA. The peak wavelength shifts 134 nm from 1200 nm in liquid to 1334 nm in PMMA. The FWHM wavelength in both cases are about the same.

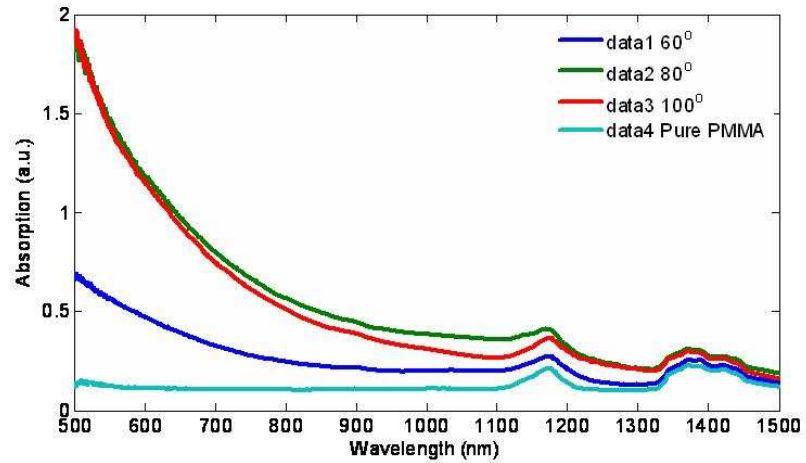


Figure IV.12: Infrared NCs PbSe in PMMA absorption

## IV.F Discussions and conclusions

Generally, NC polymer film could be obtained by incorporating NCs into solvent and polymer [61], however, non-uniform dispersion and the insolubility of NCs in large mass molecule polymer would seriously affect its quality and limit its use for application. Due to the compatibility of the MMA and the solvent of the NCs, i.e., toluene, there is no limit to raise the concentration of our PMMA-NC composite. The limit comes from the availability of the NCs concentration in toluene. Devices made of NC composite, such as waveguides, can be fabricated by use of optical lithography, followed by etching process [61]. However, directly patterning the PMMA-NC composite with electron beam lithography allows for precise control of the position of the NCs, and the shape of the NC nanostructure in device fabrication such as photonic crystals, ring resonators, and other waveguide devices [53, 62, 63]. In conclusion, we have presented a novel approach to fabricate PMMA-NC composite using pre-polymerization of MMA and commercially available colloidal semiconductor NCs. The NCs were stabilized in the rapidly formed oligomer matrices, and the complete polymerization of PMMA-NC composite was performed by common post-processing. The absorption and the PL properties of the PMMA-NC composite were measured and compared with the NCs in solution. The blue shift of the emission peak in PMMA-NC composite as well as the blue shift of the first absorption compared to that of NCs in solution is attributed to the NC environment changes. Investigation of patterning PMMA-NC composite in the electron beam lithography demonstrates promising application of our PMMA-NC composite for patterning optoelectronic devices.

The text of chapter IV, in part, is a reprint of the material as it appears in Yaoming Shen, Lin Pang, Kevin Tetz, Yeshaiahu Fainman “Characterization of PMMA quantum dot composite fabricated by pre-polymerizing method” SPIE (2004), where the dissertation author was the first author. Also in part, is a reprint of the material as it appears in L. Pang, Y. Shen, K. Tetz, and Y. Fainman,

“PMMA quantum dots composites fabricated via use of pre-polymerization,” *Opt. Expr.*, 13, 44-49 (2005), where the dissertation author was the second author. The co-authors in this publication directed, supervised, and co-worked on the research which forms the basis of this chapter.

# V

## Photoluminescence spectral study of single CdSe nanocrystals in PMMA

### V.A Introduction to the history of single NC study

#### V.A.1 Definition of blinking (fluorescence intermittency) of NCs

Blinking or fluorescence intermittency is a random switching between an emitting and a non-emitting state under steady laser illumination. This is a single molecule/particle effect which is not observable in ensemble measurements. Therefore, blinking can be used as a confirmatory test to make sure that the probe under investigation is in fact a single molecule/particle. It is found that blinking is common to all single chromophores such as single dye molecules [64], fluorescent proteins [65], single polymer segments [66], single nanocrystals like CdSe [67], single quantum dots of different materials like InP [68] and Si [69].



## Blinking for nanocrystals

Bawendi Group in MIT is the first research group who report such phenomena by continuously monitor the spectrum of single CdSe/ZnS NCs in 1996. They reported that images of individual NCs taken with an integration time of 0.5 sec and at 10 K appeared to flicker on and off. They didn't show a gradual dimming but rather an "all on/all off" behavior. Some of them can stay "dark" for as long as 10 min before resuming emission [67].

## Blinking for self assembled QDs

Mitsuru Sugisaki etc. [70] measured individual self-assembled InP QDs by far field imaging and single dot spectroscopy. They were using a metal-organic vapor phase deposition system to grown self-assembled InP QDs sandwiched between two GaInP barriers on a Si doped GaAs substrate. They also observed that some QDs exhibited the blinking phenomenon, i.e., the PL intensity switches randomly between a high efficiency state (referred to as "on") and a very weak state ("off"), while the PL from other QDs is stable.

## Blinking for other material

On/off blinking and switching behavior has also been found in single molecules of green fluorescent protein [65]. Single molecules immobilized in polyacrylamide gels were observed producing several seconds of fluorescence, then several seconds without emission, followed by resumption of emission, repeating over the course of many minutes during several minutes of illumination. The on-time histograms were fitted by single exponentials. The dark-time histograms, however, showed bi-exponential decays with a short decay time of 1 s and a long decay time greater than several tens of seconds (limited by their 90 s data collection time).

### V.A.2 Telegraph noise

The emission intensity as a function of time, so called time trace resembles a random telegraph signal (RTS). Such a random telegraph like PL signals were first observed in the spectrum of single Ba<sup>+</sup> ion contained in a radio frequency trap [71]. The ion is emitting photons (on-state) until it is shelved into a long lived state for about 30 s. Here the ion is out of resonance with the excitation laser frequency. Therefore, it could neither absorb nor emit photons (off-state). Relaxation back to the ground state restores the on-period.

### V.A.3 Auger process

A nanocrystal can absorb two (or more) photons at a time (instead of one), creating two (or more) electron-hole (e-h) pairs. The energy released after recombination of one pair is transferred to a second exciton, which results in the ejection of an electron into a long-life trap in the ZnS matrix. This is called Auger process. The Auger process created a local electric field inside the nanocrystals, which can change the internal electronic states. Therefore, during the off period in which the nanocrystal is charged, the NC does not emit light even if it absorbs a photon. Electron-hole pairs would recombine nonradiatively and transfer their energy to the remaining carriers.

### V.A.4 Power law

In contrast to exponential processes like intersystem crossing related photon bunching in single molecules, single CdSe NC follows an inverse power law behavior over many decades in probability density and in time. Such a broad distribution of kinetics with rates varying over five orders of magnitude is common to all studied NCs thus suggesting a universal process underlying the on/off fluorescence intermittency. Experiments carried out by Schuster et al. [72] reported similar power law blinking behavior for single dye molecules as well. Many kinetic

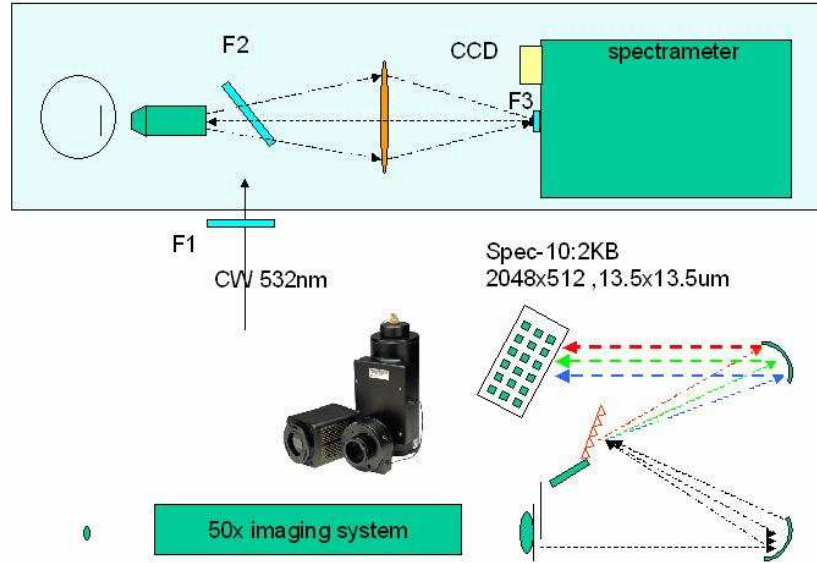


Figure V.1: The micro PL experiment setup for single CdSe nanocrystals in PMMA measurement.

models have been proposed to explain such a large dynamic range.

## V.B Experiment purpose and set up

To understand the behavior of the NCs in PMMA, it is important to measure a single NC to avoid the average effect from the inhomogeneous broadening of many NCs. We set up a micro-PL system to achieve this.

The sample was prepared by using the colloidal CdSe/ZnS core shell NCs (from Evident Technologies). Single domain wurtzite NCs with average 5 nm in diameter capped by a few-monolayer ZnS shell. The addition of a ZnS shell has been shown to have a significant effect on the luminescence and can increase the quantum yield to as high as 50 percent at room temperature. A PMMA layer about 200 nm thick was spin coated on a quartz substrate followed by a spin coat of extremely dilute solution of NCs in toluene, leading to CdSe/ZnS NCs

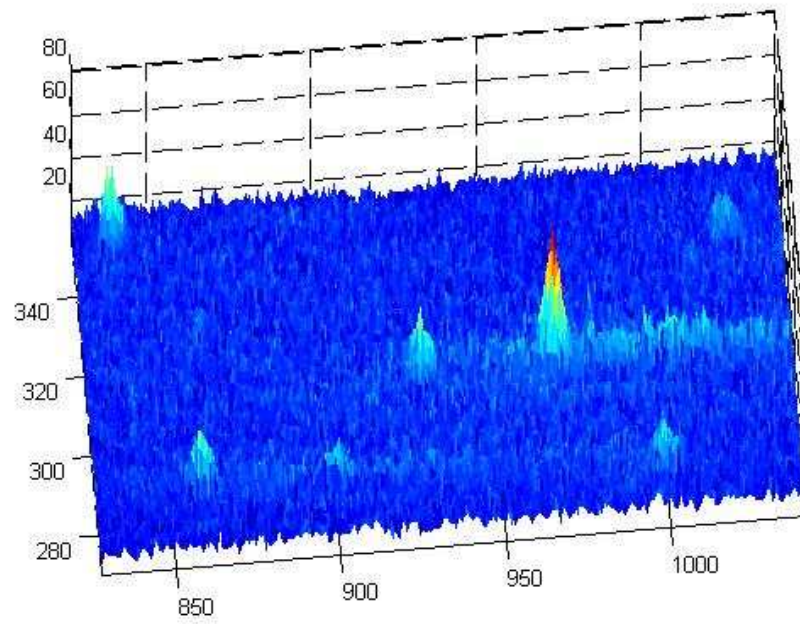


Figure V.2: This is a typical image detected by the liquid Nitrogen cooled CCD camera. Horizontal and vertical axes are the horizontal and the vertical pixels of the CCD correspondingly. Z axis is the intensity value read by the CCD, which is shown in color as well.

distributed in a PMMA matrix. The final concentration was chosen to produce an area density of less than one dot per  $\mu\text{m}^2$  in order to allow individual NCs to be spatially resolved using standard far-field optics.

For PL measurements, the sample was placed into a continuous flow cryostat, and the temperature was kept constant at 7 K by controlling the flow of liquid Helium. A diode pumped solid state laser operating at 532 nm was used for excitation, with power densities typically between 1-20 kW/cm<sup>2</sup>, and was varied using neutral density filters. The luminescence from the sample was collected through an optical microscope objective (50x, numerical aperture 0.55) with a long working distance. The collected light was passed through a notch filter, dispersed in a monochromator, and was detected using a liquid-nitrogen-cooled charge-coupled device (CCD) camera. The spectral resolution of the setup was about 200  $\mu\text{eV}$ . Spectra from a single NC were monitored continuously with an integration time that we varied between 500 ms and 30 s depending on the excitation power density and NC brightness.

Fig. V.2 is a typical image detected by the liquid Nitrogen cooled CCD camera. Horizontal and vertical axes are the horizontal and the vertical pixels of the CCD correspondingly. Z axis is the intensity value read by the CCD. It is shown in color as well. Horizontal pixels represent the wavelength or energy of the spectrum, vertical pixels represent the real position. There are at least four NCs in different vertical positions in the graph. So we can say there are at least four NCs in the image.

## V.C Experiment results

### V.C.1 Spectral diffusion

Spectral diffusion, especially random switching between discrete levels, has been observed and studied in strain-induced GaAs QD's [5]. It has also been found when colloidal nanocrystals were deposited on gold substrates [73]. In this

section, we will show that colloidal CdSe nanocrystals in PMMA also exhibit similar behavior, and we quantify the dependence on excitation power. Also, we observe a jitter of the emission energies of the NCs. Each NC has a characteristic jitter that allows us to identify phonon replicas for single NCs.

The density of NCs was made so dilute that we typically observed only a single NC in the interrogated spatial and spectral range.

Spectral diffusion, random energy shifts, is a common phenomena we have observed in our single NC detection experiment. In Fig.V.3, we analyze a series of 1500 spectra taken in intervals of 0.5 s. The spectrum peak is seen to wander randomly between 2.099 eV and 2.108 eV. These could be caused by quantum-confined Stark effect induced by the local field change.

The quantum-confined Stark effect in single Cadmium Selenide (CdSe) nanocrystallite quantum dots was studied by S. A. Empedocles and M. G. Bawendi [74]. The electric field dependence of the single-dot spectrum is characterized by a highly polarizable excited state (  $10^5$  cubic angstroms, compared to typical molecular values of order 10 to 100 cubic angstroms). Additional ionization or recombination events, as well as relocalization of external charges, could result in changes in both the zero-field energy and the excited-state dipole of a single NC. The magnitude of spectral diffusion shifts implies variations in the local field on the order of  $10^5$  to  $10^6 V/cm$  (unscreened) and is consistent with the addition or removal of an electron from the surface of the NC.

The observed local electric fields may be the result of charge carriers on or near the surface of the NC. Photoionization has been proposed as the source of fluorescence intermittency in single CdSe NCs at room temperature [28]. Photoionization leaves a charged NC core that may not relax radiatively upon further excitation. Emission resumes when the core is neutralized by the return of the ejected charge. At 10 K, however, there is little thermal energy to promote the return of an external charge. Instead, neutralization may occur through an additional ionization event, resulting in an emitting NC in the presence of a potentially

large and randomly oriented local electric field.

### **V.C.2 Influence of spectral diffusion on the line shapes of single CdSe NCs**

The presence of randomly oriented local electric fields in ensemble samples represents an additional form of inhomogeneous broadening that will not be eliminated by improvements in sample size and shape distribution. Instead, modifications of the ionization barrier, changes in the surrounding matrix, or both, may be required.

In ensemble NCs, inhomogeneities in size and shape within ensemble samples result in spectral broadening that is many orders of magnitude larger than single NC spectra. Theory predicts that NCs should have atomic-like spectral transition due to long excited-state lifetimes and weak coupling to acoustic phonons, experiments have suggested that line widths in both excitation and emission are quite broad (for example, “homogeneous” line widths extracted from fluorescence line narrowing experiments in CdSe NCs are reported to be  $\sim 5\text{meV}$  [75]). Also a range of single NC line widths over 2 orders of magnitude have been reported for II-VI nanocrystallite NCs. It has therefore been difficult to use single NC line shapes to learn about the intrinsic physics of these NC systems. Why single NC spectroscopy couldn’t uncover the true “homogeneous” line width? It is might due to the spectral diffusion is on a time scale that is fast compared to the acquisition time of the experiment. Through the direct observation of spectral shifting on a 0.1 s time scale, the contribution of spectral diffusion to the line shape of single CdSe nanocrystals is demonstrated [76].

### **V.C.3 Spectral jumps between two states**

Besides the normally observed random spectral shifts, we have found large abrupt spectral jumps between two states. We investigated several NCs switching

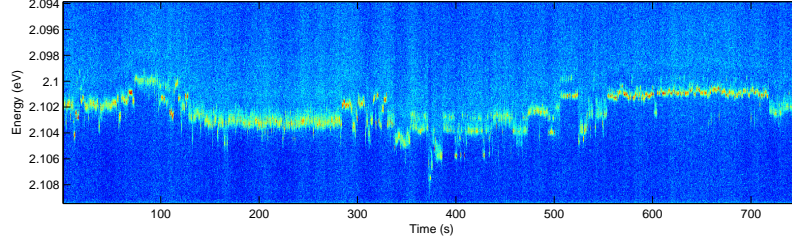


Figure V.3: Spectra from another NC were recorded continuously with an integration time of 0.5 s. The emission peak randomly shifts with small energy changes between 2.099 eV and 2.108 eV.

between two states. Spectra from a typical switching NC, recorded at six different excitation powers, are shown in Fig. V.4 (a)-(f). These spectra were recorded continuously with an integration time of 2 s each. Fig. V.4 (g) shows the typical spectrum of each of the two states. The red line (bold line) is for the lower energy state, which we will call state 2, while the blue line (thin line) is for the higher energy state which we call state 1. The energy difference between the two states is 5.6 meV. Fig. V.4 (h) contains plots of intensity vs. time for the data taken from Fig. V.4 (a)-(f). Again, the red line (bold line) is state 2 and the blue line (thin line) is state 1. Fig. V.4 (i) is the plot of the characteristic switching frequency (the inverse of the average interval time between switching) vs the excitation power. From Fig. V.4 (g) and (h) we see that there is no sizable change in the integrated PL intensity for the two states. The excitation power density is of the order of  $10 \text{ kW/cm}^2$ , which is similar to that used for measurements with InP QDs [6].

Fig. V.4 (i) shows that the switching frequency increases with increasing excitation power density. Since the widths of both state plateaus decrease with increasing excitation power, we can conclude that the transitions between the two states are light-induced.

The two emission peaks in Fig. V.4 (g) seldom emit together within our integration time, which excludes the possibility of biexciton emission and phonon replicas. If a biexciton was created, we would observe both lines within the recom-



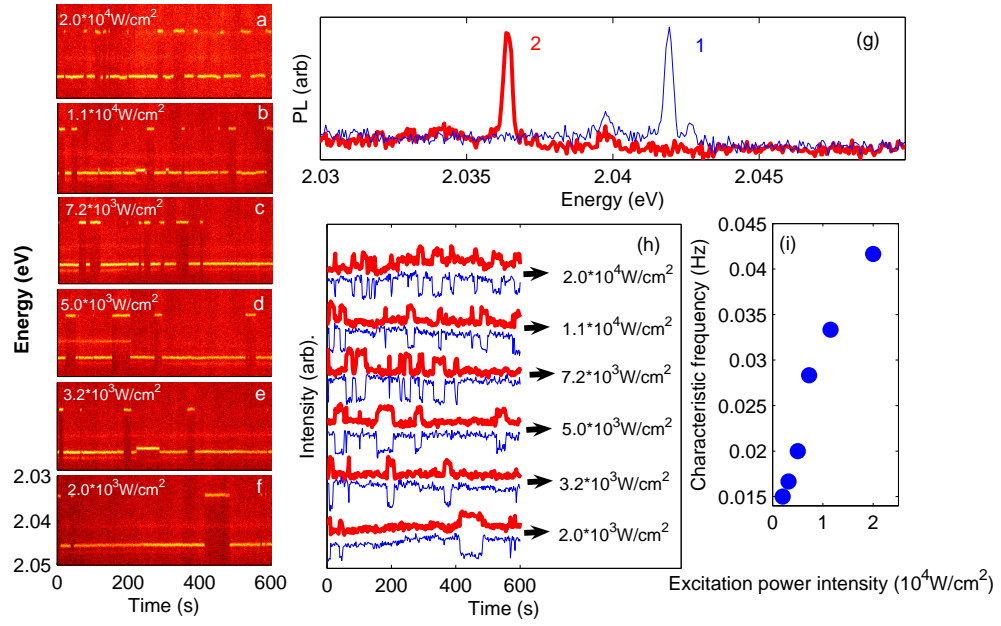


Figure V.4: Spectra from a typical switching NC, recorded at six different excitation powers ( $2.0, 3.2, 5.0, 7.2, 11, 20 \times 10^3 \text{ W/cm}^2$ ) are shown in order in (a)-(f). The integration time 2 s is used for this measurement.

bination times which are much shorter than our integration time as the biexciton relaxes to the exciton radiatively, followed by exciton emission. The same observation applies to phonon replicas. In 2002, Shimizu et al. found a spectral shift between two positions when they put CdSe/ZnS NCs on a rough metal surface [73]. The emission energy fluctuates within 15-25 meV. The authors suggested that the observed emission shifts were caused by neutral (X) and charged ( $X^-$ ) exciton emissions from a single NC. Theoretical calculation indicated that the charged NC could emit 25 meV lower in energy than the neutral exciton [77]. These values are different from our result, since the energy spacing in our experiments between two positions is 5.6 meV or smaller. Similar spectral switching behavior has also been observed in InP quantum dots in a  $Ga_xIn_{1-x}P$  matrix grown by metal-organic vapor-phase epitaxy [6]. The authors found that the quantum dot spectrum switched between two states which had the same integrated PL, similar to our result. The difference is that each state has multiple lines in the experiment.

#### V.C.4 Tunneling Model

Bawendi and co-workers proposed a model to explain the CdSe NC fluorescence intermittency [8, 7]. A charged NC was taken to be a dark NC. The transition back to a bright NC occurred through recapture of the initially localized electron (or hole) in the NC core or through capture of another electron (or hole) from nearby traps. We adopt this model to explain the spectral switching and assume that there are two metastable states of the NC which are connected with the charging and discharging of a metastable trap in the host matrix close to the NC. The Stark shifts caused by the charge could explain the two spectra we observed.

Tunneling of electrons between a NC and trap states can be rationalized as the observed redshift of the absorption bandedge with the addition of a capping semiconductor shell onto the core of the NC [78]. This shift has been attributed to the extension of the delocalized electron wavefunction into the shell. The small

effective mass of the electron and an enlarged barrier for the hole escape (because quantum confinement for electronic states are stronger than that for hole states) support a tunneling of the electron rather than the hole. Electrostatic force microscopic (EFM) measurements carried out on single CdSe NCs [28] proved that nanoparticles become positively charged under continuous laser excitation. According to Bardeen [79], the tunneling rate between NC and trap states depending on the overlap matrix element of the carrier and trap wavefunctions and the density of states of NC and trap.

### V.C.5 Fluorescence quenching

The potential application of single NCs as luminescent labels (e.g., in biological systems) is based on the high stability in combination with a relative narrow emission band, a broad excitation band, and a large “Stokes shift” [80, 81]. The total number of photons emitted by a single NC until bleaching occurs is an important number. For single dye molecules, the highest number of photons emitted before bleaching is around  $10^6$ . On the basis of an overall efficiency of about 5 percent for our system (i.e., one out of every twenty emitted photons is counted), the number of photons emitted by a single NC before bleaching occurs is typically  $10^7 - 10^9$ .

We observed three types of quenching effect in our experiment:

- a) there is almost no sign before quenching happens except the PL peak jumps between two states (Fig. V.5);
- b) before quenching happens, the PL peak jumps to a lower energy state (Fig. V.6);
- c) before quenching happens, the PL peak jumps to a higher energy state (Fig. V.7).

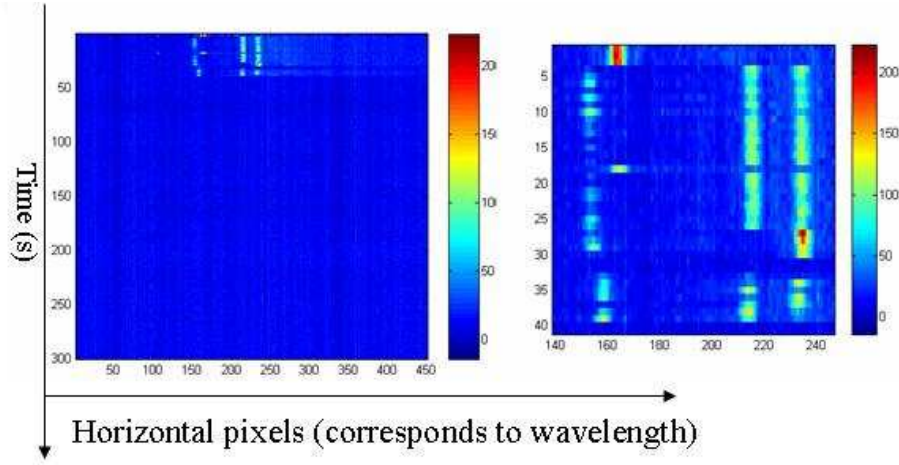


Figure V.5: NC has been quenched after a few minutes. But there is almost no sign before quenching happens except the PL peak jumps between two states. The right figure is a magnified part of the left figure.

### Explanations for the NC quenching phenomena

It is found that the spectral diffusion for NCs without PMMA matrix at room temperature is not random, but rather, a blue shift of about 10-15 nm [82]. This blue shift was attributed irreversible photooxidation of the quantum dot. Even under ambient conditions (without intense excitation), surface oxidation of CdSe nanoparticles has been reported [83].

This photooxidation also brings higher initial light output because oxygen quenches the NC defect luminescence. It is well-known that in addition to the fast (nanosecond) exciton emission, also relatively longlived (microsecond) defect emission can occur in NCs [84]. Because of the long lifetime, the fast photon absorption and emission process is interrupted, until the long-lived excited state has returned (via radiative or nonradiative relaxation) to the ground state. If oxygen can quench the defect luminescence, a higher exciton emission yield is expected by reduction of the time spent in the “dark state”. For CdS and ZnS, it has been established that oxygen can quench the defect related emission [84].

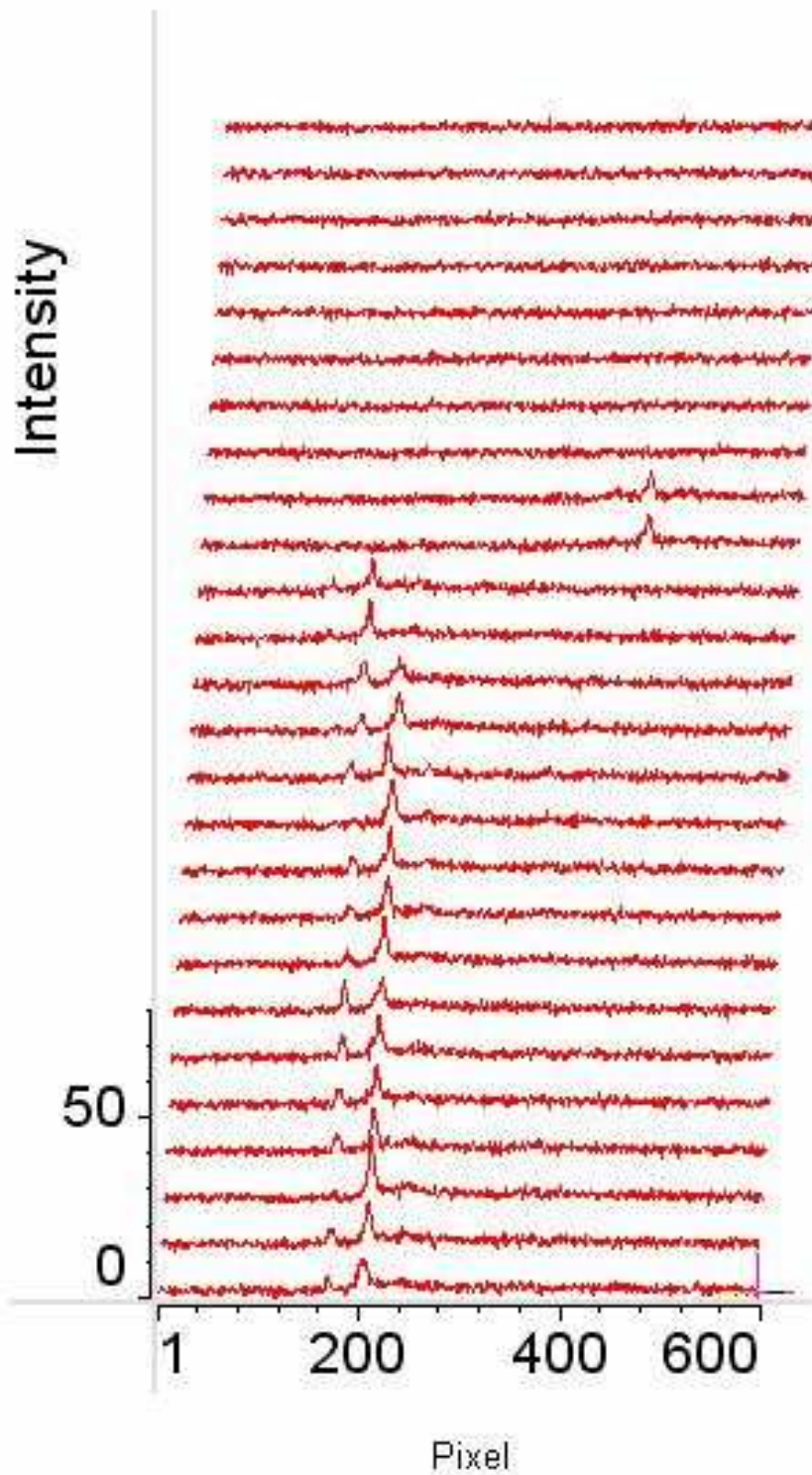


Figure V.6: Before quenching happens, the PL peak jumps to a lower energy state.

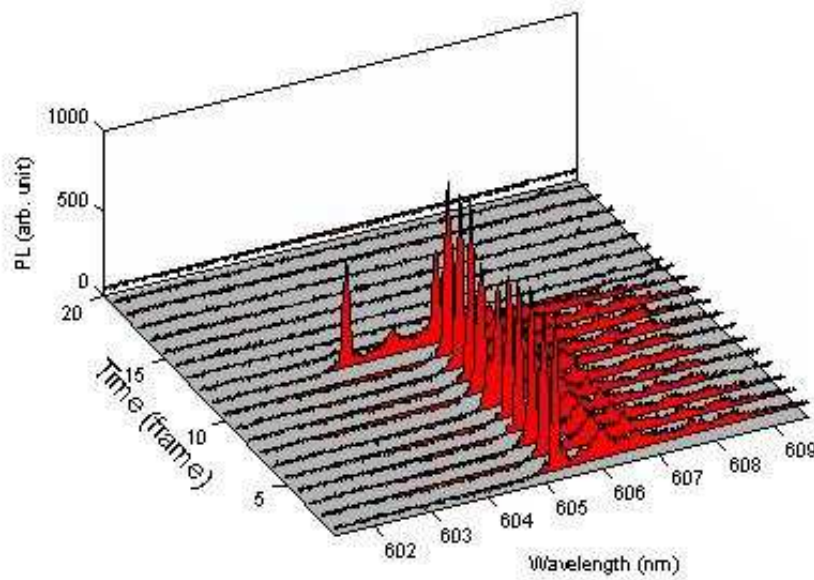


Figure V.7: Before quenching happens, the PL peak jumps to a higher energy state

If the same occurs for CdSe NCs, this can explain the higher initial light output observed for CdSe NCs in air.

The main oxidation product was suggested to be  $SeO_2$ . For photooxidation to take place, oxygen has to diffuse through the passivating ZnS layer that has been grown on the CdSe nanocrystals. The observation that photooxidation occurs indicated that the ZnS layer is not a closed epitaxial layer but rather a layer with grain boundaries, presumably at places where ZnS islands, which started to grow at different locations on the CdSe nanocrystal, meet. At these boundaries, oxygen can diffuse to the CdSe core inside the ZnS shell. For the thicker shell the oxidation rate is reduced because of the slower diffusion of oxygen to the CdSe core through a thicker ZnS shell. Wilfried [55] investigate the time evolution of the room-temperature emission spectra of single CdSe/ZnS quantum dots over time periods up to 30 min with a time resolution down to 6 ms. They studied two NCs with different ZnS cap thickness: 4 monolayers and 7 monolayers. They found that the two spectra recorded at the later times are clearly blue shifted with respect to

the initial wavelength.

As a result of the photooxidation at the CdSe surface, quenching states are expected to be formed at the  $CdSe/CdSeO_x$  interface. The formation of surface quenching states causes a decrease of the number of photons emitted. In the single NC emission spectra observed in the earlier experiment [55], a gradual decrease in light output is indeed observed as the emission shifts to shorter wavelengths. Finally, the luminescence disappears and the dot has bleached. The occurrence of photooxidation for NCs can explain the shorter bleaching times observed for NCs in air.

Also, in a nitrogen atmosphere, photobleaching occurs, albeit after much longer times. It was reported that when NCs were put in nitrogen atmosphere, there is only random spectral diffusion in time and no shift to shorter wavelengths is observed [55]. Photobleaching occurs about 4 times faster in air than in nitrogen, indicating the formation of nonradiative recombination centers during photooxidation. The observation provide convincing evidence that the observed blue shift of the emission in air is due to photooxidation of CdSe.

In our case, NCs are protected by the PMMA matrix from the oxygen. So for most NCs in our experiment, the luminescence intensity stays constant in time – no blue shift observed. But some of them will still become dark after a period of time. There are large differences between quenching times for individual NCs.

In view of the high laser power ( $20kW/cm^2$ ), photobleaching is not unexpected. Few materials are stable against photodegradation under the presently used laser power. The nature of the photoinduced quenching states is not clear. Possibly, the NCs, which are embedded in a capacitor-like structure, act as efficient trapping centers for excitons. At a high enough electric field, however, the photoexcited electrons tunnel out of the dots fast enough to quench the emission.



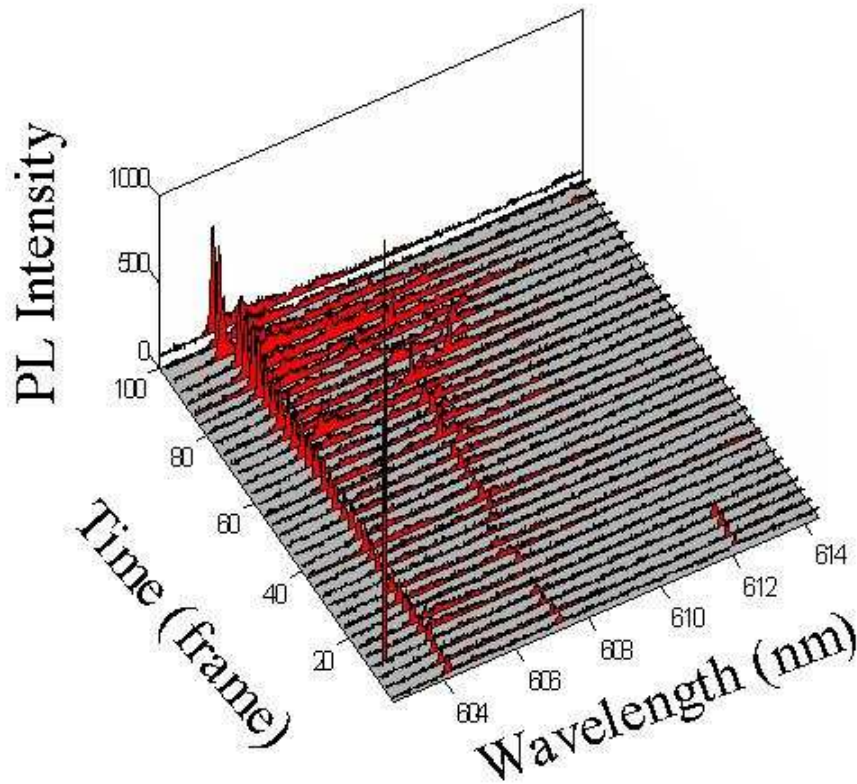


Figure V.8: The NC is pumped continuously by the CW laser. PL is observed increasing with time. The sharp peak close to 603 nm is noise.

### V.C.6 Photo-enhanced luminescence

Except the PL quenching, we also observed photo-enhanced luminescence (“photo-brightening”), shown in Fig. V.8.

An effect of photo-induced PL enhancement was noted in the glassy close-packed films of CdSe NCs covered with the ZnS film [85]; however, the process was not studied in detail. A PL intensity photo-enhancement was also observed at low temperatures in CuI and CuBr nano-crystals embedded into a glass or polymer matrix and attributed to photo-generated carrier trapping and their release when temperature increased [86].



Origin of processes leading to the photo-stimulated increase of the NCs potential barrier can be attributed to the recharging of the interface trapping states and change of the local electric field at the NC, or alternatively, to the atomic bond restructuring classified as photo-chemical processes in II-VI compounds. The NCs surface charge can reduce the exciton PL intensity. This can be a result of the exciton ionization in the external electric field as observed in the photo-conductivity study of close-packed glassy solids of colloidal CdSe NCs [87].

In the opposite case, the compensation (neutralization) of the surface charge would lead to the PL increase due to the stabilization of the exciton, increasing its binding energy, and reducing the PL thermal quenching. If only one type of photo-generated carriers is captured and the other left on the NC level, the Auger mechanism would reduce the PL intensity as was observed experimentally in Ref. [85]. Therefore, both the electron and hole after being released from the NC states must be captured by spatially separated and charged donor and acceptor defects, correspondingly. Crucially important to the present studies is the enhanced photostability of semiconductor quantum dots under continuous laser illumination. Specifically, whereas dye molecules typically undergo irreversible photochemistry (“photobleaching”) to a nonfluorescent state after absorption of  $10^6$  photons, single NCs in experiment have been observed to absorb and emit up to  $10^9$  photons without photobleaching. Correlation function Stochasticity of photophysical processes in nanocrystals and photophysical processes in nanosystems exhibit interesting dynamics quite different from those in the bulk. Besides the cage effect, occupancy statistics of excitations becomes important. Since only a few excitations are typically present per nanosystem, bulk description of the kinetics in terms of average densities is inappropriate and one has to deal with evolution of a discrete distribution of excitations. Also it is well known that the surface of nanocrystals is made of atoms that are not fully coordinated. The unsaturated dangling bonds are highly active and act like defect states unless passivated. Because of high surface-to-volume ratio, the contribution of surface states is significant in controlling the

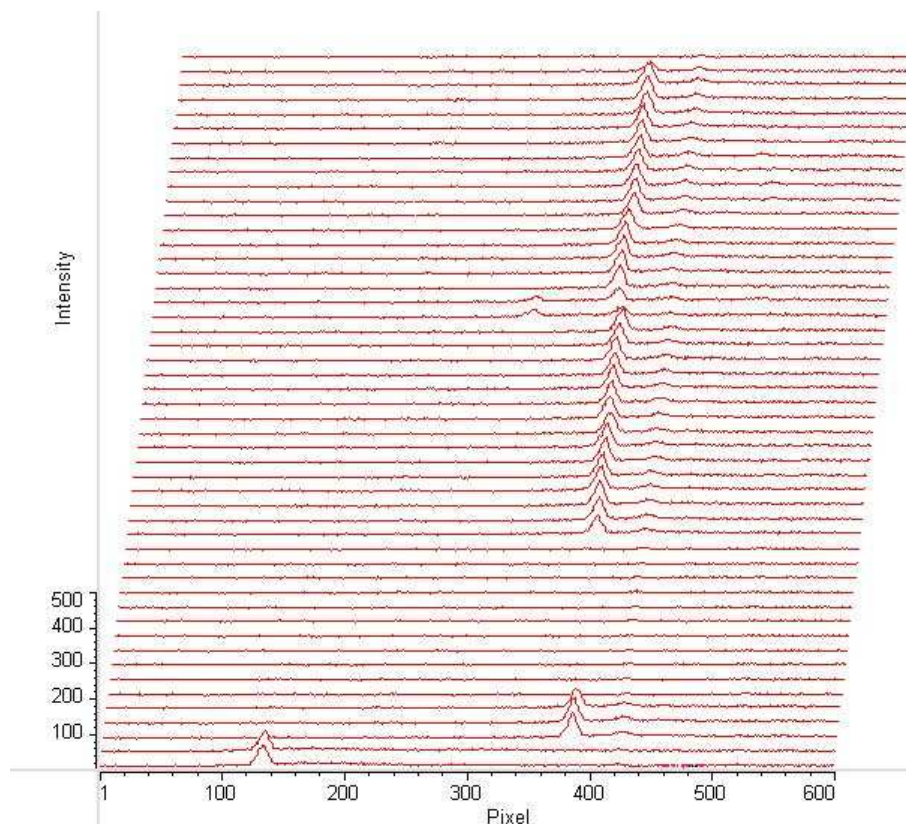


Figure V.9: Although in our measurement blinking phenomenon is not dominant, we do see some of the dots will recover after stayed dark for a few minutes. It is different with quenching since quenching bleached the NCs and they won't emit light any more.

optical properties of nanoparticles.

### V.C.7 Blinking

Although in our measurement blinking phenomenon is not dominant, we do see some of the dots will recover after stayed dark for a few minutes (Fig. V.9). It is different with quenching since quenching bleached the NCs and they won't emit light any more.

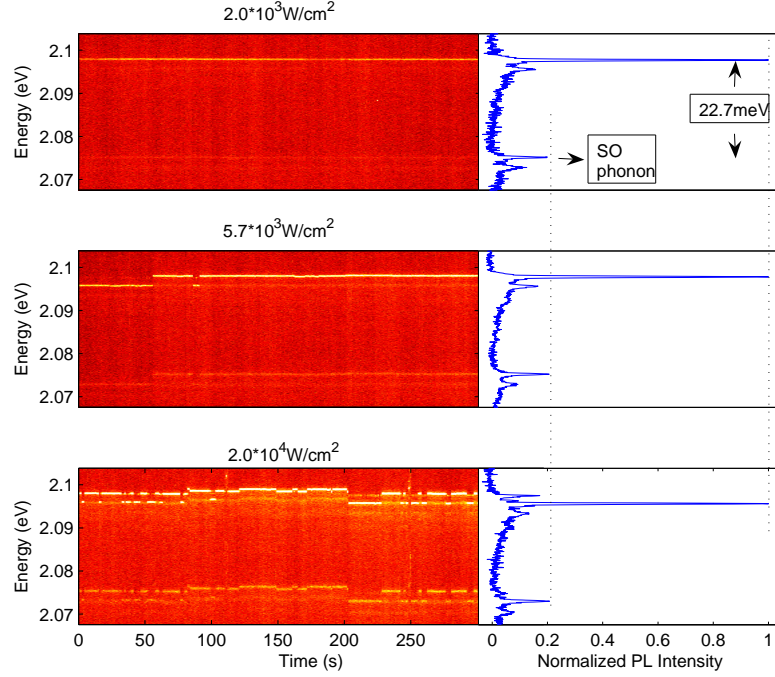


Figure V.10: Spectra from a NC were recorded continuously with an integration time of 2 s each. (a-c) shows in some NCs, higher laser intensity not only increases the switching frequency, but also makes the states moving randomly.

### V.C.8 Phonon replicas

Fig. V.10 (a-c) shows that in some NCs, higher laser intensity not only increases the switching frequency, but also makes the states move more randomly. In addition, the figure shows that there is an additional peak in lower energy side with the energy difference 22.7 meV. The energy shifts of the lines are correlated; therefore, we infer that these lines come from a single NC. The right side of Figure V.10 (a-c) shows the normalized spectrum at each laser intensity, respectively. The ratio of the side-peak intensity to the exciton-peak intensity remains constant when the pump intensity changes.

In order to observe more spectral lines, we integrated over 30 seconds for each frame in Fig. V.11. We recorded 200 measurements continuously with constant temperature and excitation power. Again the energy shifts of the lines

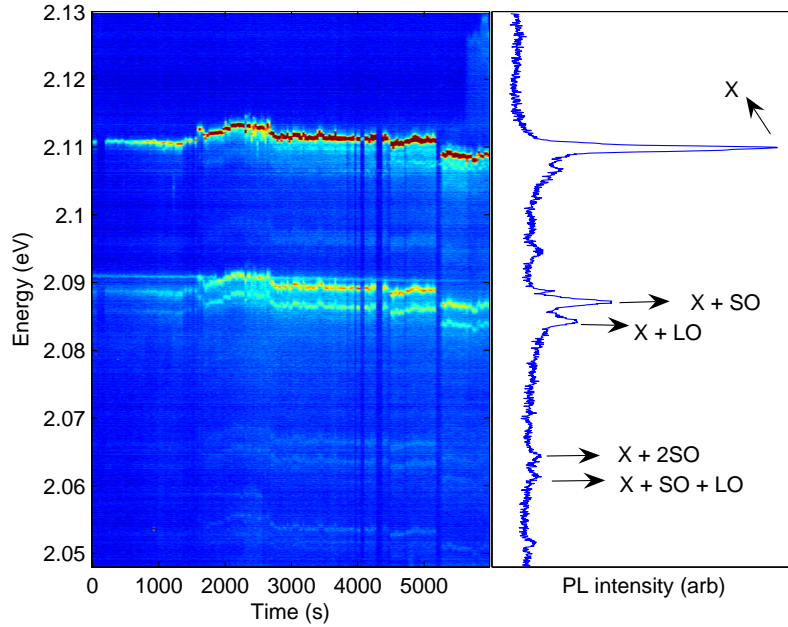


Figure V.11: Spectra from a NC were recorded continuously with an integration time of 30 s each and constant temperature and excitation power. We used a 30 s integration time for each frame to see the lower energy peaks which are weaker than the exciton peak.

are correlated; therefore, we conclude that these lines come from a single NC. The energy differences between the main line and the satellite lines are 22.7 meV and 25.8 meV, respectively. Also we can see more lines on the lower energy side. The energy differences with the main line are 45.4 meV and 48.5 meV respectively. We attributed the side peaks to phonon replicas and identified them as the lines from surface optical (SO) phonons, longitudinal optical (LO) phonons, two SO phonons, and one SO plus one LO phonons.

The energies of the SO modes,  $\Omega_{SO}$ , are determined by the energy of the TO phonons,  $\Omega_{TO}$ , in CdSe NCs, the shape of the NCs, and the dielectric constants of the core and surrounding medium. For spherical NCs the classical dispersion

relation for the interface phonons is given by the following equation [88]:

$$\Omega_{SO} = \Omega_{TO} \left[ \frac{\varepsilon_0 l + \varepsilon_M (l+1)}{\varepsilon_\infty l + \varepsilon_M (l+1)} \right]^{1/2} \quad (\text{V.1})$$

where  $\varepsilon_0$  and  $\varepsilon_\infty$  are the static and high-frequency dielectric constants of the bulk CdSe and  $\varepsilon_M$  is the static dielectric constant of the surrounding medium. Only SO-phonons with  $\ell$ =even integers are allowed (SO-phonons with  $\ell$ =odd integers are forbidden). By using the bulk CdSe values of  $\Omega_{TO} = 167.5 \text{ cm}^{-1}$ ,  $\varepsilon_0 = 9.3$ ,  $\varepsilon_\infty = 6.1$  and the dielectric constant of hexagonal ZnS  $\varepsilon_M = 8.3$ , we have calculated for the lowest ( $\ell=2$ ) and the infinite limit ( $\ell \rightarrow \infty$ ) modes of spherical CdSe NCs values of  $\Omega_{SO}^{\ell=2} = 180 \text{ cm}^{-1}$  (22.4 meV) and  $\Omega_{SO}^{\ell=\infty} = 185 \text{ cm}^{-1}$  (23.0 meV), respectively. The calculated energy is close to the experiment value (22.7 meV).

LO phonon energy 25.8 meV is smaller than the bulk value of 26.1 meV [89], and is in good agreement with the values expected from theory for a 2.5 nm radius CdSe NC, which are in the range 23.8-26.0 meV for the first four LO phonons [90].

The Huang-Rhys factors (electron-phonon coupling strength) can be roughly estimated from ratio between integrated intensities of the 2SO and SO lines. We obtained a value of  $S \approx 0.2$ .

### V.C.9 Other types

Some NCs were observed to operate outside of the two-state description. We found NCs switching among three levels or more.

## V.D Conclusions

We have investigated random switching between two states in the PL from CdSe/ZnS colloidal nanocrystals in PMMA. The spectral switching and spectral diffusion behaviors are similar to what has been observed in III-V quantum dots [5, 6]. They may be explained within the model of Shimizu and Bawendi [7, 8].

Fluorescence quenching and Photo-enhanced luminescence are studied. In higher pump intensity, lower energy lines are found and identified as phonon replicas of the exciton transition involving local SO-phonon and LO-phonon modes of the NC. Huang-Rhys factor is found to be  $S \approx 0.2$ .

The text of chapter V, in part, is a reprint of the material as it appears in Yaoming Shen, Lin Pang, Y. Fainman, Martin Griswold, Sen Yang, L. V. Butov, and L. J. Sham “Photoluminescence spectral switching of single CdSe/ZnS colloidal nanocrystals in poly(methyl methacrylate)” *Phys. Rev. B* 76, 085312 (2007), where the dissertation author was the first author. The co-authors in this publication directed, supervised, and co-worked on the research which forms the basis of this chapter.

## VI

# Optical characterization of InAs/GaAs Quantum Dots Molecules (Double Quantum Dots)

### VI.A Compare between as-grown quantum dots and self-assembled InAs/GaAs lateral dou- ble quantum dots

Self-assembled semiconductor quantum dots (QDs), from highly strained-layer heteroepitaxy in the Stranski–Krastanow (S–K) growth mode, have been intensively studied because of the  $\delta$ -function-like density of states, which is significant for optoelectronic applications. Spontaneous formation of semiconductor quantum-dot molecules (QDMs), which are clusters of a few QDs, has attracted attention as a possible implementation of future quantum devices such as quantum cellular automata. With the advances in crystal growth techniques, the fabrication methods for nanostructures have been improved continuously. Lateral QDMs

have been achieved by several growth techniques, such as a combination of in situ etching and self-assembly by anisotropic strain engineering on an In(Ga)As/GaAs (311B) superlattice (SL) template .

The formation of InAs Double Quantum Dots (DQDs) is achieved on a GaAs substrate by gas-source MBE (GSMBE) under  $\text{As}_2$  overpressure using the thin-capping-and-regrowth technique. Morphological studies are did by using atomic force microscopy (AFM). Temperature and power dependence of DQD optical properties are investigated.

### VI.A.1 Experimental procedure

All samples are grown on (0-0-1) semi-insulating GaAs substrates by GSMBE in a modified Varian Gen-II system. Element Ga and In are used as the group-III sources, and thermally cracked arsine, which produces  $\text{As}_2$  and  $\text{H}_2$ , is used as the group-V source. The growth rates of GaAs and InAs are 0.6 monolayer (ML) per second and 0.01 ML per second, respectively. After oxide desorption, a 300-nm-thick GaAs buffer layer is grown at a temperature of  $580^\circ\text{C}$ . Under  $\text{As}_2$  overpressure and deposition of 1.8 ML amount of InAs, QDs are formed randomly on the surface at a temperature of  $500^\circ\text{C}$ . Then, the substrate temperature is ramped down to  $470^\circ\text{C}$  and InAs QDs are capped partially with a 6-ML-thick GaAs layer. When 0.6-ML-thick InAs is deposited, DQDs are formed on the partially covered InAs QDs. Then a 150-nm thick GaAs buffer layer is grown and the thin-capping-and-regrowth process is repeated once more. The dot formation is monitored in situ by reflection-high-energy-electron-diffraction (RHEED). After growth the sample is ramped down immediately to room temperature. The embedded DQDs are for PL measurements, and the top DQDs are for AFM measurements. A separate sample is grown with only QDs as a reference (“as-grown QDs”).

Surface morphology is imaged by tapping-mode AFM with a sharpened SiN tip on uncapped samples. PL measurements are carried out in a close-cycle He



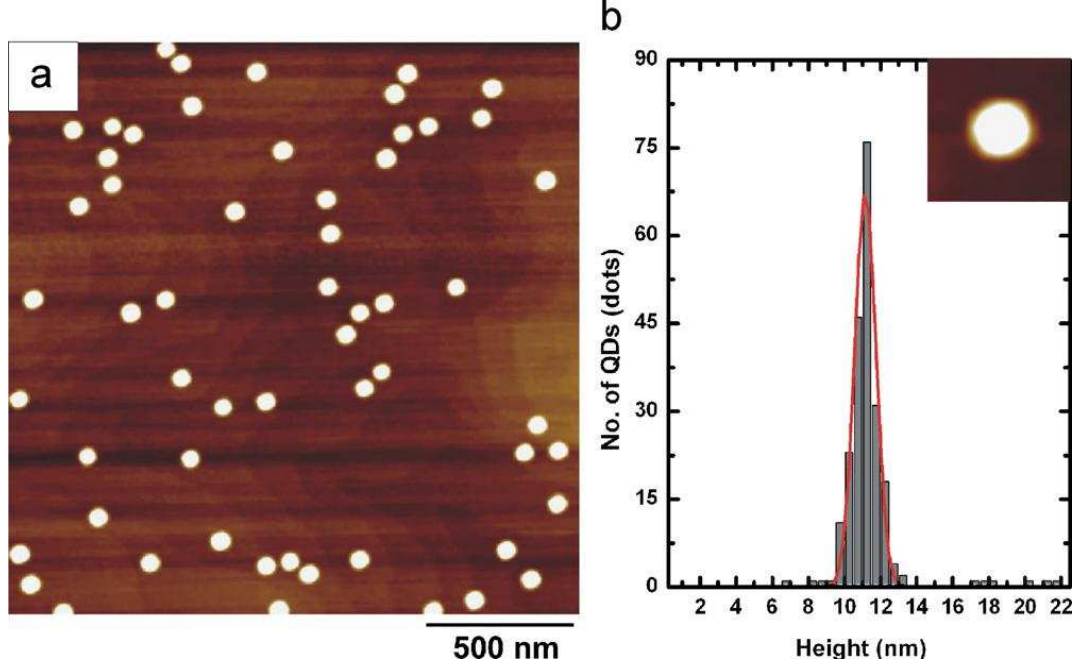


Figure VI.1: (a) shows a  $2 \times 2 \mu\text{m}^2$  AFM image of the as grown QDs sample surface. The distribution of the QDs' heights are shown on (b). We estimate their height to be  $h_1 = 11 \pm 1 \text{ nm}$ .

cryostat at various temperatures and excitation power densities. A diode-pumped solid-state laser at 532 nm emission wavelength is used for excitation and the signal is dispersed in a 0.5 m monochromator and detected by a thermoelectrical cooled InGaAs photodiode using standard lock-in-detection technique.

## VI.A.2 Results and discussion

Fig. VI.1 and Fig. VI.2 show AFM image of as-grown QDs at a coverage of 1.8 ML and DQDs, respectively. DQDs are oriented along the  $[1\bar{1}0]$  crystallographic direction. The dot density of as-grown QDs is  $6 \times 10^9 \text{ cm}^{-2}$ , whereas the total QD density in the DQD sample is  $1.1 \times 10^{10} \text{ cm}^{-2}$ , consisting of  $9.4 \times 10^9 \text{ QDs cm}^{-2}$  from  $4.7 \times 10^9 \text{ DQDs cm}^{-2}$ , and  $1.9 \times 10^9 \text{ QDs cm}^{-2}$  single dots. Each as-grown QD is transformed into a DQD after the thin-capping-and-regrowth procedure, but the DQD density is lower due to merging of some DQDs into single

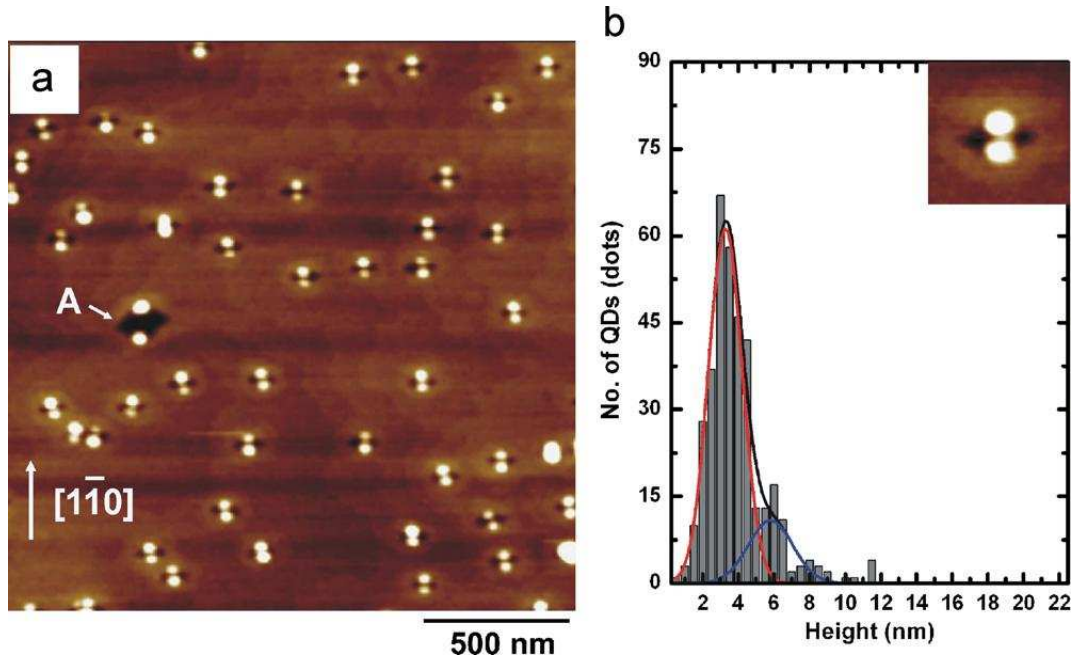


Figure VI.2: (a) shows a  $2 \times 2 \mu\text{m}^2$  AFM image of the Bi-QDs sample surface. The distribution of the Bi-QDs' heights are shown on (b). We estimate their height to be  $3.8 \pm 1\text{nm}$ . A Gaussian fit has been included. It indicates that there are two Gaussian distributions.

dots. Fig. VI.1 (b) and Fig. VI.2 (b) show dot height histograms obtained from AFM images of as-grown QDs and DQDs, respectively. Note that the QDs in the DQD sample are largely comprised of smaller dots than as-grown QDs.

The histogram in Fig. VI.3 shows the center-to-center separation of DQDs, and it is fitted with a Gaussian distribution with an average separation of 22 nm. The QD PL has a Gaussian shape as indicated by the dotted fits in Fig. VI.4 and the FWHM is attributed to the inhomogeneity of the QD ensemble with each single QD contributing only a sharp line ( $< 150\mu\text{eV}$ ) [91].

Despite higher dot density, the PL intensity of DQDs is lower than that of as-grown QDs. It is attributed to defects such as nanovoids, as shown by “A” in Fig. VI.2(a), which could affect the optical efficiency due to nonradiative recombination.

Temperature-dependent PL data from 9 to 290 K are also obtained while the incident excitation intensity is held constantly at  $10\text{ kW/cm}^2$ . Fig. VI.5 shows the temperature dependence of the peak emission energy, which can be fitted by the Varshni model [92]

$$E(T) = E_0 - \frac{\alpha T^2}{T + \beta} \quad (\text{VI.1})$$

where  $E(T)$  and  $E_0$  are the peak energies at  $T$  and 0 K, respectively, and  $\alpha$  and  $\beta$  are constants. The variation of the peak emission energy with temperature can be attributed to the effect of dilation of lattice and electron–lattice interaction. The solid line in Fig. VI.5 is the Varshni equation with  $E_0=1.083\text{ eV}$  for as-grown QDs and  $1.198\text{ eV}$  for DQDs,  $\alpha=3.16\times 10^{-4}\text{ eV/K}$  and  $\beta=93\text{ K}$  for both as-grown QDs and DQDs. The  $\alpha$  and  $\beta$  values agree with those of InAs [92].

The maximum red shift of 23 meV in the DQD curve from the Varshni equation is observed. It is because the dots size is smaller for DQDs than as-grown QDs. So they have bigger quantum confinement energy.

Fig. VI.6 shows the PL intensity of as-grown QDs and DQDs vs. inverse temperature. As the measurement temperature increases from 9 K, the PL

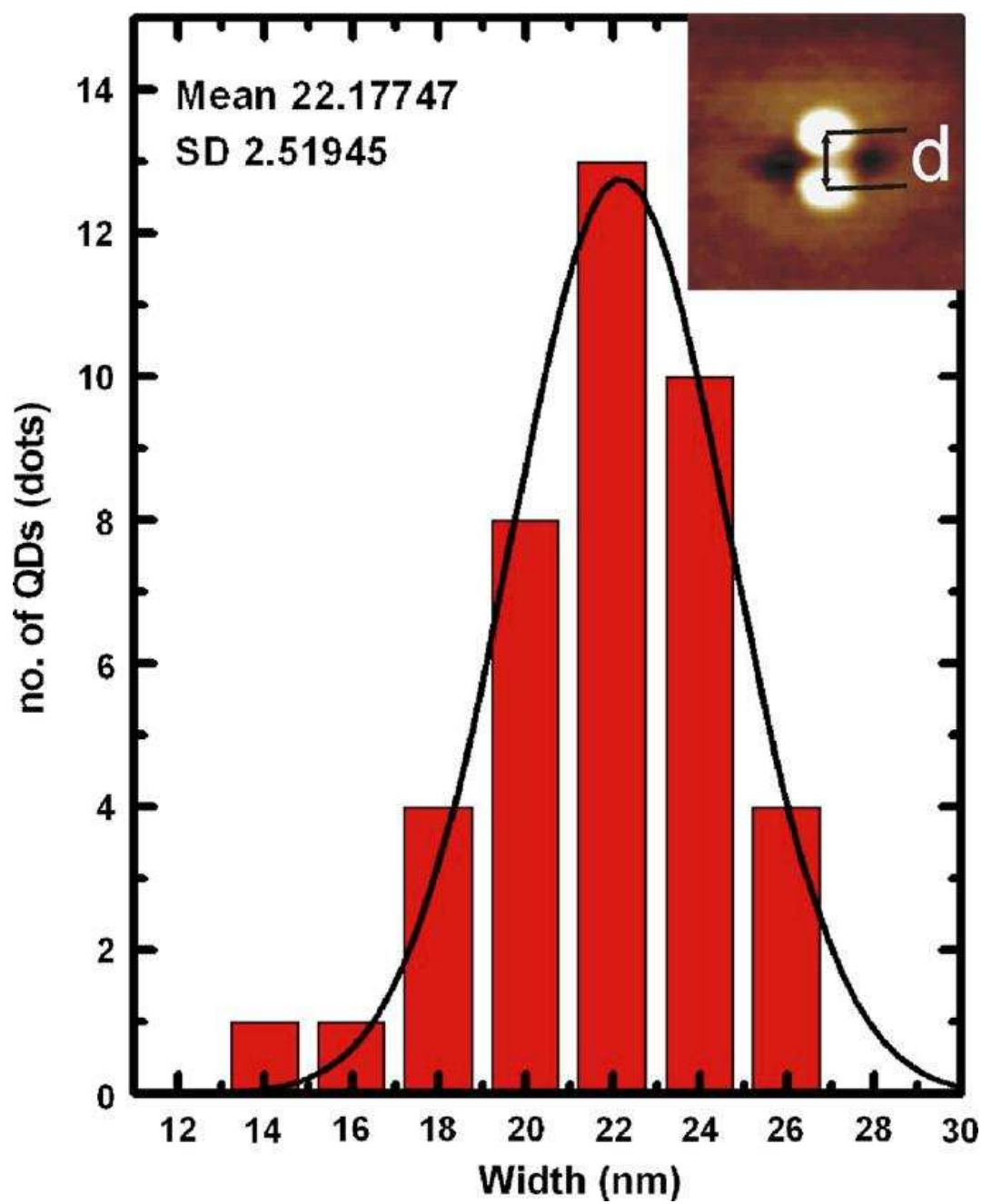


Figure VI.3: Center-to-center width histogram of DQDs with Gaussian fit.

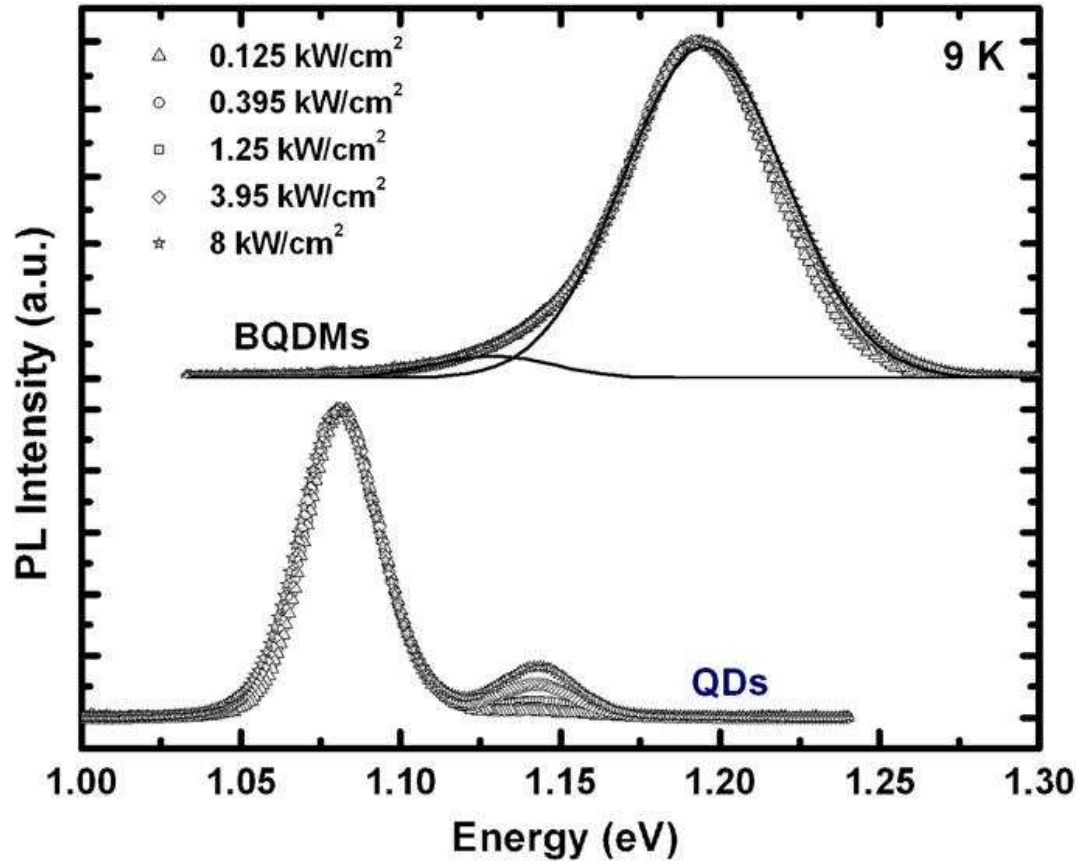


Figure VI.4: PL spectra of as-grown QDs and DQDs at 9 K. The dotted curves for DQDS are the Gaussian components.

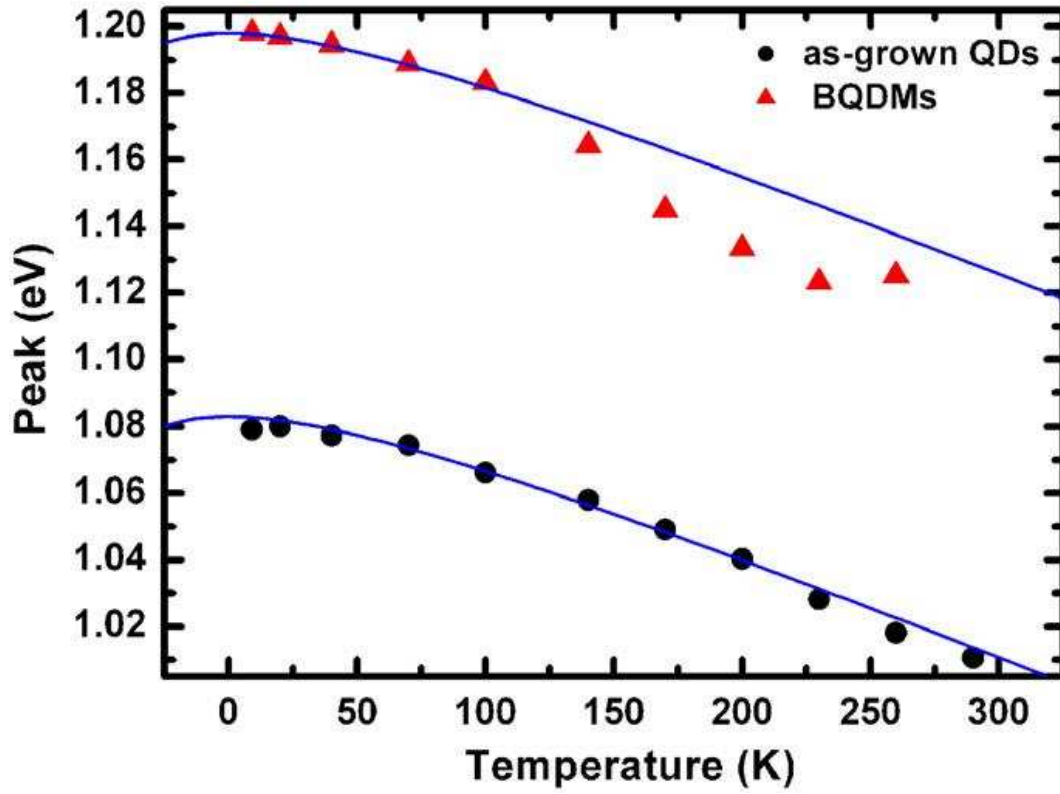


Figure VI.5: The temperature-dependent peak emission energy of as-grown QDs and DQDs. The solid lines are calculations from the Varshni equation.

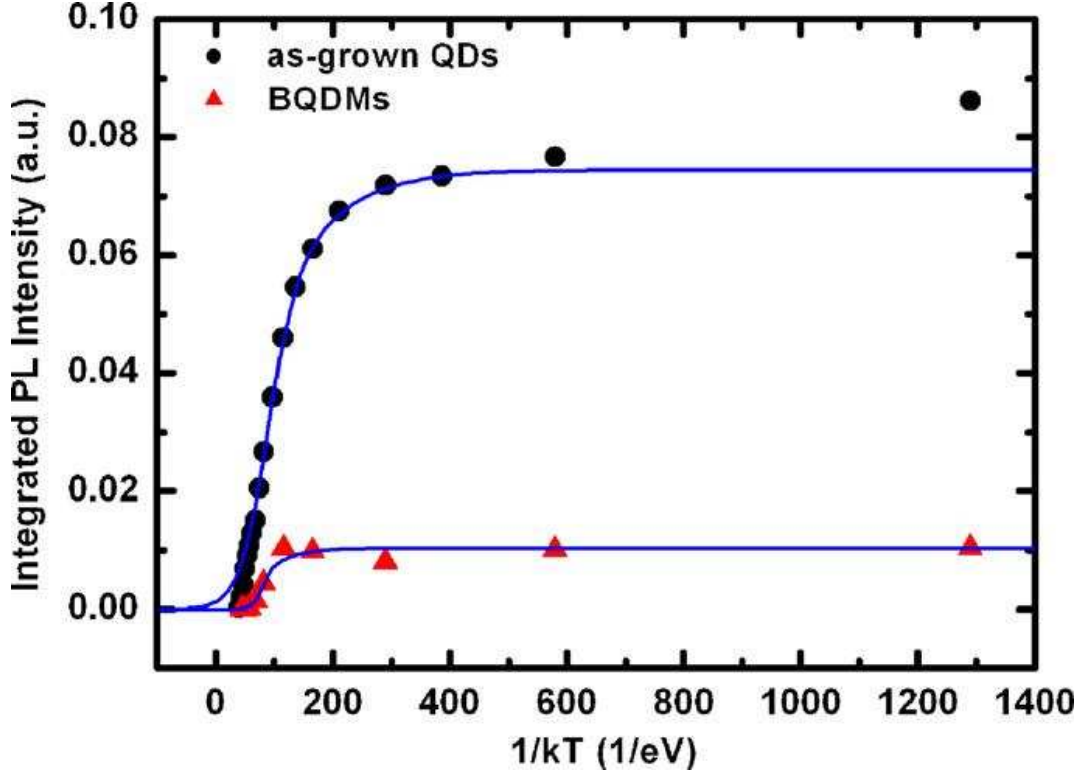


Figure VI.6: The temperature dependence of PL intensity of as-grown QDs and DQDs.

intensity of DQDs remains constant up to 100 K and then rapidly quenches. The solid lines are fitted with an assumption of two thermally activated processes with [93, 94]

$$I(T) = \frac{I(0)}{1 + A \exp(-E_a/kT) + B \exp(-E_b/kT)} \quad (\text{VI.2})$$

where  $I(T)$  and  $I(0)$  are the PL intensity at  $T$  and 0 K, respectively;  $A$  and  $B$  are constants;  $E_a$  and  $E_b$  are thermal activation energies. Activation energy  $E_a$ , derived from the slope of the straight-line portion (150–300 K) of the curves, is 45 and 128 meV for as-grown QDs and DQDs, respectively. The smaller energy  $E_b$  is ascribed to trapped excitons or carriers thermalizing from localized regions resulting from potential fluctuations due to size distribution of QDs. The

larger energy of  $E_a$  corresponds to the difference in energy between the ground state and the wetting layer if there are no localized states.  $E_a$  for DQDs then is expected to be smaller than  $E_a$  for as-grown QDs because of smaller dot size. Our results are contrary to this expectation, indicating the existence of non-radiative recombination centers in DQDs between the QD energy level and the wetting layer energy level.

## **VI.B The Effects of Rapid Thermal Annealing on Doubled Quantum Dots Grown by Molecular Beam Epitaxy**

### **VI.B.1 Introduction**

The effect of different rapid thermal annealing (RTA) temperature on the optical properties of the InAs DQDs grown by molecular beam epitaxy using partial-capping-and-regrowth process has been investigated.

At low temperature annealing, a small blueshift in the PL emission peak of DQDs has been observed; while a stronger blueshift as well as a narrower linewidth with higher PL intensity are achieved at high temperature annealing. By correlating with the diffusion process between the GaAs and InAs, we could explain this phenomena as mixing GaAs into InAs increases the bandgap between conduction band and valence band of the QDs and reduced the potential barrier between the two QDs so that the emission energy goes higher and interaction between the two QDs becomes stronger.

### **VI.B.2 Experimental Procedure**

The DQDs are annealed in nitrogen ambient at temperature of  $650^{\circ}\text{C}$ ,  $700^{\circ}\text{C}$ ,  $750^{\circ}\text{C}$ ,  $800^{\circ}\text{C}$ ,  $850^{\circ}\text{C}$  for 30 s each. For comparable purpose, a separate



sample is grown with only DQDs (“as-grown DQDs”).

Surface morphology is imaged by tapping-mode AFM with a sharpened SiN tip on uncapped samples. The PL are measured in the same way as in section one. The structural property of as-grown DQDs sample is analyzed by cross-sectional transmission electron microscopy (TEM). The TEM measurement is carried out 200 kV on the sample that is milled by focused ion beam (FIB) for electron transparency.

### VI.B.3 Results and Discussions

Fig. IV.7 shows an AFM image of as-grown DQDs fabricated by MBE under  $As_2$  overpressure. It is the image of partially capped InAs QDs with GaAs layer and followed by InAs regrown QDs. Each as-grown QD is transformed into a quantum ring (QR) after partial-capping with 6 ML of GaAs. After that, additional 0.6 ML of InAs is deposited, QRs are turned into DQDs. DQDs are oriented along the  $[1\bar{1}0]$  crystallographic direction with  $1.1 \times 10^{10} cm^{-2}$  dot density.

In order to confirm and understand the DQD structure, cross-sectional TEM is performed, as shown in Fig. VI.8. The lower wetting layer is formed when the first as-grown QDs are made. The 1.7 nm thickness of thin GaAs layer, as shown in this figure is fabricated during partial-capping process. Such layer induces strain field to become higher along the QR structure in  $[1\bar{1}0]$  crystallographic direction. The upper line of wetting formed by regrown InAs during regrowth process, when the amount of deposited InAs is increased, the strain in these two regions relaxes and leads to the formation of DQDs with upper line of wetting layer.

The observed PL in Fig. VI.10 shows a blueshift trend for thermal annealing of as-grown DQDs and their annealed samples. The PL emission peak of DQD sample is shifted to shorter wavelength when increasing annealing temperature. It can be explained by the interdiffusion of In and Ga atoms at the interface between the InAs QD and the GaAs barrier. Mixing the Ga into the InAs increases

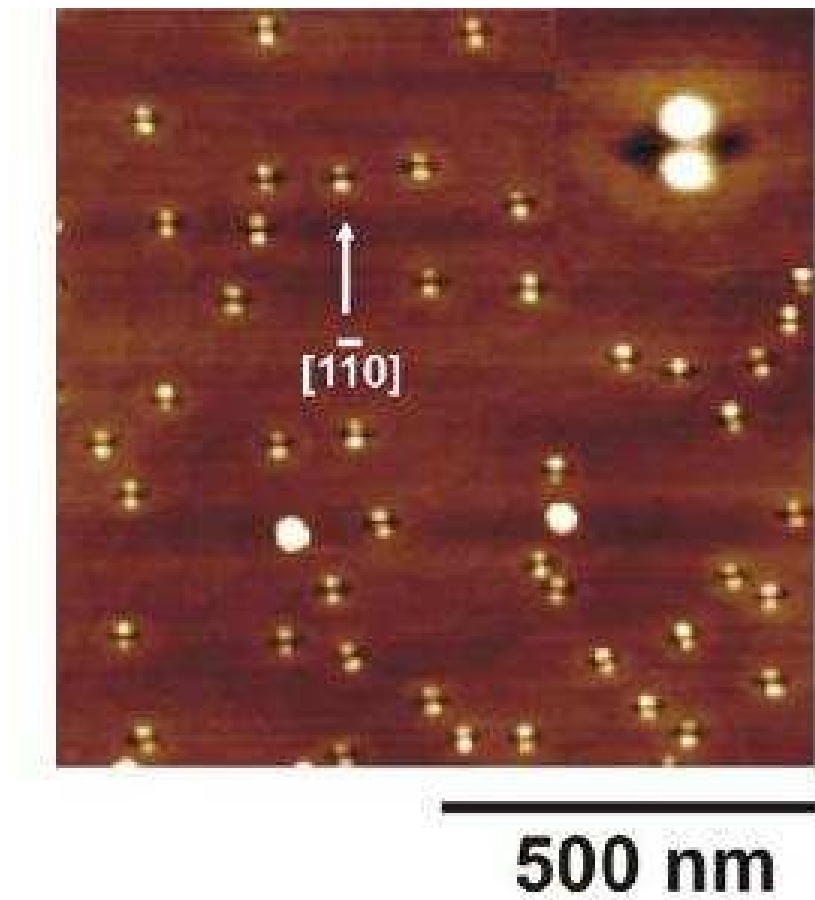


Figure VI.7: AFM image of as-grown DQDs fabricated by MBE under  $As_2$  over-pressure.

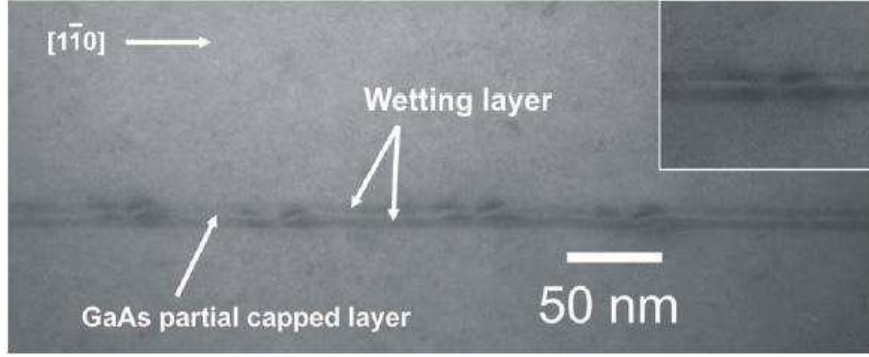


Figure VI.8: Cross-sectional TEM. The lower wetting layer is formed when the first as-grown QDs are made. The 1.7 nm thickness of thin GaAs layer is fabricated during partial-capping process.

the energy bandgap inside the individual QDs while mixing the In into the GaAs will lower the energy bandgap for the outside potential barrier. Both of these will reduce the quantum confinement and makes the interaction between the DQDs become stronger.

Fig. VI.9 shows the low temperature PL spectra of as-grown DQDs which were annealed at  $650^{\circ}\text{C}$ ,  $750^{\circ}\text{C}$  and  $850^{\circ}\text{C}$ . For as-grown DQD sample, the emission peak is 1.198 eV with full-width at half maximum (FWHM) of 61 meV. The peak position of annealed DQDs at  $650^{\circ}\text{C}$ ,  $750^{\circ}\text{C}$  and  $850^{\circ}\text{C}$  are blueshifted from as-grown DQDs by 13, 47 and 102 meV, respectively. For the PL spectrum obtained from the DQD sample annealed at  $850^{\circ}\text{C}$ , the emission linewidth is 33 meV, while the PL spectra of annealed DQDs at  $650^{\circ}\text{C}$  and  $750^{\circ}\text{C}$  exhibit linewidth of 59 and 42 meV, respectively. The linewidth of annealed samples decreases compared to that of the as-grown sample and also annealed samples have pronounced enhancement of the PL peak intensity. Increase in the PL emission intensity is observed probably as a result of curing of point defects, primarily grown at lower temperature. With higher annealing temperatures, narrower FWHM could be explained as: by increasing the bandgap inside of each QD the potential barrier

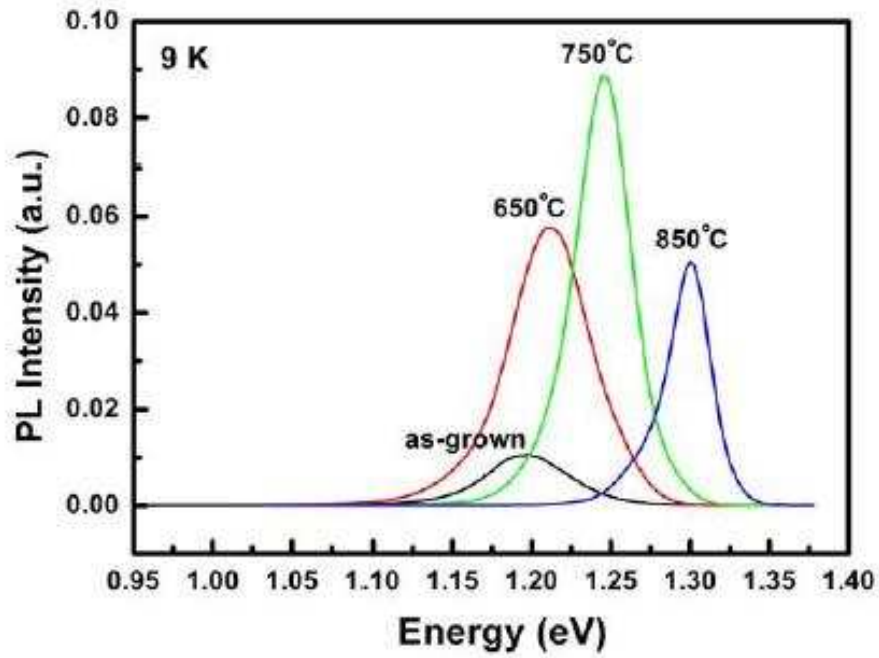


Figure VI.9: Shows the low temperature PL spectra of as-grown DQDs which were annealed at  $650^{\circ}\text{C}$ ,  $750^{\circ}\text{C}$  and  $850^{\circ}\text{C}$ .

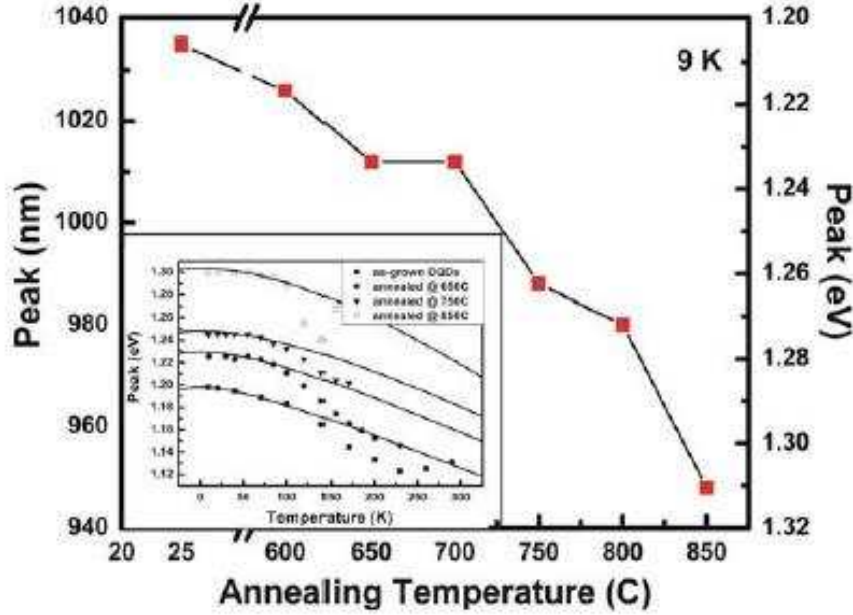


Figure VI.10: Temperature-dependent PL data are measured from 9 K to 290 K with 50 mW incident excitation intensity from a diode-pumped solid-state laser at 532 nm. The PL peak energy as a function of sample temperature is shown in the inset.

between the DQDs gets smaller so that interaction between the DQDs becomes larger. The energy differences caused by the different sizes of the individual QDs will be gradually replaced as new mixed interacting states.

The thermal energy is mainly used to eliminate the dislocations. Therefore, when annealed at relative low temperature ( $600^{\circ}\text{C}$ - $750^{\circ}\text{C}$ ), the emission peak is slightly changed. From TEM image, the partial GaAs capping layer lies in between InAs wetting layer. The interdiffusion between the Ga atoms localized on the base of QDs and the In atoms in wetting layer takes place where the strain is larger. When the sample is annealed at high temperature, the In/Ga interdiffusion becomes stronger. The Ga atoms penetrate into the QDs leading to the quickly reducing the In content in QD. Therefore, a large blueshift of emission peak is

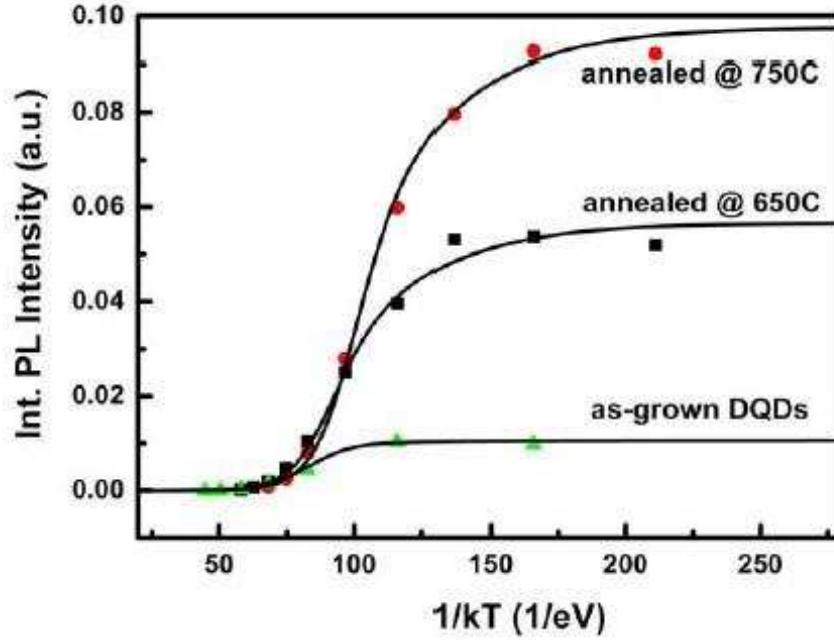


Figure VI.11: Shows the PL intensity of as-grown DQDs and their annealed DQDs as a function of inverse temperature.

observed.

Temperature-dependent PL data are measured from 9 to 290K with 50 mW incident excitation intensity from a diode-pumped solid-state laser at 532 nm. The PL peak energy as a function of sample temperature is shown in the inset of Fig. VI.10 and fitting curves are plotted in solid as guide lines using the Varshni equation. For as-grown DQDs, the solid-line represents the variation of the bulk InAs bandgap with temperature.

In case of an annealed sample at 650°C, the PL data can be fit well by the equation above with  $\alpha = 3.610^{-4} \text{ eV/K}$  and  $\beta = 150 \text{ K}$ . The values lie in the range between those of InAs and GaAs. This further confirms the existence of interdiffusion between Ga and In during the annealing process.

However, the emission peak energy vs temperature data generally follows the Varshni equation only below 100 K. Above 100 K, the emission peak energy

is below of the curve generated by Varshni equation. It can be explained as the following: Varshni equation describes a bandgap change in a single dot. When temperature increases, the electron tunneling between DQDs becomes stronger and dominant. So it will have a larger deviation with the Varshni theory.

Fig. VI.11 shows the PL intensity of as-grown DQDs and their annealed DQDs as a function of inverse temperature. At lower temperature up to 100 K for as-grown DQDs and 85 K for annealed samples, the PL intensity is almost unchanged under a constant flux of electron-hole pairs generated in the sample and the monotonically decreases at high temperatures. It is interesting to note that the quenching temperature in annealed samples occur earlier compared with as-grown DQDs due to smaller confinement potential barrier. At the low temperature, the PL intensity remains almost constant with temperature, which indicates that the carriers captured from the barrier or wetting layer (WL) are stronger than the carriers activation in QDs. However, at the high temperature range, the carrier activation is stronger than the carrier captures leading to the quenching of the luminescence. These curves are fitted with an assumption of two thermally activated processes with equation (2).

In the regime of strong thermal quenching, the curves tend to form a straight line at high temperature. Activation energy  $E_a$  can be derived from the slope of the straight-line portion (150-300K), which is characteristic of an exponential quenching  $\exp(E_a/kT)$ , due to thermal escape from the dots.  $E_a$  are 130 meV for as-grown DQDs and 75 meV for annealed sample at  $650^\circ\text{C}$ . Compared with the results obtained from the as-grown DQD sample,  $E_a$  is found to decrease when the annealing temperature increases, while  $E_b$  remains unchanged.  $E_a$  exhibits the thermal activation energy of carriers through upper states of the dots. The decrease of  $E_a$  with increasing annealing temperature can be interpreted as a change in the depth of the confining potential caused by interdiffusion during annealing, in terms of reduction of carrier localization energy by intermixing of In and Ga atoms at high annealing temperature.

It is noticed that the quality crystal of DQDs are highly improved after annealing in terms of the reduction of the nonradiative recombination centers leading to the enhancement of the optical properties.

## VI.C Summary

The formation of InAs Double Quantum Dots (DQDs) is achieved on a GaAs substrate by gas-source MBE (GSMBE) under  $\text{As}_2$  overpressure using the thin-capping-and-regrowth technique. Temperature and power dependence of DQD optical properties are investigated and compared with As-grown QDs.

The effect of different rapid thermal annealing (RTA) temperature on the optical properties of the InAs DQDs grown by molecular beam epitaxy using partial-capping-and-regrowth process has been investigated. At low temperature annealing, a small blueshift in the PL emission peak of DQDs has been observed; while a stronger blueshift as well as a narrower linewidth with higher PL intensity are achieved at high temperature annealing. By correlating with the diffusion process between the GaAs and InAs, we could explain this phenomena as mixing GaAs into InAs increases the bandgap between conduction band and valence band of the QDs and reduced the potential barrier between the two QDs so that the emission energy goes higher and interaction between the two QDs becomes stronger.

The text of chapter VI, in part, is a reprint of the material as it appears in S. Suraprapapich, Y. Shen, V. A. Odnoblyudov, S. Panyakeow, C. W. Tu, "Self-Assembled Lateral Bi-Quantum Dot Molecule Formation by Gas Source Molecular Beam Epitaxy", 9 January 2007, Journal of Crystal Growth, where the dissertation author was the second author. The co-authors in this publication directed, supervised, and co-worked on the research which forms the basis of this chapter.



# Bibliography

- [1] A. D. Yoffe. Low-dimensional systems: quantum size effects and electronic properties of semiconductor microcrystallites (zero-dimensional systems) and some quasi-two-dimensional systems. *Advances in physics*, 51(2):799–890, 2002.
- [2] D J Mowbray and M S Skolnick. New physics and devices based on self-assembled semiconductor quantum dots. *Journal of Physics D: Applied Physics*, 38(13):2059–2076, 2005.
- [3] A.P. Alivisatos. Perspectives on the physical chemistry of semiconductor nanocrystals. *Journal of Physical Chemistry*, 100(31):13226–13239, 1996.
- [4] Y. Okada K. Akahane T. Miyazawa M. Kawabe N. Yokoyama T. Ohshima, H. Z. Song. Precisely ordered quantum dot array formed using afm lithography for all-optical electron spin quantum computers. *physica status solidi (c)*, 0(4):1364–1367, 2003.
- [5] D. Bertram, M.and C. Hanna, and A.and J. Nozik. *Appl. Phys. Lett.*, 74:2666, 1999.
- [6] N. Panev, M.and E. Pistol, J. Persson, W. Seifert, and L. Samuelson. *Phys. Rev. B*, 70:073309, 2004.
- [7] K. Shimizu, T., M. Bawendi, and G. *Semiconductor and Metal Nanocrystals: Synthesis and Electronic and Optical Properties*. Number 224. Marcel Dekker, New York, 2004.
- [8] M. Nirmal, B. O. Dabbousi, M. G. Bawendi, J. J. Macklin, J. K. Trautman, T. D. Harris, and L. E. Brus. Fluorescence intermittency in single cadmium selenide nanocrystals. *nature*, 383:802–804, October 1996.
- [9] J Singh. *Physics of Semiconductors and their Heterostructures*. McGraw-Hill, New York, 1993.
- [10] Al. L. Efros and M. Rosen. The electronic structure of semiconductor nanocrystals. *Annual Review of Materials Science*, 30(1):475–521, 2000.

- [11] Yosuke Kayanuma and Hiroshi Momiji. Incomplete confinement of electrons and holes in microcrystals. *Phys. Rev. B*, 41(14):10261–10263, May 1990.
- [12] P. E. Lippens and M. Lannoo. Comparison between calculated and experimental values of the lowest excited electronic state of small cdse crystallites. *Phys. Rev. B*, 41(9):6079–6081, Mar 1990.
- [13] M. Shim and P. Guyot-Sionnest. Permanent dipole moment and charges in colloidal semiconductor quantum dots. *jcp*, 111:6955–6964, October 1999.
- [14] Markus Braun, Clemens Burda, Mona Mohamed, and Mostafa El-Sayed. Femtosecond time-resolved electron-hole dynamics and radiative transitions in the double-layer quantum well of the  $\text{cds}/(\text{hgs})_2/\text{cds}$  quantum-dot~quantum-well nanoparticle. *Phys. Rev. B*, 64(3):035317, Jun 2001.
- [15] Thomas Elsaesser, Jagdeep Shah, Lucio Rota, and Paolo Lugli. Initial thermalization of photoexcited carriers in gaas studied by femtosecond luminescence spectroscopy. *Phys. Rev. Lett.*, 66(13):1757–1760, Apr 1991.
- [16] U. Bockelmann and T. Egeler. Electron relaxation in quantum dots by means of auger processes. *Phys. Rev. B*, 46(23):15574–15577, Dec 1992.
- [17] Shintaro Nomura and Takayoshi Kobayashi. Exciton~lo-phonon couplings in spherical semiconductor microcrystallites. *Phys. Rev. B*, 45(3):1305–1316, Jan 1992.
- [18] U. Woggon, F. Gindele, W. Langbein, and J. M. Hvam. Quantum kinetic exciton~lo-phonon interaction in cdse. *Phys. Rev. B*, 61(3):1935–1940, Jan 2000.
- [19] A. P. Alivisatos, T. D. Harris, P. J. Carroll, M. L. Steigerwald, and L. E. Brus. Electron–vibration coupling in semiconductor clusters studied by resonance raman spectroscopy. *The Journal of Chemical Physics*, 90(7):3463–3468, 1989.
- [20] H. Htoon, J. A. Hollingsworth, R. Dickerson, and V. I. Klimov. Effect of zero-to one-dimensional transformation on multiparticle auger recombination in semiconductor quantum rods. *Phys. Rev. Lett.*, 91(22):227401, Nov 2003.
- [21] U. Bockelmann, W. Heller, A. Filoramo, and Ph. Roussignol. Microphotoluminescence studies of single quantum dots. i. time-resolved experiments. *Phys. Rev. B*, 55(7):4456–4468, Feb 1997.
- [22] Sokrates T. Pantelides. The electronic structure of impurities and other point defects in semiconductors. *Rev. Mod. Phys.*, 50(4):797–858, Oct 1978.
- [23] F. Hache, M. C. Klein, D. Ricard, and C. Flytzanis. Photoluminescence study of schott commercial and experimental cssse-doped glasses: observation of surface states. *J. Opt. Soc. Am. B*, 8(9):1802, 1991.

- [24] C. B. Roxlo, B. Abeles, and T. Tiedje. Evidence for lattice-mismatch-induced defects in amorphous semiconductor heterojunctions. *Phys. Rev. Lett.*, 52(22):1994–1997, May 1984.
- [25] Yongchi Tian, Changjun Wu, and Janos H. Fendler. Fluorescence activation and surface-state reactions of size-quantized cadmium sulfide particles in langmuir-blodgett films. *Journal of Physical Chemistry*, 98(18):4913–4918, 1994.
- [26] J. F. Zhang, H. K. Sii, R. Degraeve, and G. Groeseneken. Mechanism for the generation of interface state precursors. *Journal of Applied Physics*, 87(6):2967–2977, 2000.
- [27] R. L. MacDonald and N. M. Lawandy. Observation of charge screening in semiconductor nanocrystals. *Phys. Rev. B*, 47(4):1961–1966, Jan 1993.
- [28] O. Cherniavskaya, L. Chen, and L. Brus. Imaging the photoionization of individual cdse/cds core-shell nanocrystals on n- and p-type silicon substrates with thin oxides. *Journal of Physical Chemistry B*, 108(16):4946–4961, 2004.
- [29] V. I. Klimov, A. A. Mikhailovsky, D. W. McBranch, C. A. Leatherdale, and M. G. Bawendi. Mechanisms for intraband energy relaxation in semiconductor quantum dots: The role of electron-hole interactions. *Phys. Rev. B*, 61(20):R13349–R13352, May 2000.
- [30] R. G. Neuhauser, K. T. Shimizu, W. K. Woo, S. A. Empedocles, and M. G. Bawendi. Correlation between fluorescence intermittency and spectral diffusion in single semiconductor quantum dots. *Phys. Rev. Lett.*, 85(15):3301–3304, Oct 2000.
- [31] W. E. Moerner and L. Kador. Optical detection and spectroscopy of single molecules in a solid. *Phys. Rev. Lett.*, 62(21):2535–2538, May 1989.
- [32] M. Orrit and J. Bernard. Single pentacene molecules detected by fluorescence excitation in a p-terphenyl crystal. *Phys. Rev. Lett.*, 65(21):2716–2719, Nov 1990.
- [33] W. E. Moerner, Taras Plakhotnik, Thomas Irngartinger, Urs P. Wild, Dieter W. Pohl, and Bert Hecht. Near-field optical spectroscopy of individual molecules in solids. *Phys. Rev. Lett.*, 73(20):2764–2767, Nov 1994.
- [34] Eric Betzig and Robert J. Chichester. Single Molecules Observed by Near-Field Scanning Optical Microscopy. *Science*, 262(5138):1422–1425, 1993.
- [35] S Nie, DT Chiu, and RN Zare. Probing individual molecules with confocal fluorescence microscopy. *Science*, 266(5187):1018–1021, 1994.

- [36] J. J. Macklin, J. K. Trautman, T. D. Harris, and L. E. Brus. Imaging and Time-Resolved Spectroscopy of Single Molecules at an Interface. *Science*, 272(5259):255–258, 1996.
- [37] X.S. Xie. Single-molecule spectroscopy and dynamics at room temperature. *Accounts of Chemical Research*, 29(12):598–606, 1996.
- [38] Eli Barkai, YounJoon Jung, and Robert Silbey. Theory of single-molecule spectroscopy: Beyond the ensemble average. *Annual Review of Physical Chemistry*, 55(1):457–507, 2004.
- [39] H. Peter Lu, Luying Xun, and X. Sunney Xie. Single-Molecule Enzymatic Dynamics. *Science*, 282(5395):1877–1882, 1998.
- [40] L. Fleury, J.-M. Segura, G. Zumofen, B. Hecht, and U. P. Wild. Nonclassical photon statistics in single-molecule fluorescence at room temperature. *Phys. Rev. Lett.*, 84(6):1148–1151, Feb 2000.
- [41] M. A. Reed, R. T. Bate, K. Bradshaw, W. M. Duncan, W. R. Frensley, J. W. Lee, and H. D. Shih. Spatial quantization in gaas–algaas multiple quantum dots. *Journal of Vacuum Science and Technology B: Microelectronics and Nanometer Structures*, 4(1):358–360, 1986.
- [42] D. J. Eaglesham and M. Cerullo. Dislocation-free stranski-krastanow growth of ge on si(100). *Phys. Rev. Lett.*, 64(16):1943–1946, Apr 1990.
- [43] Y. Wang, A. Suna, W. Mahler, and R. Kasowski. Pbs in polymers. from molecules to bulk solids. *The Journal of Chemical Physics*, 87(12):7315–7322, 1987.
- [44] C. B. Murray, D. J. Norris, and M. G. Bawendi. Synthesis and characterization of nearly monodisperse cde (e = sulfur, selenium, tellurium) semiconductor nanocrystallites. *Journal of the American Chemical Society*, 115(19):8706–8715, 1993.
- [45] M.A. Hines and P. Guyot-Sionnest. Synthesis and characterization of strongly luminescing zns-capped cdse nanocrystals. *Journal of Physical Chemistry*, 100(2):468–471, 1996.
- [46] V. Colvin, M. Schlamp, and A. Alivisatos. *Nature (London)*, 370:354, 1994.
- [47] M. C. Schlamp, Xiaogang Peng, and A. P. Alivisatos. Improved efficiencies in light emitting diodes made with cdse(cds) core/shell type nanocrystals and a semiconducting polymer. *Journal of Applied Physics*, 82(11):5837–5842, 1997.
- [48] M.-Y. Gao, Y. Yang, B. Yang, F. L. Bian, and J. C. Shen. Synthesis of pbs nanoparticles in polymer matrices. *Chem. Comm*, pages 2779–2780, 1994.

- [49] D.E. Fogg, L.H. Radzilowski, R. Blanski, R.R Schrock, and E.L. Thomas. Fabrication of quantum dotpolymer composites: phosphine-functionalized block copolymers as passivating hosts for cadmium selenide nanoclusters. *Macromolecules*, 30:17426, 1997.
- [50] J. Lee, V.C. Sundar, J.R. Heine, M.G. Bawendi, and K.F. Jensen. Full color emission from ii-vi semiconductor quantum dot-polymer composites. *Adv. Mater*, 12:1102–1105, 2000.
- [51] H. Zhang, Z. Cui, Y. Wang, K. Zhang, X. Ji, C. Lu, B. Yang, and M. Gao. From water-woluble cdte nanocrystals to fluorescent nanocrystal-polymer transparent composites using polymerizable surfactants. *Adv. Mater*, 15:777–780, 2003.
- [52] L. Pang, L.-R Guo, and B. Chen. Polymerized pmma replication of microoptical elements. *Micro-optical Technologies for Measurement, Sensors and Microsystems II and Optical Fiber Sensor Technologies and Applications, SPIE*, 3099:115–122, 1997.
- [53] L. Pang, W. Nakagawa, and Y. Fainman. Fabrication of 2-d photonic crystals with controlled defects using multiple exposures and direct-write. *App. Opt*, 42:5450–5456, 2003.
- [54] Y. Wang, Z. Tang, M.A. Correa-Duarte, I. Pastoriza-Santos, M. Giersig, N.A. Kotov, and L.M. Liz-Marzan. Mechanism of strong luminescence photoactivation of citrate-stabilized water-soluble nanoparticles with cdse cores. *Journal of Physical Chemistry B*, 108(40):15461–15469, 2004.
- [55] W.G.J.H.M. van Sark, P.L.T.M. Frederix, D.J. Van den Heuvel, H.C. Geritsen, A.A. Bol, J.N.J. van Lingen, C. de MelloDonega, and A. Meijerink. Photooxidation and photobleaching of single cdse/zns quantum dots probed by room-temperature time-resolved spectroscopy. *Journal of Physical Chemistry B*, 105(35):8281–8284, 2001.
- [56] M. Jones, J. Nedeljkovic, R.J. Ellingson, A.J. Nozik, and G. Rumbles. Photoenhancement of luminescence in colloidal cdse quantum dot solutions. *Journal of Physical Chemistry B*, 107(41):11346–11352, 2003.
- [57] Y. Wang, Z. Tang, M.A. Correa-Duarte, L.M. Liz-Marzan, and N.A. Kotov. Multicolor luminescence patterning by photoactivation of semiconductor nanoparticle films. *Journal of the American Chemical Society*, 125(10):2830–2831, 2003.
- [58] Lin Pang, Wataru Nakagawa, and Yeshaiahu Fainman. Fabrication of optical structures using su-8 photoresist and chemically assisted ion beam etching. *Optical Engineering*, 42(10):2912–2917, 2003.

- [59] Lin Pang, Wataru Nakagawa, and Yeshaiahu Fainman. Fabrication of two-dimensional photonic crystals with controlled defects by use of multiple exposures and direct write. *Appl. Opt.*, 42(27):5450–5456, 2003.
- [60] George T. Paloczi, Yanyi Huang, Amnon Yariv, and Shayan Mookherjea. Polymeric mach-zehnder interferometer using serially coupled microring resonators. *Optics Express*, 11(21):2666–2671, 2003.
- [61] S. V. Kershaw, M. Harrison, and M. G. Burt. Putting nanocrystals to work: from solutions to devices. *Phil. Trans. R. Soc. Lond. A*, 361:331–343, 2003.
- [62] M. Campbell, D. N. Sharp, M. T. Harrison, R. G. Denning, and A. J. Turberfield. Fabrication of photonic crystals for the visible spectrum by holographic lithography. *Nature*, 404:53–56, 2000.
- [63] George Paloczi, Yanyi Huang, Amnon Yariv, and Shayan Mookherjea. Polymeric mach-zehnder interferometer using serially coupled microring resonators. *Opt. Express*, 11(21):2666–2671, 2003.
- [64] Ph. Tamarat, B. Lounis, J. Bernard, M. Orrit, S. Kummer, R. Kettner, S. Mais, and Th. Basché. Pump-probe experiments with a single molecule: ac-stark effect and nonlinear optical response. *Phys. Rev. Lett.*, 75(8):1514–1517, Aug 1995.
- [65] E.J.G. Peterman, S. Brasselet, and W.E. Moerner. The fluorescence dynamics of single molecules of green fluorescent protein. *Journal of Physical Chemistry A*, 103(49):10553–10560, 1999.
- [66] David A. Vanden Bout, Wai-Tak Yip, Dehong Hu, Dian-Kui Fu, Timothy M. Swager, and Paul F. Barbara. Discrete Intensity Jumps and Intramolecular Electronic Energy Transfer in the Spectroscopy of Single Conjugated Polymer Molecules. *Science*, 277(5329):1074–1077, 1997.
- [67] K. T. Shimizu, R. G. Neuhauser, C. A. Leatherdale, S. A. Empedocles, W. K. Woo, and M. G. Bawendi. Blinking statistics in single semiconductor nanocrystal quantum dots. *Phys. Rev. B*, 63(20):205316, May 2001.
- [68] Mats-Erik Pistol. Spectroscopic studies of random telegraph noise in self-assembled inorganic quantum dots in gain. *Phys. Rev. B*, 63(11):113306, Mar 2001.
- [69] Ilya Sychugov, Robert Juhasz, Jan Linnros, and Jan Valenta. Luminescence blinking of a silicon quantum dot in a  $\text{SiO}_2$  shell. *Physical Review B (Condensed Matter and Materials Physics)*, 71(11):115331, 2005.
- [70] Mitsuru Sugisaki, Hong-Wen Ren, Kenichi Nishi, and Yasuaki Masumoto. Fluorescence intermittency in self-assembled inorganic quantum dots. *Phys. Rev. Lett.*, 86(21):4883–4886, May 2001.

- [71] Warren Nagourney, Jon Sandberg, and Hans Dehmelt. Shelved optical electron amplifier: Observation of quantum jumps. *Phys. Rev. Lett.*, 56(26):2797–2799, Jun 1986.
- [72] Jörg Schuster, Frank Cichos, and Christian von Borczyskowski. Influence of self-trapped states on the fluorescence intermittency of single molecules. *Applied Physics Letters*, 87(5):051915, 2005.
- [73] K. T. Shimizu, W. K. Woo, B. R. Fisher, H. J. Eisler, and M. G. Bawendi. Surface-enhanced emission from single semiconductor nanocrystals. *Phys. Rev. Lett.*, 89(11):117401, Aug 2002.
- [74] S. A. Empedocles and M. G. Bawendi. Quantum-Confined Stark Effect in Single CdSe Nanocrystallite Quantum Dots. *Science*, 278(5346):2114–2117, 1997.
- [75] D. J. Norris and M. G. Bawendi. Measurement and assignment of the size-dependent optical spectrum in cdse quantum dots. *Phys. Rev. B*, 53(24):16338–16346, Jun 1996.
- [76] S.A. Empedocles and M.G. Bawendi. Influence of spectral diffusion on the line shapes of single cdse nanocrystallite quantum dots. *Journal of Physical Chemistry B*, 103(11):1826–1830, 1999.
- [77] Alberto Franceschetti and Alex Zunger. Optical transitions in charged cdse quantum dots. *Phys. Rev. B*, 62(24):R16287–R16290, Dec 2000.
- [78] B.O. Dabbousi, J. Rodriguez-Viejo, F.V. Mikulec, J.R. Heine, H. Mattoussi, R. Ober, K.F. Jensen, and M.G. Bawendi. (cdse)zns core-shell quantum dots: Synthesis and characterization of a size series of highly luminescent nanocrystallites. *Journal of Physical Chemistry B*, 101(46):9463–9475, 1997.
- [79] J. Bardeen. Tunnelling from a many-particle point of view. *Phys. Rev. Lett.*, 6(2):57–59, Jan 1961.
- [80] Jr. Bruchez, Marcel, Mario Moronne, Peter Gin, Shimon Weiss, and A. Paul Alivisatos. Semiconductor Nanocrystals as Fluorescent Biological Labels. *Science*, 281(5385):2013–2016, 1998.
- [81] W. Chan, Warren C. and Shuming Nie. Quantum Dot Bioconjugates for Ultrasensitive Nonisotopic Detection. *Science*, 281(5385):2016–2018, 1998.
- [82] S.R. Cordero, P.J. Carson, R.A. Estabrook, G.F. Strouse, and S.K. Buratto. Photo-activated luminescence of cdse quantum dot monolayers. *Journal of Physical Chemistry B*, 104(51):12137–12142, 2000.

- [83] J. E. Bowen Katari, V. L. Colvin, and A. P. Alivisatos. X-ray photoelectron spectroscopy of cdse nanocrystals with applications to studies of the nanocrystal surface. *Journal of Physical Chemistry*, 98(15):4109–4117, 1994.
- [84] N. Chestnoy, T. D. Harris, R. Hull, and L. E. Brus. Luminescence and photophysics of cadmium sulfide semiconductor clusters: the nature of the emitting electronic state. *Journal of Physical Chemistry*, 90(15):3393–3399, 1986.
- [85] C. R. Kagan, C. B. Murray, M. Nirmal, and M. G. Bawendi. Electronic energy transfer in cdse quantum dot solids. *Phys. Rev. Lett.*, 76(9):1517–1520, Feb 1996.
- [86] Yasuaki Masumoto, Kanae Kawabata, and Tadashi Kawazoe. Quantum size effect and persistent hole burning of cui nanocrystals. *Phys. Rev. B*, 52(11):7834–7837, Sep 1995.
- [87] C. A. Leatherdale, C. R. Kagan, N. Y. Morgan, S. A. Empedocles, M. A. Kastner, and M. G. Bawendi. Photoconductivity in cdse quantum dot solids. *Phys. Rev. B*, 62(4):2669–2680, Jul 2000.
- [88] A. V. Fedorov, A. V. Baranov, and K. Inoue. Exciton-phonon coupling in semiconductor quantum dots: Resonant raman scattering. *Phys. Rev. B*, 56(12):7491–7502, Sep 1997.
- [89] K. Hellwege and H., editors. *Numerical Data and Functional Relationship in Science and Technology*, volume 17. Landolt-Börnstein, New Series, Group III, Springer-Verlag, Berlin, 1982.
- [90] C. Trallero-Giner, A. Debernardi, M. Cardona, E. Menéndez-Proupín, and A. I. Ekimov. Optical vibrons in cdse dots and dispersion relation of the bulk material. *Phys. Rev. B*, 57(8):4664–4669, Feb 1998.
- [91] M. Grundmann, J. Christen, N. N. Ledentsov, J. Böhrer, D. Bimberg, S. S. Ruvimov, ‡, P. Werner, U. Richter, U. Gösele, J. Heydenreich, V. M. Ustinov, A. Yu. Egorov, A. E. Zhukov, P. S. Kop’ev, and Zh. I. Alferov. Ultranarrow luminescence lines from single quantum dots. *Phys. Rev. Lett.*, 74(20):4043–4046, May 1995.
- [92] Y.P. Varshni. *Physica*, 34:149, 1967.
- [93] J. D. Lambkin, L. Considine, S. Walsh, G. M. O’Connor, C. J. McDonagh, and T. J. Glynn. Temperature dependence of the photoluminescence intensity of ordered and disordered in<sub>0.48</sub>ga<sub>0.52</sub>p. *Applied Physics Letters*, 65(1):73–75, 1994.
- [94] A. Nishikawa, Y. G. Hong, and C. W. Tu. Temperature dependence of optical properties of ga<sub>0.3</sub>in<sub>0.7</sub>n<sub>x</sub>as<sub>1-x</sub> quantum dots grown on



gaas (001). *Journal of Vacuum Science and Technology B*, 22(3):1515–1517, 2004.